FACULDADE DE ENGENHARIA DA UNIVERSIDADE DO PORTO

Project of a Photonic Integrated Circuit for PAM digital modulation

Thiago Henrique Gonçalves



Mestrado em Engenharia Eletrotécnica e de Computadores

Supervisor: Prof. Henrique Manuel de Castro Faria Salgado

September 25, 2026

© Thiago Henrique Gonçalves, 2026

Resumo

A fotónica de silício possibilita a criação de sistemas de comunicação compactos e energeticamente eficientes através da integração óptica de elementos fotónicos junto de elementos eletrónicos na plataforma de silício. Em especial, Moduladores de anel ressonante (MRMs) são ideais para estas aplicações por conta de seu tamanho compacto, baixo consumo de energia e alta seletividade de comprimento de onda. Contudo, os MRMs oferecem curvas de ressonância muito sensíveis, dependentes de propriedades como o índice de refração efetivo e características geométricas dos dispositivos sujeitas a erro de fabrico.

Esta dissertação detalha o projeto e a simulação de um modulador de anel ressonante para modulação óptica PAM4 com tecnologia fotónica de silício. É elaborada uma metodologia de simulação multifísica que integra a modelação de portadores elétricos, a definição de guias de onda e acopladores ópticos, além da análise integrada em circuito. A metodologia incorpora os simuladores da Ansys Lumerical sendo eles o CHARGE, MODE, FDTD e INTERCONNECT, além disso a metodologia é automatizada com Python, possibilitando a geração parametrizada dos dispositivos, o controlo das simulações e gestão dos dados.

A metodologia desenvolvida é utilizada para investigar a influência da geometria da junção pn, dos parâmetros dos guias de onda e das condições de acoplamento no desempenho do modulador. São comparadas junções pn verticais convencionais e em formato L em termos de eficiência de modulação, largura de banda e desempenho de transmissão PAM4. Os resultados evidenciam os compromissos entre as características elétricas e ópticas e fornecem orientações para o projeto e otimização de moduladores de anel ressonante.

Abstract

Silicon photonics enables compact and energy-efficient optical communication systems by integrating photonic components on a scalable semiconductor platform. In particular, microring resonator modulators (MRMs) are well suited for these applications due to their small footprint, low power consumption and wavelength selective operation. However, MRMs have very sensitive resonance properties, dependent on the phase modulation induced by carriers, electrical limitations, and device parameters subject to fabrication errors.

This thesis presents the design and simulation of a microring modulator for PAM4 optical modulation based on silicon photonics. A multi-physics simulation workflow is established combining electrical carrier modelling, optical waveguide and coupler characterisation, and circuit level analysis. The workflow integrates the Ansys Lumerical CHARGE, MODE, FDTD and INTERCONNECT solvers through a Python based automation framework enabling parameterized device generation, simulation control and systematic data management.

The developed methodology is used to investigate the influence of p-n junction geometry, waveguide parameters and the coupling conditions on the performance of the modulator. We compare conventional vertical and L-shaped p–n junction designs in terms of modulation efficiency, optical losses, bandwidth and PAM4 transmission performance. The results unveil the trade-offs between electrical and optical characteristics and provide guidelines for the design and optimisation of microring modulators.

UN Sustainable Development Goals

The United Nations Sustainable Development Goals (SDGs) provide a global framework to achieve a better and more sustainable future for all. It includes 17 goals to address the world's most pressing challenges, including poverty, inequality, climate change, environmental degradation, peace, and justice.

The electricity consumption for data centers and telecommunication networks has been rising at an increasing rate because of the massive growth in data traffic which stems from cloud computing and streaming and artificial intelligence operations. The energy consumption of Silicon photonic microring modulators (MRMs) remains lower than that of standard Mach–Zehnder modulators (MZMs) which makes them suitable for developing energy-efficient optical interconnects. The research work focuses on the design workflow of MRM-based devices to support energy-efficient optical communication systems.

The specific Sustainable Development Goals addressed in this work are:

SDG 7 Ensure access to affordable, reliable, sustainable and modern energy for all

SDG 9 Build resilient infrastructure, promote inclusive and sustainable industrialization and foster innovation

SDG	Target	Contribution	Performance Indicators and Metrics
7	7.3	Improving the modulation efficiency (nm/V) and reducing the drive voltage of ring modulators lowers the energy consumption per transmitted bit in optical interconnects.	Energy consumption per bit (pJ/bit); tuning efficiency (nm/V)
	7.a	Characterizing and optimizing electro-optic mechanisms contributes to more efficient photonic device technologies for future communication systems.	Reduction in static/dynamic power consumption (mW) of the modulator
9	9.4	Enabling more compact, energy-efficient photonic components supports the upgrade of communication infrastructure towards greater resource-use efficiency.	Device footprint (μm^2); Q-factor; extinction ratio (dB)
	9.5	Contributing simulation and characterization methodologies for silicon photonic modulators supports ongoing research and innovation in photonic integrated circuits.	Number of validated device models / methodologies developed

Declaration of honour

I declare that this dissertation is my own work and has not previously been submitted or assessed at this or any other institution. References to other authors (statements, ideas, thoughts), as well as the use of published works, strictly comply with the rules of attribution and are duly identified in the text and in the bibliographic references, in accordance with the applicable referencing standards. I am aware that the practice of plagiarism or self-plagiarism constitutes an academic offence, as established in the U.Porto Code of Ethics.

I also declare that I have used Artificial Intelligence tools to complete part(s) of this dissertation, and that this use and its results have been carefully checked for errors, inaccuracies, unfounded attributions or other forms of bias in content and arguments, as well as determining authorship. Specifically, Artificial Intelligence tools were used as a research aid tool, as a grammar and spelling checker and as a programming aid in the development of scripts in Python.

Thiago Henrique Gonçalves



Index

1 Introduction **1**
- 1.1 Context . . . 1
- 1.2 Motivation . . . 1
- 1.3 Objective . . . 2
- 1.4 Thesis Structure . . . 2

2 Theoretical Background **3**
- 2.1 Light-Matter Interaction Mechanisms . . . 3
  - 2.1.1 Electro-Optic Effects . . . 3
  - 2.1.2 Carrier-Induced Effects . . . 4
  - 2.1.3 Thermo-Optic Effect . . . 4
  - 2.1.4 Summary on Optical Modulation . . . 5
- 2.2 Silicon Photonics Passive Components . . . 5
  - 2.2.1 Optical Waveguides . . . 6
  - 2.2.2 Y-Branch Splitters and Combiners . . . 7
  - 2.2.3 Directional couplers . . . 8
- 2.3 PN-Junction Phase Shifters . . . 9
  - 2.3.1 PN-junction Figures of Merit . . . 10
  - 2.3.2 Speed Limitations and RC Effects . . . 11
- 2.4 Mach-Zehnder Modulator . . . 12
- 2.5 Microring Resonator Modulators . . . 13
  - 2.5.1 Ring Geometry and Round-Trip Parameters . . . 14
  - 2.5.2 Cavity Energy and Photon Lifetime . . . 15
  - 2.5.3 Resonance condition and parameters . . . 17
  - 2.5.4 Transmission transfer functions . . . 19
  - 2.5.5 Coupled Mode Theory of Ring Resonators . . . 21
  - 2.5.6 Microring modulator Figures of Merit . . . 25
- 2.6 Summary . . . 27

3 Simulation Methodology **28**
- 3.1 Introduction . . . 28
- 3.2 Python Automation Layer . . . 29
- 3.3 Database Schema . . . 30
- 3.4 PN-Junction Characterisation (CHARGE) . . . 32
- 3.5 Rib Waveguide Characterisation (MODE) . . . 32
  - 3.5.1 Undoped Waveguide Characterisation . . . 33
  - 3.5.2 Doped Waveguide Characterisation . . . 33
- 3.6 Coupler Characterisation (FDTD) . . . 34

3.7 Circuit Assembly and Analysis (INTERCONNECT) . . . 35
3.7.1 Microring Modulator Compound Element . . . 35
3.7.2 Frequency-Domain Analysis . . . 36
3.7.3 Time-Domain Analysis . . . 37
3.8 Summary . . . 39

4 Device Design and Target Specifications **40**
4.1 Introduction and Design Objectives . . . 40
4.2 Fabrication Constraints and Candidate Waveguide Geometries . . . 41
4.2.1 Analytical Design Criteria . . . 41
4.2.2 Resonance-shift and insertion-loss criterion . . . 43
4.2.3 Doping Profile and Junction Geometry . . . 45
4.3 Ring Radius selection procedure . . . 47
4.4 Coupling-gap selection procedure . . . 47
4.5 Summary . . . 48

5 Simulation Results and Device Optimisation **49**
5.1 PN Junction and Waveguide Simulation Results . . . 49
5.1.1 Junction shape . . . 51
5.1.2 Junction Characteristics . . . 53
5.1.3 Loaded Quality Factor and Optical Bandwidth Optimisation Targets . . . 57
5.2 Coupling-Gap optimisation . . . 60
5.3 Microring Modulator Optimised Device and Generated Layout . . . 60
5.3.1 Transmission Spectrum Results . . . 61
5.3.2 Eye Diagrams . . . 64
5.4 Summary . . . 67

6 Conclusion and Future Work **68**
6.1 Overview . . . 68
6.2 Main Findings . . . 68
6.3 Limitations . . . 69
6.4 Future Work . . . 69
6.5 Final Remarks . . . 70

References **71**

List of Figures

2.1 Strip and rib waveguides cross sections based on [1, Ch. 3]. 6
2.2 Electric field intensity (linear scale) of the fundamental guided mode in a rib waveguide, simulated using Ansys Lumerical MODE. 7
2.3 Y-branch splitter/combiner diagram based on [1, Ch. 4]. 8
2.4 Signal-flow graphs of an ideal directional coupler. The graph on the left follows the physical port ordering whilst the graph on the right doesn't as a trade-off for having no crossing arrows 9
2.5 PN junction cross-section with and without the depletion region based on [1, Ch. 6] 10
2.6 Mach-Zehnder interferometer diagram based on [1, Ch. 4]. 12
2.7 Mach–Zehnder Modulator Interferometer transfer function. 13
2.8 Diagram of ring/racetrack resonators based on [1, Ch. 4]. 14
2.9 Normalized spectral intensity obtained from the Fourier transform of an exponentially decaying resonant cavity field. 18
2.10 Signal-flow graph of an all-pass microring resonator modulator. 19
2.11 Signal-flow graph of an add-drop microring resonator modulator. 20
2.12 Power transmission of the all-pass microring resonator through port as a function of the round-trip phase ϕ_{rt} with $A_{rt} = 0.9$ and $t = 0.9$. 20
2.13 Power transmission of the add-drop microring resonator through port as a function of the round-trip phase ϕ_{rt} with $A_{rt} = 0.9$ and $t_1 = t_2 = 0.9$. 21
2.14 Power transmission of the add-drop microring resonator drop port as a function of the round-trip phase ϕ_{rt} with $A_{rt} = 0.9$ and $t_1 = t_2 = 0.9$. 21
2.15 Transfer function amplitude $|T(\Delta\omega)|$ of a microring resonator as a function of detuning for different coupling ratios CR $= \tau_i/\tau_c$. The functions are computed using the CMT formulation with a quality factor of $Q = 10000$. 24
2.16 Transfer function amplitude $|T(\Delta\omega)|$ of a microring resonator as a function of detuning for different quality factors $Q = \omega_0\tau_{ph}$ at critical coupling (CR $= 1$). . . 24
2.17 Transmission of MRM at different voltages adapted from [8]. 25

3.1 Component diagram of the simulation workflow. 29
3.2 Class diagram of the simulation workflow. 29
3.3 CHARGE simulation setup for PN-Junction 32
3.4 MODE simulation setup 33
3.5 FDTD simulation setup for coupler characterisation. 34
3.6 Microring Modulator Compound INTERCONNECT Element 36
3.7 Microring Modulator Block Diagram 37
3.8 Microring modulator frequency domain analysis setup, with DC Source and Optical Network Analyzer (ONA) 38

3.9 Microring modulator time domain analysis setup, with PAM driver, transmitter and receiver chains . . . 39

4.1 Rib waveguide cross-section . . . 41
4.2 Geometrical definition of the clearance angle θ_c in the microring modulator. . . . 42
4.3 Active modulation fraction χ of an all-pass microring modulator as a function of microring bend radius R with $w_{wg} = 0.5\,\mu m$, $w_{slab} = 5.0\,\mu m$, $g = 0.4\,\mu m$ and $C_s = 2.5\,\mu m$. . . . 42
4.4 3-dB insertion loss quality factor as a function of achievable resonance shift $\Delta\lambda_{res}$. The blue region represents Q values that lower the IL below the 3-dB value. . . . 44
4.5 3-dB insertion loss frequency linewidth as a function of achievable resonance shift $\Delta\lambda_{res}$. The blue region represents Δf_{FWHM} values that lower the IL below the 3-dB value. . . . 44
4.6 PN junction abrupt vertical junction cross-section . . . 45
4.7 PN junction L-shaped junction cross-section . . . 45
4.8 Implant Doping for abrupt vertical junction . . . 46
4.9 Implant Doping for L-shaped junction . . . 46
4.10 Cross-sectional schematic of the rib waveguide geometry with the coordinate origin located at the center of the core–slab interface. . . . 46
4.11 Coupling quality factor Q_c as a function of the power coupling coefficient κ^2. . . . 48

5.1 Electron carrier density distribution across p–n junction cross-sections at (top row) 0 V and (bottom row) 10 V reverse bias. Vertical junction with core width 500 nm compared against L-shaped geometry at 500 nm core width. The colorbar indicates electron carrier concentration (cm^{-3}). . . . 52
5.2 Junction capacitance as a function of reverse-bias voltage for the conventional and L-shaped 500 nm PN junctions. Obtained from a small-signal AC simulation at f = 10 GHz. . . . 53
5.3 Electrical cutoff frequency as a function of reverse-bias voltage for the conventional and L-shaped 500 nm PN junctions. Obtained from a small-signal AC simulation at f = 10 GHz. . . . 53
5.4 Resonance wavelength shift as a function of reverse-bias voltage for the conventional and L-shaped 500 nm PN junctions. . . . 54
5.5 Local voltage-length product as a function of wavelength for multiple bend radii for the conventional and L-shaped 500 nm PN junctions. . . . 54
5.6 Stored electrical energy as a function of reverse-bias voltage for the conventional and L-shaped 500 nm PN junctions. . . . 55
5.7 Real component of the effective index as a function of wavelength for the conventional and L-shaped 500 nm PN junctions. . . . 55
5.8 Imaginary component of the effective index as a function of wavelength for the conventional and L-shaped 500 nm PN junctions. . . . 56
5.9 Group index as a function of wavelength for the conventional and L-shaped 500 nm PN junctions. . . . 56
5.10 Intrinsic quality factor Q_i as a function of wavelength for the 450 nm vertical, 500 nm vertical, and L-shaped 500 nm PN junction configurations. . . . 57
5.11 Interpolation of the intrinsic quality factor Q_i as a function of ring radius for the L-shaped and vertical PN junction designs. . . . 59
5.12 Power coupling κ^2 as a function of coupling gap at the design wavelength $\lambda_0 =$ 1550 nm. . . . 60

5.13 Generated GDS layout 61
5.14 Transmission spectrum of microring modulator with L-shaped PN junction. . . . 62
5.15 Transmission spectrum of microring modulator with vertical PN junction. 63
5.16 Accumulated wavelength shift as a function of reverse bias voltage for the two PN junction configurations. 64
5.17 OOK eye diagrams comparing L-shaped and vertical PN junction microring modulators at 5 and 10 Gbaud. 65
5.18 PAM4 eye diagrams comparing L-shaped and vertical PN junction microring modulators at 5 and 10 Gbaud. 66

List of Tables

2.1 Plasma dispersion model parameters for silicon free-carrier effects, written in the unified form of Eq. (2.3) adapted from [1, Ch. 6]. 5

3.1 Database tables used in the simulation workflow. 30
3.2 Schema of the `pn_junctions` table. 30
3.3 Schema of the `microring_modulators` table. 30
3.4 Schema of the `mode_frequency_sweep_simulations` table. 31
3.5 Schema of the `mode_voltage_sweep_simulations` table. 31
3.6 Schema of the `pn_junction_ac_characterisation` table. 31
3.7 Schema of the `fdtd_coupling_simulations` table. 31

4.1 Generic silicon photonic PDK fabrication process parameters used as reference for the PN-junction design, adapted from [1, Ch. 10]. 41
4.2 Summary of the doping profiles used for the investigated PN junctions. The abrupt junctions (500 nm and 450 nm core widths) share the same doping configuration. Diffusion regions are defined by their lateral (x) and vertical (y) extents, while implanted regions are characterised by their lateral extent and implantation depth (d). 46

5.1 Summary of microring modulator performance metrics for L-shaped and vertical PN junctions. 62
5.2 Modulation voltage levels for OOK and PAM4 schemes across PN junction configurations. 64

List of Acronyms

CLI	Command-Line Interface
CMOS	Complementary Metal-Oxide-Semiconductor
CMT	Coupled Mode Theory
CW	Continuous Wave
DM	Direct Modulation
EAM	Electro-Absorption Modulator
EO	Electro-Optic
ER	Extinction Ratio
FDTD	Finite-difference time-domain method
FKE	Franz–Keldysh Effect
FSR	Free Spectral Range
FWHM	Full Width Half Maximum
GHz	Gigahertz
IL	Insertion Loss
$LiNbO_3$	Lithium Niobate
MZI	Mach–Zehnder Interferometer
MZM	Mach–Zehnder Modulator
MRM	Micro-Ring Modulator
OM	Optical Modulator
OMA	Optical Modulation Amplitude
OOK	On-off Keying
PAM	Pulse Amplitude Modulation
PDK	Process Design Kit
PIC	Photonic Integrated Circuit
PN	P-type / N-type (junction)
Q	Quality Factor
Si	Silicon
SiPh	Silicon Photonics
SOI	Silicon-On-Insulator
SSI	Small Scale Integration
VLSI	Very Large Scale Integration

Chapter 1

Introduction

1.1 Context

Silicon Photonic Integrated Circuits (PICs) have achieved a level of technological advancement that makes them a crucial component for extensive opto-electronic integration. By utilizing the established manufacturing capabilities of the semiconductor industry, silicon photonics enables the creation of intricate photonic functions at the chip level — in *silicon platforms* whilst non SiPh PICs utilize other platforms like InP or $LiNbO_3$ requiring specialized and more expensive processes — offering cost-effectiveness, high reproducibility, and low energy consumption [1].

The introduction of Process Design Kits (PDKs) by commercial foundries has played a significant role in speeding up the adoption of silicon PICs. These PDKs provide standardized and thoroughly tested photonic components — such as waveguides, couplers, resonators, and optical modulators — along with design guidelines and fabrication limitations. Consequently, system designers can concentrate on innovation at the circuit and system levels while depending on reliable and scalable manufacturing processes [1].

Silicon photonics is primarily used in optical communications, especially for high-speed data transfer, signal routing, and optical modulation in data center interconnects and high-performance computation. Beyond communications, this technology is becoming increasingly important in new areas like hardware acceleration for linear algebra, sensing, and artificial intelligence, where compactness, energy efficiency, and high bandwidth are essential [1].

1.2 Motivation

Optical modulators are essential components of photonic communication systems, as they facilitate the transformation of electrical data into modulated optical signals. Mach–Zehnder Modulators (MZMs) are currently the preferred choice in high-performance systems due to their linear response and capability to support advanced modulation formats through precise interferometric phase control [1].

However, when MZMs are implemented in monolithic silicon photonics platforms, they often have a relatively large size and limited modulation efficiency, leading to higher power consumption and size footprint. These challenges become more pronounced as photonic systems progress from small-scale integration (SSI) to very-large-scale integration (VLSI) [2].

In this scenario, Micro-Ring Modulators (MRMs) present an appealing alternative. Their resonant characteristics allow for strong light–matter interaction within a compact size, resulting in enhanced energy efficiency and inherent wavelength selectivity. These features make MRMs particularly suitable for dense wavelength-division multiplexing (DWDM) [3] systems and multi-level Pulse Amplitude Modulation (PAM) [4].

The motivation for this work is thus driven by the demand for compact, high-speed, and energy-efficient silicon-based optical modulators that can support higher data rates while remaining compatible with standard CMOS fabrication processes.

1.3 Objective

This dissertation primarily aims to design, simulate, layout, and validate a silicon photonic integrated circuit that can execute multi-level Pulse Amplitude Modulation (PAM-*N*) on an optical carrier.

The proposed approach utilizes Micro-Ring Modulators with PN-junction phase shifters. This thesis presents all phases of the design process, from device-level modeling and circuit simulation to layout creation and system-level validation.

Simulations of photonic devices and circuits were be conducted using Lumerical software tools, and the final design was then assessed within a simulated digital communication system, including the optical receiver, to evaluate its performance.

1.4 Thesis Structure

This thesis is organized in the following chapters:

- Chapter 2 presents the theoretical background on silicon photonics and microring modulators.
- Chapter 3 describes the simulation methodology, modeling framework and pipeline.
- Chapter 4 details the design procedures for the microring modulator.
- Chapter 5 presents and discusses the simulation results and design optimisations.
- Chapter 6 summarizes the main conclusions of this work and outlines directions for future research.

Chapter 2

Theoretical Background

2.1 Light-Matter Interaction Mechanisms

Light-matter interaction underpins the operation of optical modulators, switches, and sensors in integrated photonics. The optical response of a material can arise from changes in polarization, carrier densities, temperature and electric-field-induced band structure modifications. This section is based on the modulation techniques presented by Agrawal [5].

2.1.1 Electro-Optic Effects

Electro-optic modulation arises from the interaction between an applied electric field and the optical polarization or absorption properties of a material.

The induced polarization $\mathbf{P}$ in a material due to an electric field $\mathbf{E}$ is given by the power-series (2.1) from [6, Ch. 1], where $\chi^{(n)}$ denotes the n-th order susceptibility tensor.

$$\mathbf{P} = \varepsilon_0 \left(\chi^{(1)}\mathbf{E} + \chi^{(2)}\mathbf{E}^2 + \chi^{(3)}\mathbf{E}^3 + \dots \right) \tag{2.1}$$

Usually only the first susceptibility term $\chi^{(1)}$ of the material is considered, which gives rise to the refractive index n and the change in the velocity and wavelength of a field inside a material. However higher order susceptibilities give rise to exploitable effects for modulation purposes.

Linear Electro-Optic Effect - Pockels Effect The Pockels effect originates from the second-order susceptibility $\chi^{(2)}$, producing a refractive index change linearly proportional to the applied electric field. It requires non-centrosymmetric materials and enables high-speed, low-loss phase modulation [6, Ch. 11].

Silicon, being centrosymmetric, does not exhibit a strong effect, which makes it incompatible with SiPh, requiring other materials — Lithium niobate ($LiNbO_3$) is the canonical example [1].

Nonlinear Electro-Optic Effects Higher-order electro-optic effects — like the Kerr effect which stems from the third-order susceptibility $\chi^{(3)}$ — are usually weak for practical electric-field modulation purposes, since they require high optical intensity.

Electroabsorption Effect – Franz–Keldysh Effect The Franz–Keldysh effect (FKE) is a *field-induced modification of semiconductor absorption*, where an applied electric field shifts the effective bandgap and alters the optical absorption. It underlies electro-absorption modulators (EAMs) and has been quantified in both direct- and indirect-gap materials [7]. While enabling fast amplitude modulation, its impact in indirect-gap silicon is weak, and modulation is inherently lossy [7].

2.1.2 Carrier-Induced Effects

Plasma Dispersion Effect describes how variations in electron (N) and hole (P) densities change the real and imaginary parts of the refractive index, in which the imaginary part represents absorption α. The absorption spectrum and refractive index are intrinsically linked through the Kramers-Kronig relations (2.2), allowing one to be calculated from the other [7].

$$\Delta n(\omega) = \frac{c}{\pi} \mathscr{P} \int_0^\infty \frac{\Delta\alpha(\omega')}{\omega'^2 - \omega^2} d\omega' \tag{2.2}$$

The model of how Δn and $\Delta\alpha$ change with electron and hole densities is generalized as (2.3) — with parameters shown in the Table 2.1 — from [1].

$$\begin{aligned} \Delta n(\lambda) &= -A(\lambda)N^\alpha - B(\lambda)P^\beta \\ \Delta\alpha(\lambda) &= C(\lambda)N^\gamma + D(\lambda)P^\delta \quad [\mathrm{cm}^{-1}] \end{aligned} \tag{2.3}$$

Both the dispersive and absorptive effects of free carriers in silicon are captured by the models compiled in Table 2.1. The plasma dispersion effect is influenced differently by electrons and holes. For a given carrier density, electrons cause a relatively greater rise in absorption, whereas holes cause a stronger refractive index shift. Therefore, in phase shifters and resonant modulators where reducing extra optical loss is crucial, hole-dominated modulation is typically favored [1].

The free-carrier absorption is too weak for electroabsorption modulation so in SiPh the refractive index modulation through plasma dispersion is the main use case [8].

2.1.3 Thermo-Optic Effect

The thermo optic coefficient, the temperature dependence of the refractive index, in silicon is around $\frac{dn}{dT} = 1.87 \cdot 10^{-4}\,\mathrm{K}^{-1}$ [1, Ch. 6.6], which is relatively large compared to the plasma dispersion effect, but with a slower time response, not being suited for modulation purposes.

The thermo-optic effect therefore is utilized for wavelength tuning and stabilization of MRMs in silicon, since these devices require a stable refractive index due to the extremely narrowband they operate in, and this can be highly sensitive to the environment, temperature and fabrication errors [1].

Wavelength	Parameters			
	A	α	B	β
	C	γ	D	δ
Common phenomenological expressions [1]				
1550 nm	8.8×10^{-22}	1	8.5×10^{-18}	0.8
	8.5×10^{-18}	1	6.0×10^{-18}	1
1310 nm	6.2×10^{-22}	1	6.0×10^{-18}	0.8
	6.0×10^{-18}	1	4.0×10^{-18}	1
More recent experimental studies [1]				
1550 nm	5.4×10^{-22}	1.011	1.53×10^{-18}	0.838
	8.88×10^{-21}	1.167	5.84×10^{-20}	1.109
1310 nm	2.98×10^{-22}	1.016	1.25×10^{-18}	0.835
	3.48×10^{-22}	1.229	1.02×10^{-19}	1.089
Free-carrier Drude model [1]				
λ	$3.64\times10^{-10}\lambda^2$	1	$3.51\times10^{-6}\lambda^2$	0.8
	$3.52\times10^{-6}\lambda^2$	1	$2.40\times10^{-6}\lambda^2$	1

Table 2.1: Plasma dispersion model parameters for silicon free-carrier effects, written in the unified form of Eq. (2.3) adapted from [1, Ch. 6].

2.1.4 Summary on Optical Modulation

Optical modulators have evolved alongside laser and fiber technologies, the following modulator techniques are discussed in [5, Ch .3].

Early devices relied on *direct modulation (DM)* of the laser source — turning it on and off — limited to 10 Gb/s due to high frequency chirp.

Currently high-performance modulators utilize MZM configurations in the non-centrosymmetric crystal $LiNbO_3$, which is not compatible with SiPh processes, requiring chip-on-chip architectures to be feasible, adding complexity.

Silicon Photonics ultimately relies on the *plasma dispersion effect* for phase-shifters in both MZM and MRM, allowing amplitude and phase modulation and the thermo-optic later complements these mechanisms, enabling wavelength tuning, and resonant device optimisation.

Together, these effects define the operational toolkit for modern integrated photonics.

2.2 Silicon Photonics Passive Components

This section is primarily based on the treatment of silicon photonic passive devices presented by Chrostowski and Hochberg [1] which represent the fundamental building blocks of SiPh PICs.

Mach-Zehnder interferometers and ring resonators are also classified as passive photonic components. However, since these structures are employed as active devices in the context of optical modulation, they are discussed in detail in their respective sections dedicated to modulators.

2.2.1 Optical Waveguides

Optical waveguides provide light guidance and confinement, in SiPh they are typically implemented on silicon-on-insulator (SOI) substrates, where a thin crystalline silicon layer is separated from the silicon substrate by a buried oxide layer, enabling strong optical confinement due to the high refractive index contrast [1].

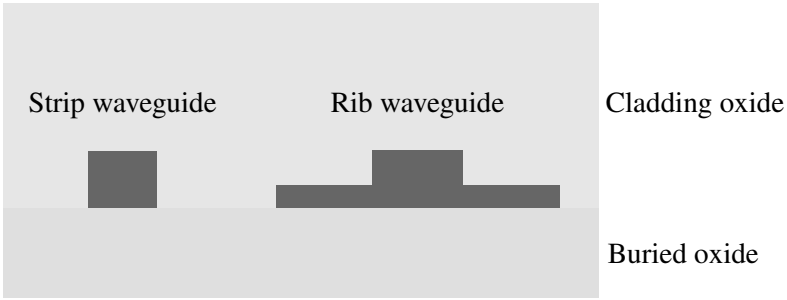


Figure 2.1: Strip and rib waveguides cross sections based on [1, Ch. 3].

The most common waveguide geometries are strip and rib waveguides, in Figure 2.1. Strip waveguides offer tight confinement and small bend radii, making them well suited for dense routing, while rib waveguides retain a silicon slab that facilitates electrical access and are therefore preferred in active devices such as modulators [1]. With appropriate design and fabrication, both geometries can achieve low propagation loss, supporting large-scale integration in silicon photonic systems [1].

Guided modes are solutions of Maxwell's equations that characterise the light propagation in the waveguide.

$$\mathbf{E}(x,y,z,t) = \mathbf{e}(x,y)\exp(j\beta z)\exp(-j\omega t) \tag{2.4}$$

where $\mathbf{e}(x,y)$ is the transverse field distribution and β the propagation constant.

Often the waveguide is described by the effective index n_{eff} which is related to β by the vacuum wavenumber k_0

$$k_0 = \omega\sqrt{\varepsilon_0\mu_0} = \frac{2\pi}{\lambda_0} \tag{2.5}$$

$$\beta = k_0 n_{\text{eff}} \tag{2.6}$$

For a guided mode, β must take a value between the wavenumbers of the core and cladding regions. Equivalently, in terms of the effective index, this requires [9, Ch. 3, Sec. 3.4.2]

$$n_{\text{clad}} < n_{\text{eff}} < n_{\text{core}}, \tag{2.7}$$

The value of β for a given mode is obtained as the eigenvalue of the Helmholtz equation solved over the waveguide cross-section, subject to the boundary conditions —set by materials and geometry of regions.

SiPh waveguides —SiO_2 cladding and Si core —are limited to a width up to 500 nm at 220 nm thickness to maintain single mode operation due to the confinement condition Eq. 2.7. As the waveguide width and thickness increases, the optical confinement also increases, eventually allowing higher-order modes to propagate. [1, Ch. 3.2].

An optical mode in a SiPh rib waveguide is illustrated in Fig. 2.2.

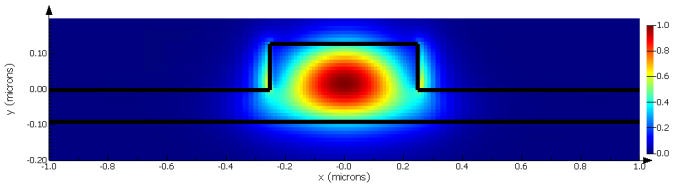


Figure 2.2: Electric field intensity (linear scale) of the fundamental guided mode in a rib waveguide, simulated using Ansys Lumerical MODE.

Single-mode operation is generally preferred in photonic integrated circuits because it eliminates modal dispersion and modal interference, leading to predictable propagation characteristics, lower losses, and simpler design of passive and active photonic devices.

The phase velocity v_p determines how the peaks of a monochromatic optical field propagate and is determined by the effective index n_{eff}.

$$v_p = \frac{\omega}{\beta} = \frac{c}{n_{\text{eff}}} \tag{2.8}$$

The group velocity v_g determines the speed of propagation of the optical signal envelopes and is determined by the group index n_g.

$$v_g = \frac{d\omega}{d\beta} = \frac{c}{n_g} \tag{2.9}$$

where

$$n_g = n_{\text{eff}} - \lambda \frac{dn_{\text{eff}}}{d\lambda} \tag{2.10}$$

2.2.2 Y-Branch Splitters and Combiners

Y-branch structures, illustrated in Fig. 2.3, are used to split light from a single input waveguide into two output waveguides, or reciprocally combine light from two waveguides into a single output. An ideal Y-branch acts as a 50/50 splitter, with input output relations (2.11) from [1, Ch. 4.2].

$$\begin{aligned} I_{out,1} &= I_{out,2} = \frac{1}{2} I_{in} \\ E_{out,1} &= E_{out,2} = \frac{1}{\sqrt{2}} E_{in} \end{aligned} \tag{2.11}$$

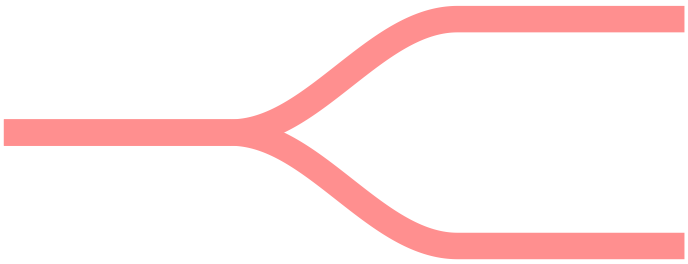


Figure 2.3: Y-branch splitter/combiner diagram based on [1, Ch. 4].

where I represents optical intensity and E field amplitudes — both for the input and output ports — related by $I \propto |E|^2$.

When the device functions as a combiner the constructive and destructive interference of the two input field amplitudes needs to be considered, since in-phase inputs can fully combine in the fundamental mode of the output waveguide whilst out-of-phase inputs result in no power at the fundamental mode of the waveguide. Note that the power doesn't disappear, it needs to be redistributed to higher-order modes or radiation modes. The interference at the output of combiners is essential for the operation of MZI's.

Practical devices exhibit some excess loss due to fabrication imperfections and non-ideal mode overlap, typically optimized using numerical methods such as FDTD simulations [1].

2.2.3 Directional couplers

Directional couplers are fundamental building blocks in integrated photonics and are formed by bringing two single-mode waveguides into close proximity over a finite interaction length, allowing power exchange via evanescent coupling [1]. The optical behavior of such structures is accurately described by coupled-mode theory, where the system eigenmodes are the symmetric and antisymmetric supermodes of the coupled waveguides [1].

The power coupling strength depends exponentially on the waveguide separation and sinusoidally on the interaction length, while the through- and cross-coupled field amplitudes satisfy the power conservation relation

$$|t|^2 + |\kappa|^2 = 1, \tag{2.12}$$

for a lossless directional coupler [1]. Here, t and κ denote the field transmission and coupling coefficients, respectively.

Importantly, the symmetric and antisymmetric supermodes exhibit a relative π phase difference between the fields in the two waveguides. When the fields are recombined into the original waveguide basis, this phase difference results in a fixed $\pi/2$ phase shift between the through and cross ports [1]. Consequently, the coupling coefficient is purely imaginary, while the through coefficient may be chosen real without loss of generality.

If the propagation phase accumulated inside the coupling region is accounted for separately—as is customary in compact circuit models and ring resonator analysis—the directional coupler can

be represented by the unitary scattering matrix [1]

$$\begin{pmatrix} E_{\text{out},1} \\ E_{\text{out},2} \end{pmatrix} = \begin{pmatrix} t & i\kappa \\ i\kappa & t \end{pmatrix} \begin{pmatrix} E_{\text{in},1} \\ E_{\text{in},2} \end{pmatrix}, \tag{2.13}$$

where $t \in \mathbb{R}$ and $\kappa \in \mathbb{R}$.

This representation is widely used in photonic circuit modeling and is adopted throughout this work, as it captures both power conservation and the intrinsic 90° phase shift introduced by directional coupling, while allowing propagation phases to be treated independently [1].



Figure 2.4: Signal-flow graphs of an ideal directional coupler. The graph on the left follows the physical port ordering whilst the graph on the right doesn't as a trade-off for having no crossing arrows

Figure 2.4 shows two equivalent signal-flow graph representations of an ideal directional coupler. Nodes represent complex optical field amplitudes, while directed edges represent linear field transformations with coefficients t and $i\kappa$.

2.3 PN-Junction Phase Shifters

Carrier-depletion phase shifters based on reverse-biased pn-junctions are among the most widely used phase-modulation structures in silicon photonics. These devices rely on the plasma dispersion effect, discussed in Section 2.1, which shows how changes in the free-carrier concentration modify the refractive index. The analysis of these devices in this section follows the formulation presented in [1, Ch. 6].

A schematic cross-section of a pn-junction phase shifter is illustrated in Fig. 2.5, consisting of adjacent p and n doped regions, with a depletion region in the junction interface. Under reverse bias, the applied voltage increases the width of the depletion region, modifying the spatial distribution of free carriers near the optical mode.

The model in Fig 2.5 assumes an abrupt impurity profile change across the doping boundary with a depletion region width W_d shown in Eq. (2.14) from [1].

$$W_d(V) = \sqrt{\frac{2\varepsilon_0\varepsilon_s}{q}\frac{(N_A+N_D)}{N_A N_D}(V_{bi}-V)}, \qquad V_{bi} = \frac{k_B T}{q}\ln\left(\frac{N_A N_D}{n_i^2}\right) \tag{2.14}$$

where N_A, N_D are the impurity densities, V_{bi} the diffusion potential of the junction and ε_s the relative permittivity.

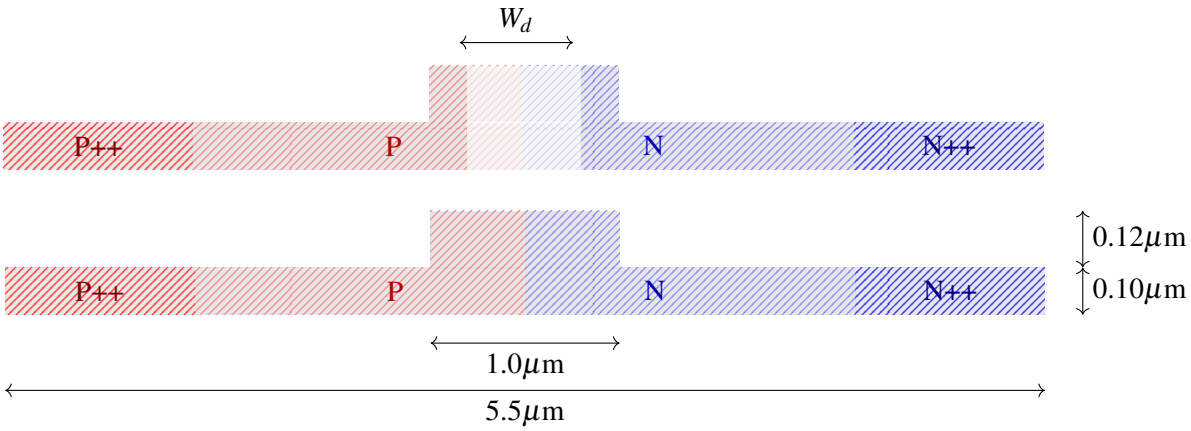


Figure 2.5: PN junction cross-section with and without the depletion region based on [1, Ch. 6]

The local refractive index change is given by the carrier distribution through Eq. (2.3), whilst the effective index change is given by the overlap between the optical mode $e(x,y)$ and this local changes in the core index n_{core}, shown in Eq. (2.15).

$$\Delta n_{\text{eff}}(V) = \frac{\iint e^*(x,y) n_{\text{core}}(x,y,V) e(x,y)\, dA}{\iint |e(x,y)|^2\, dA}, \tag{2.15}$$

This voltage-induced variation of the effective index produces a phase shift

$$\Delta\phi(V) = \frac{2\pi}{\lambda} \Delta n_{\text{eff}}(V) L \tag{2.16}$$

where L is the length of the phase shifter.

2.3.1 PN-junction Figures of Merit

The objective of a depletion-mode phase shifter is to maximize the voltage-induced change in n_{eff} while minimizing optical loss. Several figures of merit can be used to quantify the performance of the phase shifter.

Total effective index change as a function of voltage

$$\Delta n_{\text{eff}}(V) \tag{2.17}$$

Effective-index tuning efficiency quantifies the sensitivity of the effective refractive index to changes in the applied voltage, and is defined in this work as

$$\left.\frac{dn_{\text{eff}}}{dV}\right|_{V_0} \tag{2.18}$$

The derivative is evaluated at a local operating voltage V_0 and therefore represents the local change in effective index per unit change in voltage.

Voltage–length product According to Eq. 2.16 a π phase shift is obtained for an index change

$$\Delta n_{\text{eff}} = \frac{\lambda}{2L}$$

Assuming the effective index varies approximately linearly with the applied voltage over the operating range, the voltage–length product is

$$V_\pi L = \frac{\lambda}{2}\left(\frac{\Delta n_{\text{eff}}}{\Delta V}\right)^{-1} \tag{2.19}$$

alternatively it can be computed at a local operating voltage V_0 as

$$(V_\pi L)_{\text{local}}(V_0) = \frac{\lambda}{2}\left(\frac{dn_{\text{eff}}}{dV}\right)^{-1} \tag{2.20}$$

2.3.2 Speed Limitations and RC Effects

The high-speed performance of pn-junction phase shifters is primarily limited by the junction resistance and capacitance. The junction capacitance C_j can be obtained from the capacitance definition

$$C_j(V) = \frac{dQ(V)}{dV} \tag{2.21}$$

which would require the integration of the total charge Q across the phase shifter, or it can also be obtained from a small-signal analysis, with voltage perturbation V_{ac}, around a operating point V_{DC}

$$C_j(\omega) = \frac{\Im\{Y(\omega)\}}{\omega} \tag{2.22}$$

where ω is the small-signal perturbation angular frequency and Y the admittance. From this analysis the junction series resistance can also be obtained

$$R_j(\omega) = \Re\{\frac{1}{Y(\omega)}\} \tag{2.23}$$

As shown in [1, Ch. 6, Sec. 6.2], the RC time constant determines the intrinsic electrical bandwidth f_{τ_j}:

$$\begin{aligned} \tau_j &= R_j C_j \\ f_{\tau_j} &= \frac{1}{2\pi\tau_j}. \end{aligned} \tag{2.24}$$

An increase in the applied reverse bias voltage increases the depletion region and leads to a decrease of R_j and C_j and an increase in f_{τ_j}, which can easily exceed tens of GHz, and therefore is

usually not the limiting factor on modulator bandwidths though, for large phase shifters like those required for MZM's the increase in the capacitance C_j can be a problem [1].

The junction capacitance also directly determines the electrical energy required to switch the phase shifter. Assuming a capacitive load and a voltage switch of ΔV between states the dynamic energy consumed per bit is

$$\mathrm{E_{bit}} = \frac{1}{2} C_j \Delta V^2 \tag{2.25}$$

2.4 Mach-Zehnder Modulator

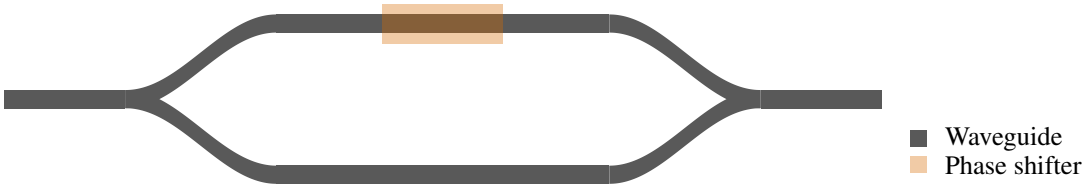


Figure 2.6: Mach-Zehnder interferometer diagram based on [1, Ch. 4].

Mach–Zehnder interferometers (MZI) are a fundamental photonic device used to control and measure optical phase differences. It consists of an input wave split into two arms, which are later recombined at a second splitter. The splitting and recombining can be realized using Y-branches or directional couplers, illustrated in Fig. 2.6 [1].

Transfer Function Following the derivation in Chrostowski and Hochberg [1, Ch. 4], for an ideal, lossless MZI with symmetric 50:50 beam splitters, the input electric field E_{input} is split equally between the upper and lower arms:

$$E_1 = \frac{E_{input}}{\sqrt{2}}, \quad E_2 = \frac{E_{input}}{\sqrt{2}}. \tag{2.26}$$

The fields propagate through the waveguides, accumulating different phase shifts $\Delta\phi_1$ and $\Delta\phi_2$ in each arm due to the optical path difference, or in MZMs due to a change in the refractive index from a phase shifter.

$$E_{o1} = E_1 e^{j\Delta\phi_1}, \quad E_{o2} = E_2 e^{j\Delta\phi_2}. \tag{2.27}$$

Recombining at the second splitter gives the output field:

$$\begin{aligned} E_{output} &= \frac{1}{\sqrt{2}} (E_{o1} + E_{o2}) \\ &= E_{input} \frac{1}{2} \left(e^{j\Delta\phi_1} + e^{j\Delta\phi_2} \right) \\ &= E_{input} \cdot e^{j\left(\frac{\Delta\phi_1 + \Delta\phi_2}{2}\right)} \cos\left(\frac{\Delta\phi_1 - \Delta\phi_2}{2} \right). \end{aligned} \tag{2.28}$$

The output intensity, obtained by squaring the magnitude of the output field, is:

$$I_{output} = |E_{output}|^2 = I_{input} \cos^2\left(\frac{\Delta\phi_1 - \Delta\phi_2}{2}\right). \tag{2.29}$$

This formulation explicitly follows the derivation given in Chrostowski [1, Ch .4], showing that the MZM output is controlled by the relative phase difference between the two arms and demonstrating that the intensity transmission is sinusoidal in relation to the phase difference between the arms, as seen in Figure 2.7.

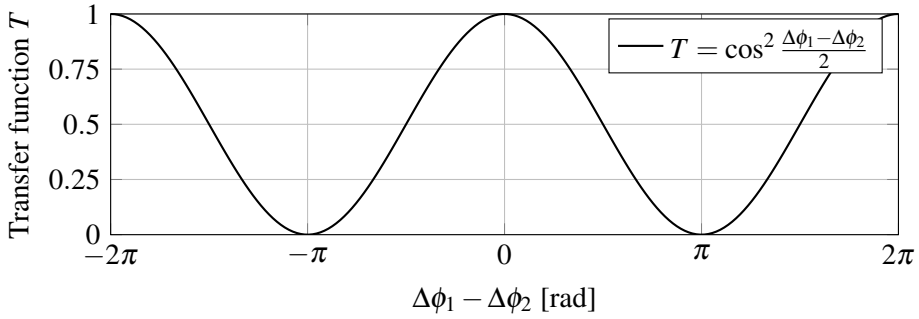


Figure 2.7: Mach–Zehnder Modulator Interferometer transfer function.

The phase shift in each arm is given by the equation (2.30) where β is the propagation constant

$$\Delta\phi_i = \beta L_i, \qquad \beta = \frac{2\pi n_{eff}}{\lambda_0} \tag{2.30}$$

MZMs utilize phase shifters in the arms to electronically control the transmission between constructive and destructive interference , allowing for the modulation of the light intensity and with more complexity also coherent modulation.

Assuming in an MZM both arms have the same length L the difference between phase shifts in each arm becomes

$$\Delta\phi_1 - \Delta\phi_2 = -j(\beta_1 - \beta_2)L = -j\frac{2\pi}{\lambda_0}(n_1 - n_2)L, \tag{2.31}$$

meaning it scales linearly with the refractive index difference between arms $n_1 - n_2$ and the length of the arms L. This indicates that the $\Delta\phi_1 - \Delta\phi_2$ swing from 0 to $\pm\pi$ limits the possible values for L and the strength of the refractive index change.

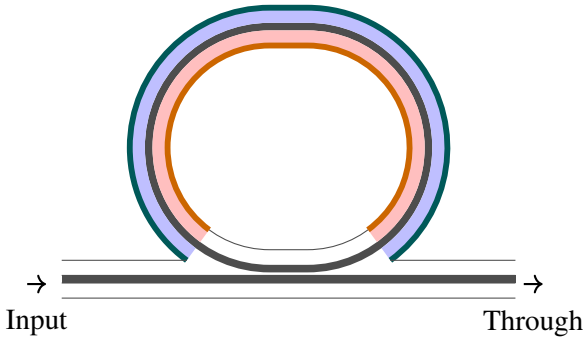
The above limitations related to its effectiveness, size footprint and drive voltages stem from MZMs being phase accumulation devices.

2.5 Microring Resonator Modulators

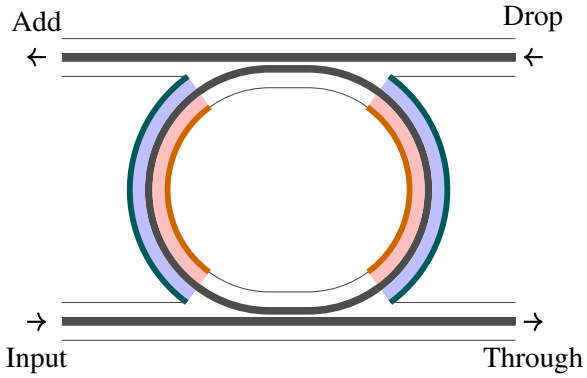
Microring resonators are among the most widely used building blocks in integrated photonics due to their compact footprint and wavelength selectivity, having a wide scope of applications

from filters, multiplexing/demultiplexing channels, and as compact modulators. The theoretical framework presented here follows the formalism introduced in [1].

Fig. 2.8 illustrates ring modulators, with a racetrack loop, in the all-pass and add-drop configurations.



(a) All-pass ring modulator.



(b) Add-drop ring modulator.

Figure 2.8: Diagram of ring/racetrack resonators based on [1, Ch. 4].

Wavelength resonance constitutes the operating principle of ring resonators, where minor variations in refractive index yield substantial alterations in transmission. This augmented sensitivity emanates from the quality factor Q of the resonant cavity, in contrast to MZIs, whose modulation efficacy escalates linearly with interaction length L. Consequently, microring resonators are capable of attaining pronounced modulation within a compact spatial footprint, while MZMs would require a larger footprint and driving voltages to modulate n.

2.5.1 Ring Geometry and Round-Trip Parameters

As depicted in Fig. 2.8 ring resonators consist of an optical cavity — closed-loop waveguide — coupled to one or more bus waveguides.

Following the analysis in [1, Ch. 4], the racetrack geometry has a total round-trip length

$$L_{\mathrm{rt}} = 2\pi r + 2L_c, \tag{2.32}$$

where r is the bend radius of the curved sections and L_c is the length of each straight coupling section. If L_c were equal to zero the resonator is said to be point-coupled to the bus, having a ring geometry instead of a racetrack geometry.

The optical field accumulates both phase and loss over a round trip. The round-trip phase

$$\phi_{\text{rt}} = \beta L_{\text{rt}}, \qquad \beta = \frac{2\pi}{\lambda_0} n_{eff} \tag{2.33}$$

in which β is the propagation constant, n_{eff} the effective index of the guided mode, and λ_0 the vacuum wavelength.

The round-trip time of an optical signal T_{rt} can be defined from the ring length given the group velocity of the optical waveguide that composes the ring modulator.

$$T_{\text{rt}} = \frac{L_{\text{rt}}}{v_g} \tag{2.34}$$

Propagation loss in the ring is captured by the round-trip power attenuation factor

$$A_{rt} = e^{-\alpha L_{\text{rt}}} \tag{2.35}$$

with α denoting the power attenuation coefficient of the waveguide [1, Ch. 4].

2.5.2 Cavity Energy and Photon Lifetime

Since the microring is a resonator, it stores energy E_{stored} in the circulating optical field within the cavity. The stored energy increases due to the optical power coupled into the ring and decreases due to intrinsic propagation losses and power coupled out of the resonator.

Intrinsic propagation loss: Assuming no input power and waveguide absorption as the only loss mechanism, E_{stored} is reduced by a factor of A_{rt} per round trip, which occur every T_{rt} seconds.

$$E_{\text{stored}}(t + T_{\text{rt}}) = A_{\text{rt}} E_{\text{stored}}(t)$$

The discrete round-trip decay can be expressed as a continuous function of time,

$$E_{\text{stored}}(t) = E_{\text{stored}}(0)\,(A_{\text{rt}})^{t/T_{\text{rt}}} = E_{\text{stored}}(0) \exp\left(\frac{t}{T_{\text{rt}}} \ln A_{\text{rt}}\right), \qquad t \geq 0 \tag{2.36}$$

Or by defining the intrinsic photon lifetime τ_i and substituting Equations (2.35) and (2.34):

$$E_{\text{stored}}(t) = E_{\text{stored}}(0) \exp\left(-\frac{t}{\tau_i}\right), \qquad t \geq 0, \qquad \frac{1}{\tau_i} = -\frac{\ln A_{\text{rt}}}{T_{\text{rt}}} = \alpha v_g \tag{2.37}$$

Coupling losses: Assuming no input power and out-coupling of power as the only loss mechanism, only a fraction $|t|^2$ — through-coupling coefficient presented in Sec. 2.2.3—of the stored energy E_{stored} remains in the ring after each round trip, since after one round trip all cross-sections of the traveling wave pass through the coupler.

By thinking of $|t|^2$ as a round trip coupling loss A_c we obtain:

$$E_{\text{stored}}(t+T_{\text{rt}}) = A_c E_{\text{stored}}(t), \qquad A_c = |t|^2$$

Following the same steps as the instrinic propagation loss the coupling loss lifetime τ_c is:

$$E_{\text{stored}}(t) = E_{\text{stored}}(0)\exp\left(-\frac{t}{\tau_c}\right), \qquad t \geq 0, \qquad \frac{1}{\tau_c} = -\frac{\ln|t|^2}{T_{\text{rt}}} \tag{2.38}$$

The photon lifetime τ_{ph} is determined by the combined contributions from these distinct loss mechanisms, with the corresponding total decay rate given by in Eq. (2.39).

$$\frac{1}{\tau_{\text{ph}}} = \frac{1}{\tau_c} + \frac{1}{\tau_d} + \frac{1}{\tau_i} \tag{2.39}$$

where:

- $1/\tau_c$: Decay rate due to external coupling to the through port (transmitted wave)
- $1/\tau_d$: Decay rate due to coupling to the drop port in add-drop microring configurations
- $1/\tau_i$: Decay rate due to intrinsic losses (absorption, scattering, radiation)

$$E_{\text{stored}}(t) = E_{\text{stored}}(0)\exp\left(-\frac{t}{\tau_{\text{ph}}}\right), \qquad t \geq 0 \tag{2.40}$$

$$P_{\text{loss}} = -\frac{dE_{\text{stored}}}{dt} = \frac{E_{\text{stored}}}{\tau_{\text{ph}}} \tag{2.41}$$

The exponential decay of the stored energy E_{stored} is therefore given by Eq. (2.40), with the corresponding power loss (2.41).

The photon lifetime therefore provides a direct measure of the characteristic timescale over which the energy stored in the resonator decays in the absence of external excitation.

A related and widely used parameter for characterizing resonator is the quality factor Q, which quantifies the ability of the resonator to store optical energy relative to the energy lost per optical cycle, defined as

$$Q = \omega_0 \frac{E_{\text{stored}}}{P_{\text{loss}}} \tag{2.42}$$

where ω_0 is the resonance angular frequency. Substituting Eq. 2.41 into this definition gives

$$Q = \omega_0 \tau_{\text{ph}} \tag{2.43}$$

It follows also that the quality factor can be separated into contributions from each loss mechanism and the formulation of each one is given by [1, Ch. 6] considering an all-pass configuration.

$$Q^{-1} = Q_c^{-1} + Q_i^{-1}, \qquad Q_i = \omega_0 \tau_i = \frac{2\pi n_g}{\lambda \alpha}, \qquad Q_c = \omega_0 \tau_c = -\frac{\pi L_{\text{rt}} n_g}{\lambda \ln|t|} \tag{2.44}$$

2.5.3 Resonance condition and parameters

The resonance condition of the microring arises when the round-trip phase satisfies $\phi_{\text{rt}} = 2\pi m$, with $m \in \mathbb{Z}$, substituting ϕ_{rt} in Eq. (2.33) gives Eq. (2.45) where λ_m is the m-th resonance.

$$\lambda_m m = n_{eff}(\lambda_m) L_{\text{rt}} \tag{2.45}$$

At resonance, the traveling wave inside the ring constructively interferes with itself meanwhile the out-coupled wave destructively interferes with the input wave, leading to strong amplitude modulation in the output port.

The free spectral range FSR is defined by the spectral distance between resonances $\text{FSR}_\lambda = \lambda_m - \lambda_{m+1}$ for any $m \in \mathbb{Z}$, being however wavelength dependent due to the change in refractive index. The FSR of the resonator and group index n_g of the waveguide are related through equation (2.46) from [1, Ch. 4].

$$\text{FSR}_f = \frac{c}{n_g L_{\text{rt}}}, \qquad \text{FSR}_\lambda \approx \frac{\lambda^2}{L_{rt} \cdot n_g} \tag{2.46}$$

where FSR_f and FSR_λ denote the free spectral range in the frequency and wavelength domains

The conversion between frequency and wavelength domains uses the standard first-order approximation (2.47) obtained from $f = \frac{c}{\lambda}$ by linearization around a center wavelength λ.

$$\Delta f \approx c \frac{\Delta\lambda}{\lambda^2}, \qquad \Delta\lambda \ll \lambda \tag{2.47}$$

Resonance linewidth and photon lifetime In the absence of external excitation the energy stored decays according to Eq. (2.40), the corresponding electric field amplitude at resonance decays as

$$E(t) = E(0) \exp\left(-\frac{t}{2\tau_{\text{ph}}}\right) \exp(j\omega_0 t), \qquad t \geq 0 \tag{2.48}$$

where ω_0 is the resonance angular frequency. The cavity therefore exhibits a finite temporal memory since after the excitation is removed, the stored energy persists as a decaying tail. This limits how rapidly the cavity can be switched between successive states without intersymbol interference.

The spectral response of (2.48) is obtained taking its Fourier transform,

$$\begin{aligned} \mathscr{F}\{E\}(\omega) &= \int_0^\infty E(t) e^{-j\omega t} dt = E(0) \int_0^\infty \exp\left(-j(\frac{t}{2\tau_{\text{ph}}} + j(\omega - \omega_0))t\right) dt \\ &= \frac{E(0)}{\frac{1}{2\tau_{\text{ph}}} + j(\omega - \omega_0)} \end{aligned} \tag{2.49}$$

Normalizing the spectral intensity $|\mathscr{F}\{E\}(\omega)|^2$ obtained from Eq. (2.49) yields the Lorentzian lineshape

$$S(\omega) = K\frac{1}{(\frac{1}{2\tau_{\text{ph}}})^2 + (\omega-\omega_0)^2}, \qquad K = \frac{1}{(2\tau_{\text{ph}})^2} \tag{2.50}$$

The normalized spectral intensity is illustrated in Fig. 2.9. The spectral intensity reaches its maximum value at $\omega = \omega_0$ and the half-maximum

$$S(\omega) = \frac{1}{2}S(\omega_0)$$

occurs when

$$|\omega - \omega_0| = \frac{1}{2\tau_{\text{ph}}}$$

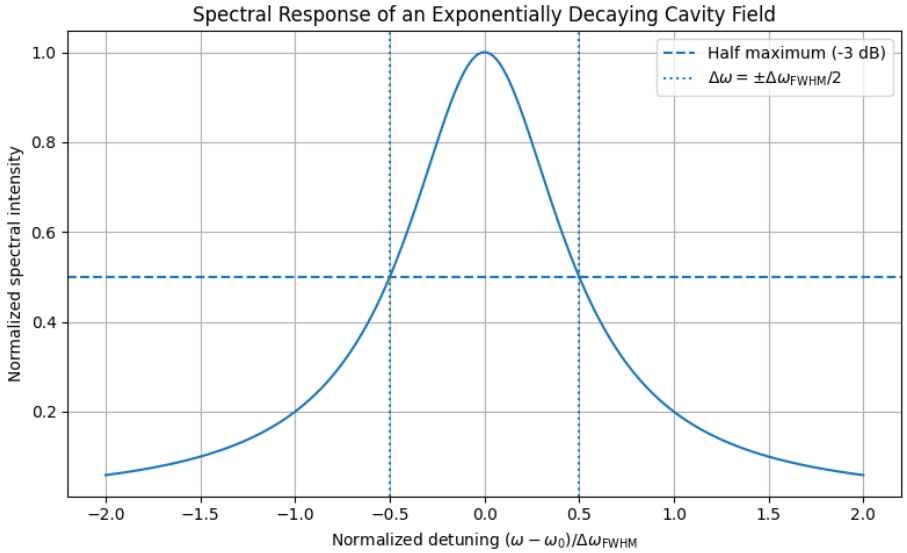


Figure 2.9: Normalized spectral intensity obtained from the Fourier transform of an exponentially decaying resonant cavity field.

Therefore the full width at half maximum (FWHM), equivalently the 3-dB linewidth, is

$$\Delta\omega_{\text{FWHM}} = \frac{1}{\tau_{\text{ph}}} \tag{2.51}$$

equivalently we can write Eq. (2.51) in terms of the cutoff frequency $f_{\tau_{ph}}$ defined in [1, Ch. 6].

$$f_{\tau_{\text{ph}}} = \frac{1}{2\pi\tau_{\text{ph}}}, \qquad \Delta\omega_{\text{FWHM}} = 2\pi\Delta f_{\text{FWHM}} = 2\pi f_{\tau_{\text{ph}}} \tag{2.52}$$

Modulating a microring at a modulation rate corresponding to the 3-dB linewidth, implies that one photon lifetime elapses per symbol. Consequently the stored energy inside decays by a factor of e^{-1}, approximately 36% of its value before the arrival of the next symbol.

The 3-dB linewidth is taken as the characteristic modulation bandwidth achievable, although higher modulation frequencies could be achieved, albeit with a increase in the inter-symbol interference.

Substituting (2.51) into (2.43), and utilizing Eq. (2.47) to convert frequency ranges into wavelength ranges yields

$$Q = \frac{\omega_0}{\Delta\omega_{\text{FWHM}}} = \frac{f_0}{\Delta f_{\text{FWHM}}} \approx \frac{\lambda_0}{\Delta\lambda_{\text{FWHM}}} \tag{2.53}$$

This is a useful equation to relate the quality factor to the linewidth and achievable bandwidth.

Intensity Modulation Microring resonator modulators exploit the strong dependence of ϕ_{rt} on the effective index n_{eff} (2.33) by utilizing pn-junction phase shifters to modulate n_{eff} and in turn modulate strongly the amplitude response, ideal for PAM modulation.

By applying an electrical control signal—typically via carrier injection, carrier depletion, or the thermo-optic effect—the effective index of the ring waveguide is altered, shifting the resonance wavelength. When the input laser wavelength is biased on the slope of a resonance, small index changes result in large variations in transmitted optical power, enabling efficient intensity modulation. This resonant enhancement allows microring modulators to achieve low energy per bit and compact device footprints, at the cost of increased sensitivity to wavelength detuning and temperature variations, as discussed in [1].

2.5.4 Transmission transfer functions

The resonant behavior of the microring can also be characterised in the frequency domain through the transmission transfer functions. These functions describe the steady-state relationship between the input and output, without temporal evolution of the cavity field or associated memory effects. The transfer functions for the all-pass and add-drop configurations are derived below from the corresponding signal flow graphs.

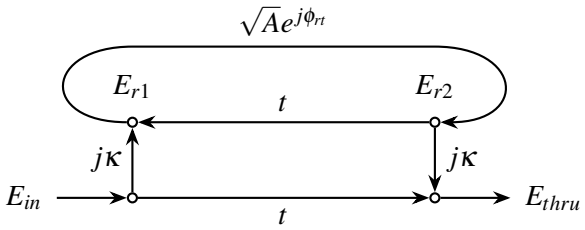


Figure 2.10: Signal-flow graph of an all-pass microring resonator modulator.

All-pass microring resonator: In the all-pass configuration, the ring is coupled to a single bus waveguide. The corresponding signal-flow graph is shown in Figure 2.10 composed of a directional coupler and a round-trip field loss $\sqrt{A_{rt}}$ and phase shift $\exp(j\phi_{rt})$.

By summing all circulating field contributions in the ring, the normalized through-port transfer function can be written as equation (2.54), illustrated by Fig. 2.12, adapted from [1]

$$\frac{E_{\text{thru}}}{E_{\text{in}}} = \frac{-\sqrt{A_{rt}} + te^{-j\phi_{\text{rt}}}}{-\sqrt{A_{rt}}t + e^{-j\phi_{\text{rt}}}}, \tag{2.54}$$

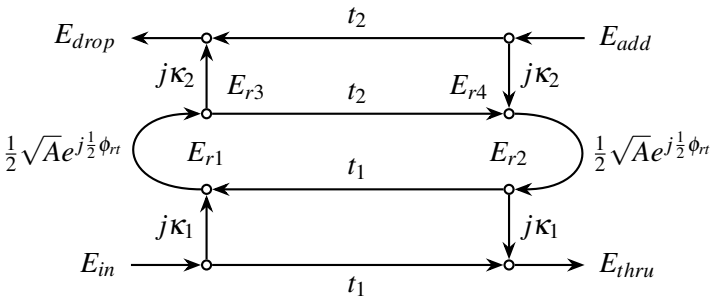


Figure 2.11: Signal-flow graph of an add-drop microring resonator modulator.

Add-drop microring resonator In the add-drop configuration, shown in Figure 2.11, the ring is coupled to two bus waveguides via two directional couplers. The normalized through-port and drop-port transfer functions obtained from the signal graph are given by the Equations (2.55) and (2.56) adapted from [1].

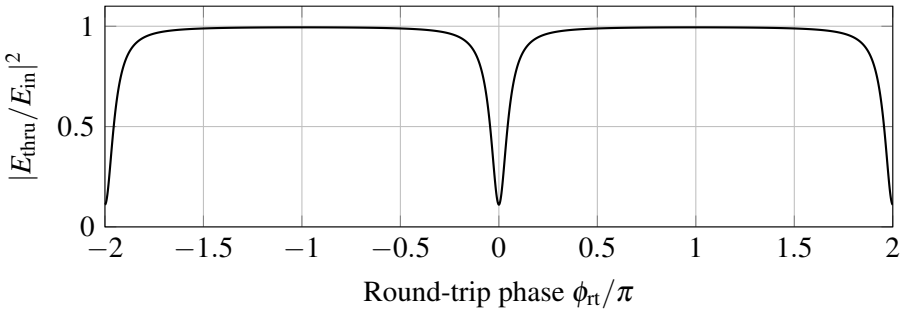


Figure 2.12: Power transmission of the all-pass microring resonator through port as a function of the round-trip phase ϕ_{rt} with $A_{\text{rt}} = 0.9$ and $t = 0.9$.

$$\frac{E_{\text{thru}}}{E_{\text{in}}} = \frac{t_1 - t_2\sqrt{A_{rt}}e^{j\phi_{\text{rt}}}}{1 - \sqrt{A_{rt}}t_1t_2e^{j\phi_{\text{rt}}}}, \tag{2.55}$$

$$\frac{E_{\text{drop}}}{E_{\text{in}}} = \frac{-\kappa_1\kappa_2A_{rt}^{1/4}e^{j\phi_{\text{rt}}/2}}{1 - \sqrt{A_{rt}}t_1t_2e^{j\phi_{\text{rt}}}}, \tag{2.56}$$

At resonance, optical power is efficiently transferred from the input waveguide to the drop port, while the through-port transmission is minimized. The power transmission responses of the transfer functions in Eqs. (2.55)–(2.56) are illustrated in Figs. 2.13–2.14 respectively.

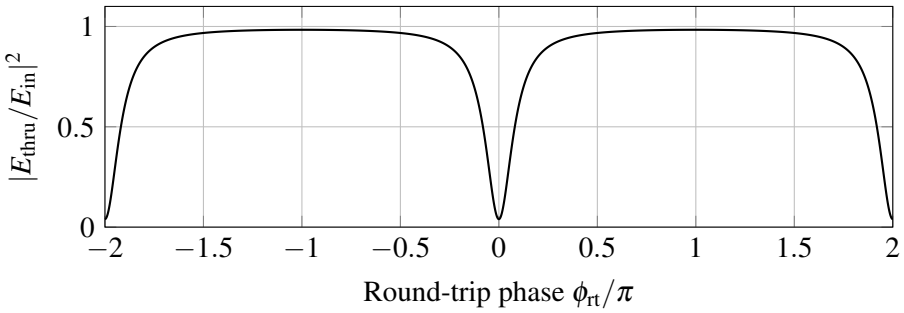


Figure 2.13: Power transmission of the add-drop microring resonator through port as a function of the round-trip phase ϕ_{rt} with $A_{\text{rt}} = 0.9$ and $t_1 = t_2 = 0.9$.

2.5.5 Coupled Mode Theory of Ring Resonators

A microring resonator can be described using *Coupled Mode Theory (CMT)* in the time domain, where the ring is treated as a *lumped oscillator* with energy amplitude $a(t)$ and total energy stored $E_{\text{stored}}(t)$ [3].

$$E_{\text{stored}}(t) = |a(t)|^2 \tag{2.57}$$

The normalized traveling wave $A(t)$, input $s_i(t)$, and through port waves $s_t(t)$, as the amplitudes for the power in an arbitrary cross-section of the ring, input port and output port, respectively, are also defined with the relations below.

$$P_{\text{ring}} = |A(t)|^2, \qquad P_{\text{i}} = |s_i(t)|^2, \qquad P_{\text{t}} = |s_t(t)|^2 \tag{2.58}$$

where P_{ring}, P_{i} and P_{t} are the power flowing through any cross-section of the ring, the input power and output power respectively.

The traveling wave $A(t)$ inside the ring can be converted to the energy amplitude of the discrete lumped oscillator through the equation (2.59) adapted from [3] where the round-trip time is the conversion factor between power and energy.

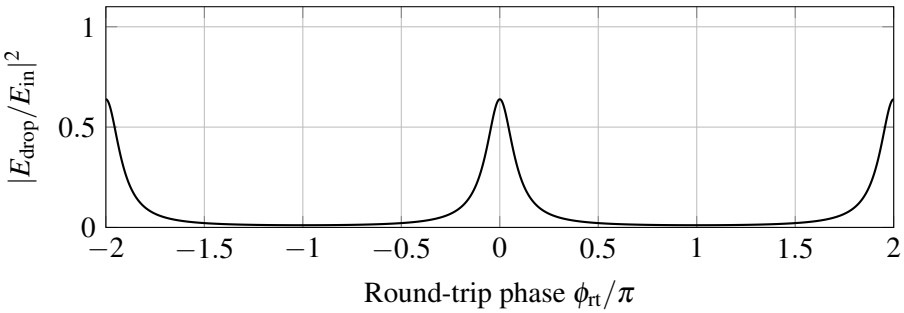


Figure 2.14: Power transmission of the add-drop microring resonator drop port as a function of the round-trip phase ϕ_{rt} with $A_{\text{rt}} = 0.9$ and $t_1 = t_2 = 0.9$.

$$|a(t)|^2 = |A(t)|^2 T_{\text{rt}} = |A(t)|^2 \frac{L_{rt}}{v_g} \qquad \Longleftrightarrow \qquad E_{\text{stored}} = P_{\text{ring}} T_{\text{rt}} \tag{2.59}$$

In this way the continuous cavity resonator is simplified to a lumped element.

Time Evolution and Coupling Equations The temporal evolution of the energy amplitude $a(t)$ is represented by the first-order differential equation (2.60), adapted from [3]. Here, τ_{ph} denotes the photon lifetime of the cavity and τ_c the coupling lifetime associated with the losses of the external optical field that couple into the cavity. The imaginary factor j arises from the convention used for the lossless directional coupler in Sec. 2.2.3.

$$\frac{d}{dt}a(t) = \left(j\omega_0 - \frac{1}{2\tau_{ph}}\right) a(t) - j\sqrt{\frac{1}{\tau_c}} s_i(t) \tag{2.60}$$

The output port relation (2.61), from [3] is easily obtained by considering the time reversal symmetry, with the power coupling from the ring to the through port.

$$s_t(t) = s_i(t) - j\sqrt{\frac{1}{\tau_c}} a(t) \tag{2.61}$$

The exponential decay factor $-\frac{1}{2\tau_{ph}}$ in (2.60) is chosen such that it matches with the definition of the photon lifetime as the decay factor of the stored energy in the ring (2.41) from [10, Ch. 4.7].

Homogeneous Solutions Derivation The homogeneous solutions, where $s_i(t) = 0$, for the $E_{\text{stored}}(t)$ and $a(t)$ differential equations are given by (2.62) which can be verified by confirming the amplitude wave to power relation (2.57) holds.

$$\begin{aligned} a(t) &= a(0)\exp(-\frac{t}{2\tau_{ph}})\exp(j\omega_0 t) \\ E_{\text{stored}}(t) &= E_{\text{stored}}(0)\exp(-\frac{t}{\tau_{ph}}) \end{aligned} \tag{2.62}$$

The energy in the ring exponentially decays if there is no input power, as described in Sec. 2.5.3.

CW Laser Solutions Derivation In microring modulators the laser *is not directly modulated* meaning $s_i(t)$ is known to be a CW input with lasing frequency ω_L and amplitude $\sqrt{P_i}$.

$$s_i(t) = \sqrt{P_i}\exp(j\omega_L t) \tag{2.63}$$

Substituting (2.63) into (2.60) we obtain:

$$\frac{d}{dt}a(t) = \left(j\omega_0 - \frac{1}{2\tau_{\text{ph}}}\right) a(t) - j\sqrt{\frac{1}{\tau_c}}\sqrt{P_i} e^{j\omega_L t} \tag{2.64}$$

This adds a driving term oscillating at frequency ω_L. To solve it, we assume a steady-state solution oscillating at the same frequency as the drive: $a(t) = a_0 e^{j\omega_L t}$, where a_0 is the complex amplitude of the resonator field in steady-state.

$$
\begin{aligned}
& j\omega_L a_0 e^{j\omega_L t} = \left(j\omega_0 - \frac{1}{2\tau_{\text{ph}}}\right) a_0 e^{j\omega_L t} - j\sqrt{\frac{1}{\tau_c}}\sqrt{P_i} e^{j\omega_L t} \\
\Leftrightarrow\ & j\omega_L a_0 = j\omega_0 a_0 - \frac{1}{2\tau_{\text{ph}}} a_0 - j\sqrt{\frac{1}{\tau_c}}\sqrt{P_i} \\
\Leftrightarrow\ & \left[j(\omega_L - \omega_0) + \frac{1}{2\tau_{\text{ph}}}\right] a_0 = -j\sqrt{\frac{1}{\tau_c}}\sqrt{P_i}
\end{aligned}
\tag{2.65}
$$

Solving for the complex amplitude a_0:

$$
a_0 = \frac{-j\sqrt{\frac{1}{\tau_c}}\sqrt{P_i}}{j(\omega_L - \omega_0) + \frac{1}{2\tau_{\text{ph}}}} = \frac{-j\sqrt{\frac{1}{\tau_c}}\sqrt{P_i}}{j\Delta\omega + \frac{1}{2\tau_{\text{ph}}}} \tag{2.66}
$$

It is conventional to express this in terms of the detuning $\Delta\omega = \omega_L - \omega_0$, thus the resonator amplitude can be written as:

$$
a(t) = \frac{-j\sqrt{\frac{1}{\tau_c}}\sqrt{P_i}}{j\Delta\omega + \frac{1}{2\tau_{\text{ph}}}} e^{j\omega_L t} \tag{2.67}
$$

It follows from (2.61) that the through port wave is then:

$$
\begin{aligned}
& s_t(t) = \sqrt{P_i}\exp(j\omega_L t) - j\sqrt{\frac{1}{\tau_c}}\left(\frac{-j\sqrt{\frac{1}{\tau_c}}\sqrt{P_i}}{j\Delta\omega + \frac{1}{2\tau_{\text{ph}}}} e^{j\omega_L t}\right) \\
\Leftrightarrow\ & s_t(t) = \sqrt{P_i}\exp(j\omega_L t)\left(1 - \frac{\frac{1}{\tau_c}}{j\Delta\omega + \frac{1}{2\tau_{\text{ph}}}}\right) \\
\Leftrightarrow\ & s_t(t) = s_i(t)\left(\frac{j\Delta\omega + \frac{1}{2\tau_{\text{ph}}} - \frac{1}{\tau_c}}{j\Delta\omega + \frac{1}{2\tau_{\text{ph}}}}\right)
\end{aligned}
\tag{2.68}
$$

Substituting the photon lifetime with (2.39) — for an all-pass microring — the end result is the steady-state field transmission transfer function of the CMT formulation (2.69) also adapted from [11].

$$
T(\Delta\omega) = \frac{s_t}{s_i} = \frac{j\Delta\omega + \frac{1}{2\tau_{\text{i}}} - \frac{1}{2\tau_{\text{c}}}}{j\Delta\omega + \frac{1}{2\tau_{\text{i}}} + \frac{1}{2\tau_{\text{c}}}} \tag{2.69}
$$

This provides the spectral response directly from the intrinsic and coupler photon lifetimes, which can be related through the coupling ratio CR defined by [11] as

$$
\text{CR} = \frac{\tau_i}{\tau_c} = \frac{Q_i}{Q_c} \tag{2.70}
$$

In Figure 2.15 it can be seen that for the critical coupling ratio $CR = 1$ no power is transmitted to the through-port at resonance, which is a common goal when designing MRM's since this provides the largest extinction ratio (ER) meaning a larger eye-opening for PAM modulation. In

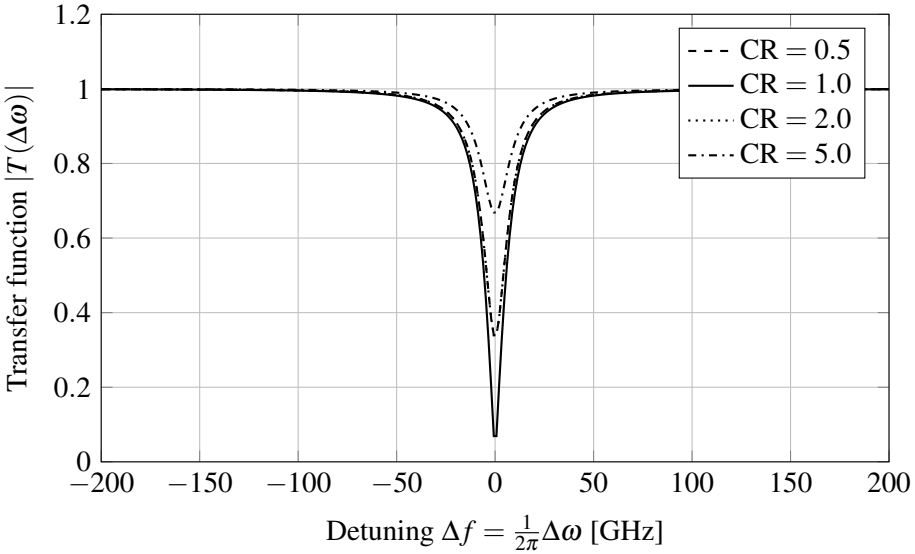


Figure 2.15: Transfer function amplitude $|T(\Delta\omega)|$ of a microring resonator as a function of detuning for different coupling ratios CR $= \tau_i/\tau_c$. The functions are computed using the CMT formulation with a quality factor of $Q = 10000$.

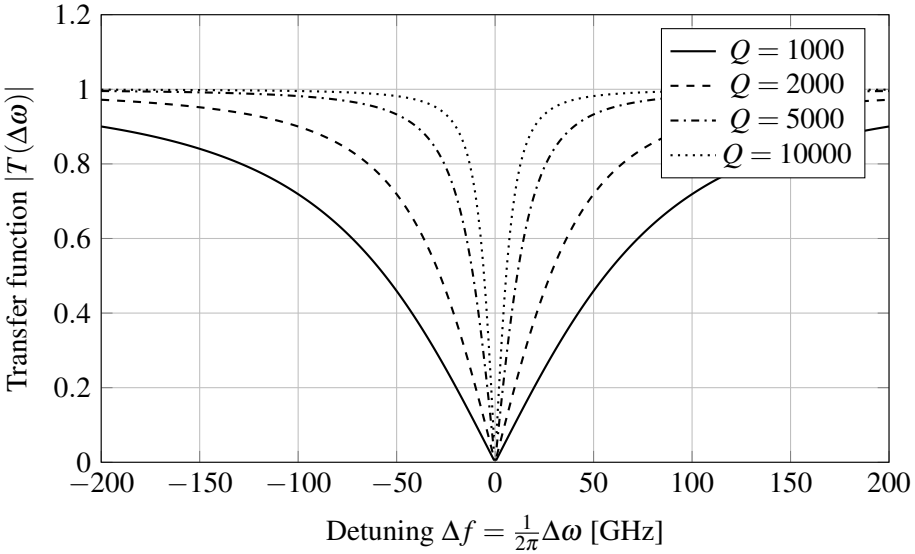


Figure 2.16: Transfer function amplitude $|T(\Delta\omega)|$ of a microring resonator as a function of detuning for different quality factors $Q = \omega_0\tau_{\text{ph}}$ at critical coupling (CR $= 1$).

Figure 2.16, the effect of the quality factor and photon lifetime on the bandwidth linewidth is observed [1, 11].

When designing the MRM, the matching of the quality factor of the coupler and of the intrinsic losses and coupler determines the filter depth as seen in Figure 2.15, and therefore a common goal is to design the MRM for CR = 1 obtained by making $Q_i = Q_c$ with help of Equation (2.44) [1].

2.5.6 Microring modulator Figures of Merit

This section is based on the design methodology for microring resonators described by Chrostowski and Hochberg [1, Ch. 6.3.3].

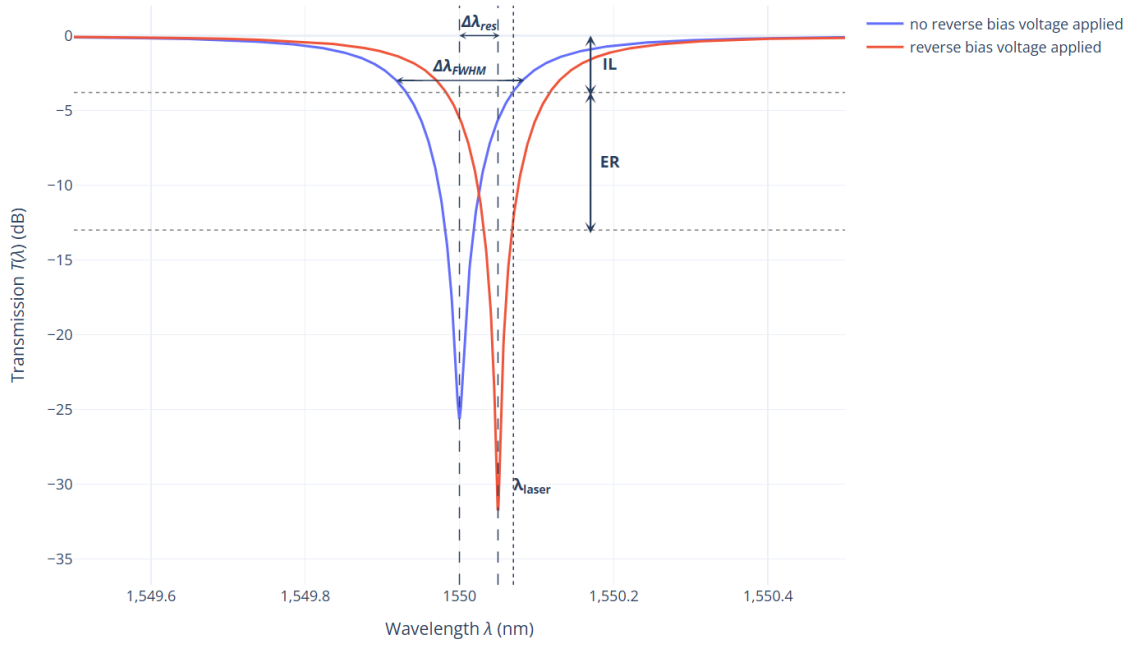


Figure 2.17: Transmission of MRM at different voltages adapted from [8].

Following [8], the performance of optical modulators can be characterised by several key metrics:

- **Extinction Ratio (ER)**: Ratio between the optical power of the high and low states at the laser wavelength, ER $= \frac{P_1}{P_0}$, generally expressed in decibels.
- **Optical Modulation Amplitude (OMA)**: Difference between two modulation levels $\text{OMA}_{01} = P_1 - P_0$. Utilized to characterize modulation schemes with multiple levels like PAM4.
- **Insertion Loss (IL)**: Power loss between the input and through ports in the on state.
- **Bandwidth**: The maximum modulation frequency supported by the device, which is related to the resonance linewidth $\Delta\lambda_{\text{FWHM}}$ through Eq. 2.53.
- **Voltage & Energy-per-Bit**: Determined by the refractive index modulation swing required by the pn-junction phase shifter, which directly affects the resonance shift $\Delta\lambda_{\text{res}}(V)$.

Figure 2.17 illustrates these key metrics in the transmission spectrum of a microring modulator. The resonance shift $\Delta\lambda_{\text{res}}$ represents the change in the resonance wavelength with the applied modulation voltage, while the resonance linewidth $\Delta\lambda_{\text{FWHM}}$ characterizes the spectral width of the resonance. The ER and IL quantify the modulation depth and optical loss, respectively, at the lasing wavelength λ_{laser}. To achieve a large ER with small loss IL the ratio between the resonance shift and linewidth should be designed to be sufficiently large $\frac{\Delta\lambda_{\text{res}}}{\Delta\lambda_{\text{FWHM}}}$.

Balanced Resonator Note that the resonance depth, i.e., transmission $T(\lambda)$ at resonance wavelength, changes with the modulation voltage. This variation results from a change in the balance (coupling ratio) between the intrinsic Q_i and coupling Q_c quality factors. In Fig. 2.17 the coupling quality factor is fixed at $Q_c = 20000$, while the intrinsic quality factor increases from $Q_i = 18000$ to $Q_i = 19000$ with the increasing reverse-bias modulation voltage. Consequently, the resonator approaches the critical-coupling condition, resulting in a higher resonance depth.

(2.70) is not constant, the waveguide loss α in the ring decreases when the depletion region increases in size due to the existence of less carriers, see plasma dispersion in Sec. 2.1. This makes τ_i, and equivalently Q_i, increase due to Eq. (2.37)

The change in Q_i and Q_c happens because τ_c changes with the group index (2.38) and τ_i changes with the group index n_g and waveguide loss α (2.37). As explained by the formalism in Sec. 2.1 the loss α decreases with a larger depletion region in a p–n junction — high reverse-bias voltage —and that's why in the example figure Q_i increases when modulated.

Bandwidth and Modulation Limits The total cutoff frequency is given by cascading the cutoff frequency of the pn-junction phase shifter (2.24) and of the microring resonator (2.52) as described by Chrostowski and Hochberg [1]

$$\frac{1}{f_c^2} = \frac{1}{f_{\tau_{ph}}^2} + \frac{1}{f_{\tau_j}^2} \tag{2.71}$$

The 3-dB cutoff frequency is an important design metric since it limits the maximum symbol rate, and is defined as the frequency at which the transmitted power drops to half. Frequencies beyond f_c contribute less to the channel response, meaning the channel is band-limited by f_c.

Resonance Shift: The achievable resonance shift, $\Delta\lambda_{\text{res}}$, determines how far the device's resonance can be tuned away from the laser wavelength λ_{laser}. This tunability is essential for performance: shifting the resonance away reduces insertion loss at the ON state, while returning it to the lasing frequency increases the extinction ratio (ER) toward the maximum value set by the resonance depth (see Fig. 2.17). To quantify this shift, we derive how the resonance wavelength depends on the applied voltage.

To compute the resonance shift we differentiate the resonance condition (2.45) with respect to voltage

$$m\frac{d\lambda}{dV} = L\frac{d}{dV}\left[n_{\text{eff}}(\lambda, V)\right] = L\left(\frac{\partial n_{\text{eff}}}{\partial V} + \frac{\partial n_{\text{eff}}}{\partial \lambda}\frac{d\lambda}{dV}\right)$$

$$\frac{d\lambda}{dV}\left(m - L\frac{\partial n_{\text{eff}}}{\partial \lambda}\right) = L\frac{\partial n_{\text{eff}}}{\partial V}$$

Substituting $m = \frac{Ln_{\text{eff}}}{\lambda_0}$ (where λ_0 is the resonance wavelength) and then introducing the group index at λ_0 from Eq. (2.10) yields

$$m - L\frac{\partial n_{\text{eff}}}{\partial \lambda} = \frac{L}{\lambda_0}\left(n_{\text{eff}} - \lambda_0\frac{\partial n_{\text{eff}}}{\partial \lambda}\right) = \frac{Ln_g}{\lambda_0}$$

This results in the resonance shift per voltage as a function of the effective index shift per voltage, a figure of merit of the pn-junction discussed in 2.3

$$\frac{d\lambda}{dV} = \frac{\lambda_0}{n_g}\frac{\partial n_{\text{eff}}}{\partial V} \tag{2.72}$$

From this the total shift is given by

$$\Delta\lambda_{\text{res}} = \frac{\lambda_0}{n_g}\Delta n_{\text{eff}}(V) \tag{2.73}$$

where $\Delta n_{\text{eff}}(V)$ is the achieved effective index shift for a reverse bias voltage of V.

2.6 Summary

The chapter established the theoretical foundations for the design and analysis of silicon photonic microring modulators. The carrier-depletion PN junction functions as the phase-shifting element which modulates the effective refractive index through its core performance metrics that consist of modulation efficiency, effective index shift, electrical bandwidth and energy consumption.

The operation of microring resonator modulators became clear through their resonance condition and transmission characteristics and quality factors and coupled-mode theory. The main device performance parameters which consist of the resonance shift, extinction ratio, insertion loss and the 3dB bandwidth, obtained from the frequency linewidth. All this parameters become available through an integrated analysis considering the PN junction properties.

These theoretical concepts serve as the foundation which supports both simulation techniques and design optimisation methods that the upcoming chapters explore.

Chapter 3

Simulation Methodology

3.1 Introduction

The simulation workflow presented in this chapter is based on and adapted from several Ansys Lumerical application examples. In particular, the overall microring modulator workflow is based on the *Ring Modulator* tutorial [12]; the PAM4 electrical drive is based on the *Optical PAM4 Transceiver* tutorial [13], and the analysis of the PN-depletion phase shifter is based on the *PN-depletion Phase Shifter* tutorial [14]. These examples serve as the foundation for the simulation methodology developed and implemented in this work.

The design and evaluation of a microring modulator is done by the following hierarchical multi-physics simulation flow:

1. Extraction of the charge carrier distribution as a function of applied reverse bias voltage using drift-diffusion simulation (Ansys Lumerical CHARGE™). [15]

2. Characterisation of the waveguide sections —using the eigenmode solver (Ansys Lumerical MODE™). [16]

3. Characterisation of the directional coupler using 3D Finite-Difference Time-Domain (FDTD) simulation (Ansys Lumerical FDTD™). [17]

4. Characterisation of the active bent waveguide section and assembly of the complete ring modulator circuit, including PAM4 operating-point analysis, in the circuit simulator (Ansys Lumerical INTERCONNECT™). [18]

The device geometry is parameterised through Python dataclasses and the workflow is orchestrated through Python automation tools described in section 3.2. The overall architecture of the workflow is illustrated in Figure 3.1.

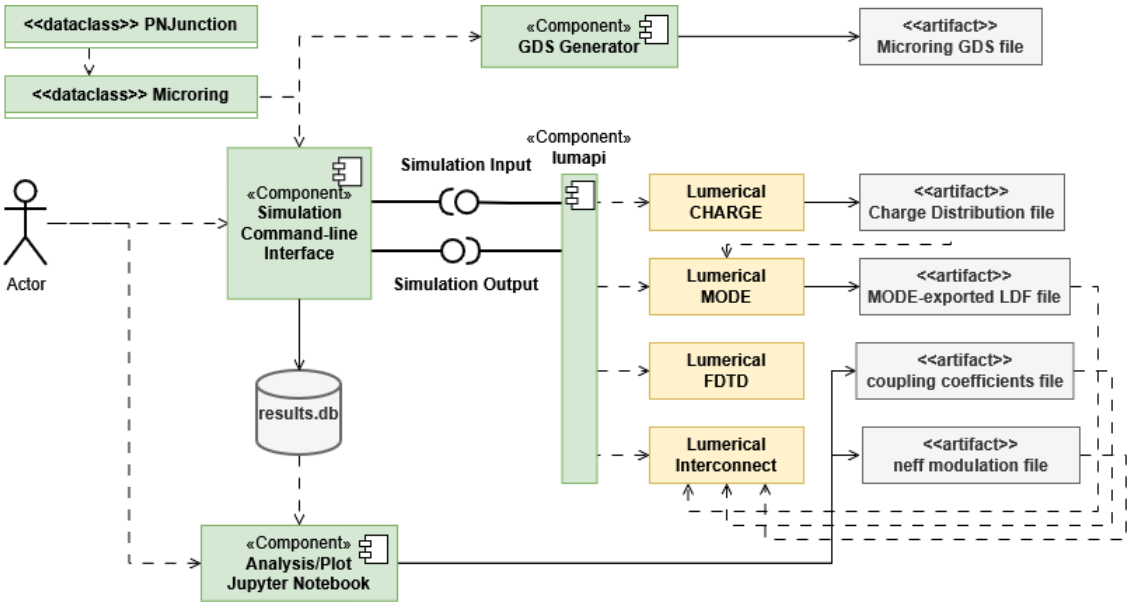


Figure 3.1: Component diagram of the simulation workflow.

3.2 Python Automation Layer

The Python automation layer is built on top of the `lumapi` interface and is responsible for the simulation workflow through a CLI. It can tweak simulation parameters or construct and generate CHARGE, MODE, FDTD and INTERCONNET simulations based on user input.

The user input consists of PN junctions and microring devices defined through the dataclasses and simulation sweeps selected through the CLI. After completing the simulations the automation layer stores resulting data in a database.

The device input parameters are illustrated in the class diagram shown in Fig. 3.2.

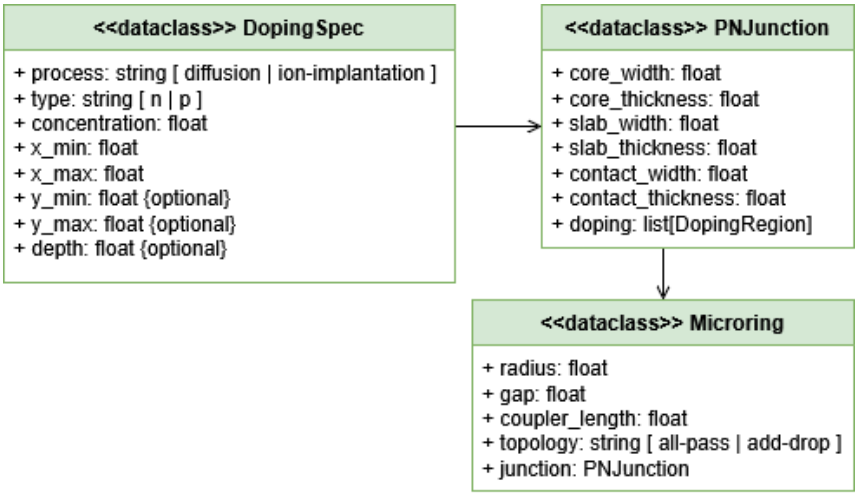


Figure 3.2: Class diagram of the simulation workflow.

3.3 Database Schema

The simulation results and device definitions are stored in an SQLite database, by default a `results.db` file. The database stores device definitions in JSON-encoded records, while each simulation record must reference the corresponding device in which the simulation was performed.

The database schema table overview is provided in Table 3.1.

Table	**Purpose**
`pn_junctions`	Device definitions
`microring_modulators`	Device definitions
`mode_frequency_sweep_simulations`	MODE frequency sweep results
`mode_voltage_sweep_simulations`	MODE voltage sweep results
`fdtd_coupling_simulations`	FDTD coupling results

Table 3.1: Database tables used in the simulation workflow.

Column	**Type**	**Description**
`id`	INTEGER	Primary key.
`data`	TEXT	JSON-encoded representation of the PN junction dataclass.

Table 3.2: Schema of the `pn_junctions` table.

Column	**Type**	**Description**
`id`	INTEGER	Primary key.
`data`	TEXT	JSON-encoded representation of the Microring modulator dataclass.

Table 3.3: Schema of the `microring_modulators` table.

Column	Type	Description
pn_junction_id	INTEGER	Foreign key referencing a PN-Junction definition
radius	REAL	Ring radius used in the simulation; NULL for straight waveguides.
frequency	REAL	Optical frequency point.
active	INTEGER	Indicates whether the waveguide section is doped.
neff_real	REAL	Real part of the effective index.
neff_imag	REAL	Imaginary part of the effective index.
vg	REAL	Group velocity.

Table 3.4: Schema of the mode_frequency_sweep_simulations table.

Column	Type	Description
pn_junction_id	INTEGER	Foreign key referencing a PN-Junction definition
radius	REAL	Ring radius used in the simulation; NULL for straight waveguides.
voltage	REAL	Applied reverse-bias voltage.
neff_real	REAL	Real part of the effective index.
neff_imag	REAL	Imaginary part of the effective index.

Table 3.5: Schema of the mode_voltage_sweep_simulations table.

Column	Type	Description
pn_junction_id	INTEGER	Foreign key referencing the PN-junction device definition used for the simulation.
voltage	REAL	Reverse-bias voltage applied to the PN junction.
frequency	REAL	Frequency of the AC excitation signal.
Y_real	REAL	Real part of the simulated junction admittance.
Y_imag	REAL	Imaginary part of the simulated junction admittance.

Table 3.6: Schema of the pn_junction_ac_characterisation table.

Column	Type	Description
pn_junction_id	INTEGER	Foreign key referencing a PN-Junction definition
radius	REAL	Ring radius used in the simulation.
gap	REAL	Coupling gap between the ring and bus waveguides.
frequency	REAL	Optical frequency point.
power_coupling	REAL	Coupled optical power.

Table 3.7: Schema of the fdtd_coupling_simulations table.

3.4 PN-Junction Characterisation (CHARGE)

The p–n junction was electrically characterised using the Ansys Lumerical CHARGE™ solver [15]. The simulation inputs consist of the waveguide geometry and doping distribution defined by the p–n junction dataclass illustrated in Fig. 3.2. The simulation setup is shown in Fig. 3.3

The CHARGE simulation produces the following outputs:

- **DC simulation:** A **charge distribution file** (`charge_distribution.mat`), illustrated in Fig. 3.1, containing the spatial carrier distribution as a function of bias voltage.
- **Small-signal AC simulation:** Outputs the small-signal voltage and current responses, δV and δI, utilized to compute the admittance with Eq. 3.1. The results are stored in the `pn_junction_ac_characterisation` database table described in Table 3.6.

$$Y(f, V_{DC}) = \frac{\delta I(f, V_{DC})}{\delta V(f, V_{DC})} \tag{3.1}$$



Figure 3.3: CHARGE simulation setup for PN-Junction

The doping distribution provided as input through the `DopingSpec` dataclass illustrated in Fig. 3.2 is an important design parameter since with it the Python Automation tool can insert two types of available doping processes in the CHARGE simulation tool — diffusion and ion-implantation —controlling the depletion region format.

3.5 Rib Waveguide Characterisation (MODE)

The rib waveguide was characterised using the FDE solver Ansys Lumerical MODE™[16]. This workflow stage objective is to determine the optical properties of undoped and doped waveguide cross-sections at different bend radii, including the straight waveguide case.

The simulation inputs are likewise derived from the device parameters defined by p–n junction dataclass illustrated in Fig. 3.2. However, unlike the CHARGE simulation, the MODE simulation does not directly use the doping parameters, it instead imports the carrier distribution for the doped-waveguide characterisation from the `charge_distribution.mat` file described in Section 3.4.

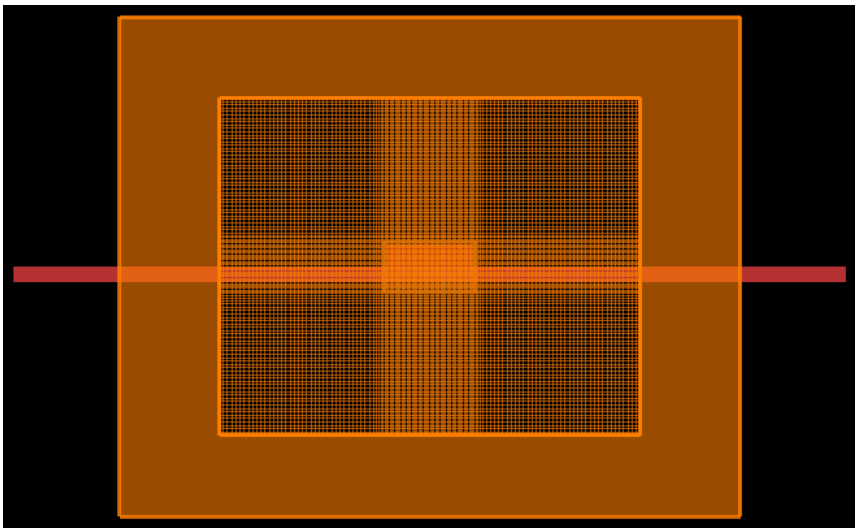


Figure 3.4: MODE simulation setup

3.5.1 Undoped Waveguide Characterisation

The undoped waveguide is mainly characterised through a frequency sweep, in which solving the eigenvalue problem for the setup illustrated in Fig. 3.4 yields the fundamental TE mode $e(x,y,f)$ and corresponding effective index $n_{\text{eff}}(f)$ over the optical frequency range of interest.

The group index (f) is subsequently obtained from $n_{\text{eff}}(f)$ through Eq. 2.10. Alternatively the group velocity v_g, related to by Eq. 2.9, is utilized since Lumerical MODE simulation outputs it directly.

Lumerical MODE simulation results expose the group velocity, related to by Eq. 2.9.

The frequency sweep then can be repeated for different waveguide geometries and microring radii. The resulting modal properties are stored in the `mode_frequency_sweep_simulations` database table, as described in Table 3.4.

Lumerical Data Files: The optical properties obtained from frequency sweeps are exported as Lumerical Data Files (`.ldf`). These files can be imported in INTERCONNECT to define straight, bent and active bent waveguide blocks.

3.5.2 Doped Waveguide Characterisation

The doped waveguide is mainly characterised through a voltage sweep of the bias voltages and corresponding carrier distributions. For each applied reverse-bias voltage the eigenvalue problem is solved yielding the fundamental TE mode $e(x,y,V)$ and the corresponding effective index $n_{\text{eff}}(V)$.

The resulting modal properties are stored in the `mode_voltage_sweep_simulations` database table, as described in Table 3.5. Similarly to the frequency sweep 3.5.1 the table accounts for variations in the waveguide geometry and microring radii.

Effective-index modulation file: To simulate the effective index modulation in INTERCONNECT the voltage-dependent index change $\Delta n_{\text{eff}}(V)$, obtained through Eq. 3.2, needs to be imported into an optical modulator as a text-based data file with the following columns: applied voltage V, real component of the effective index $\Re\{n_{\text{eff}}\}$ and imaginary component of the effective index $\Im\{n_{\text{eff}}\}$.

$$\Delta n_{\text{eff}}(V) = n_{\text{eff}}(V) - n_{\text{eff}}(0) \tag{3.2}$$

This file is generated from the data gathered in the database as Illustrated in Fig 3.1.

3.6 Coupler Characterisation (FDTD)

The directional coupler is characterised using the 3D FDTD solver Ansys Lumerical FDTD™ [17]. The simulation is constructed through the Python automation layer based on the main microring geometric parameters, radius and gap, as Illustrated in Fig 3.5.

The objective of the simulation is to characterise the coupling behaviour of the directional coupler by extracting the corresponding power coupling coefficient.

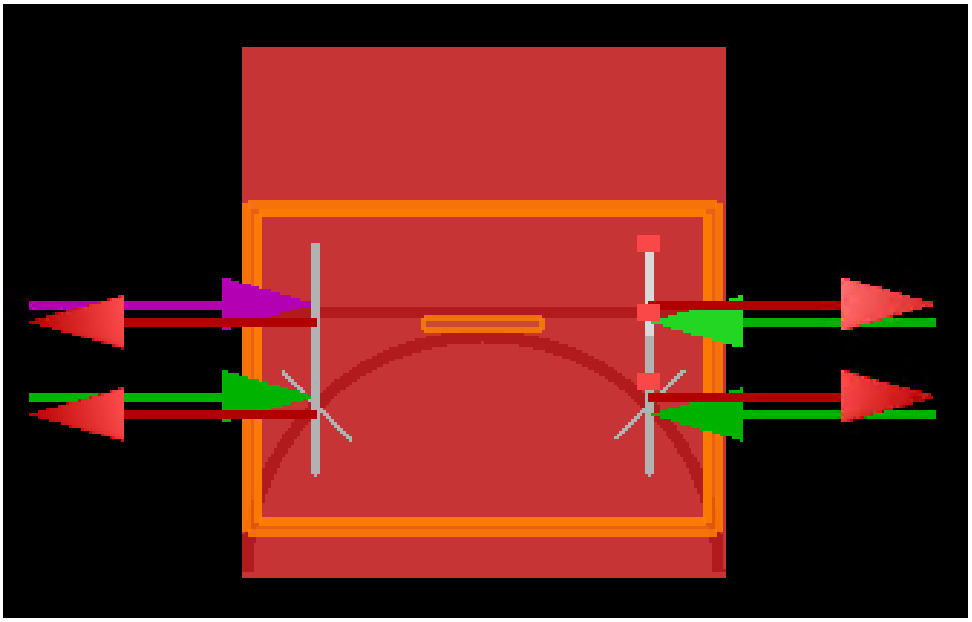


Figure 3.5: FDTD simulation setup for coupler characterisation.

The simulation contains four ports: an input port (1) and an output port (2) located on the bus waveguide, and left (3) and right (4) ports located on the ring. The ring ports are positioned at 45° on either side of the coupling region in order to sample the guided mode on the ring arc away from the local field perturbation introduced by the coupler. Only half of the microring is included in the simulation region, so the two ring ports together represent the propagation along the modeled half-ring section.

The coupling coefficient is extracted from the complex S-parameters returned by the port monitor after the simulation is run.

The input port (1) is set as the excitation source, and the complex S-parameters are then extracted from the port monitors after the simulation is complete.

The corresponding power coupling κ and through t coefficients are obtained from Eq. 3.3.

$$\kappa^2 = |S_{41}|^2, \qquad t^2 = |S_{21}|^2 \tag{3.3}$$

κ^2 represents the fraction of optical power coupled into the monitored ring port and t^2 the optical power transmitted through the bus waveguide, not coupling in the ring. For a lossless coupler these coefficients must satisfy

$$\kappa^2 + t^2 \approx 1.$$

The extracted power coupling data is stored in the `fdtd_coupling_simulations` database table, as described in Table 3.7. Each record is associated to a corresponding waveguide geometry and contains the power coupling as a function of frequency, radius and coupling gap: $\kappa^2(f, R, g)$.

Coupling coefficient file: A text-based coupling coefficient file needs to be imported in INTERCONNECT to simulate the coupler as a block. The file consists of two columns corresponding to the optical frequency f and the power coupling coefficient κ^2 at the equivalent frequency, throughout the frequency range of interest.

This file is generated from the data gathered in the database as Illustrated in Fig 3.1.

3.7 Circuit Assembly and Analysis (INTERCONNECT)

The circuit-level simulation of the microring modulator is performed in Ansys Lumerical INTERCONNECT™[18].

3.7.1 Microring Modulator Compound Element

The circuit under study is organized into a compound element `MRM`, which implements the microring modulator block used throughout the analysis, allowing it to be characterised in both the frequency and time domains.

The `MRM` block can be an all-pass or add-drop modulator as illustrated in Fig. 3.6, exposing the input, output and modulation ports and additionally the add and drop ports for the add-drop topology.

The inner structure of the `MRM_ALL_PASS` is Illustrated in Fig. 3.7

The microring modulator model shown in Fig. 3.7 requires the optical characteristics obtained from the preceding CHARGE, MODE, and FDTD simulations as inputs for the following blocks:

- **MODE:** Lumerical data files containing te frequency-dependent optical properties of the waveguide cross-sections.

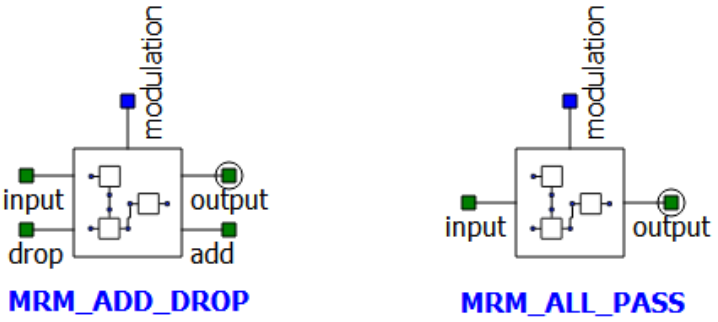


Figure 3.6: Microring Modulator Compound INTERCONNECT Element

  - `STRAIGHT_WG`: Straight waveguide section.
  - `PASSIVE_BEND_WG`: Passive bent waveguide section.
  - `ACTIVE_BEND_WG`: Active bent waveguide section biased at $V = 0$.

- **MODE:** Effective index modulation file containing voltage-dependent changes ($\Delta n_{\text{eff}}(V)$) to the effective index
  - `OM`: Optical modulator
- **FDTD:** Coupling coefficient file containing frequency-dependent power coupling characteristics.
  - `COUPLER`: Microring directional coupler.

The microring compound element also requires as input the following geometry parameters that can be tweaked in the design chapter:

- radius (R): Defines the length of the ring and consequently the resonance, and the length definition is necessary since the waveguide data files only provide the cross-section optical response.
- coupler length (L_c): Also defines the length of the ring, the coupler length is not accounted by the `COUPLER` block since the former only accounts for coupling, so L_c as a parameter is necessary to define the passive waveguide sizes.
- Active region fraciton (χ): Defines the percentage of the full length $L_{\text{rt}} = 2\pi R + 2L_c$ that `ACTIVE_BEND_WG` consists of on the ring.

3.7.2 Frequency-Domain Analysis

Figure 3.8 shows the frequency-domain analysis setup used to characterize the MRM. In this configuration, a direct current (DC) source (`DC_1`) is connected to the modulation port to provide

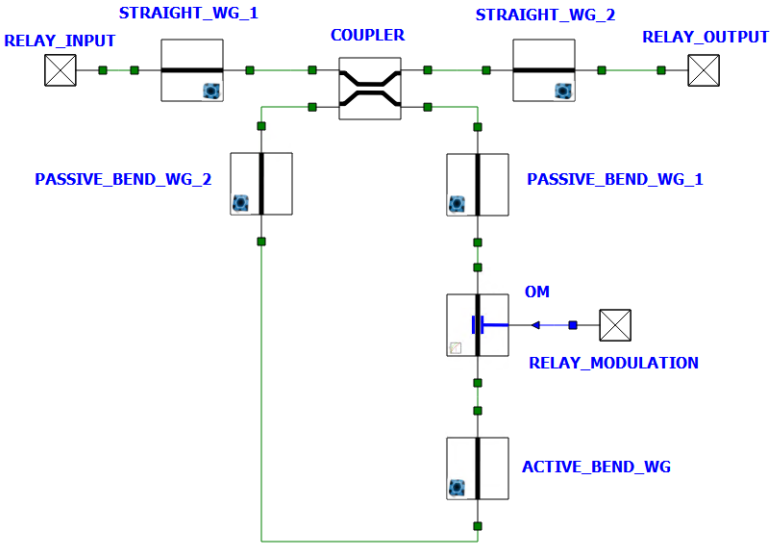


Figure 3.7: Microring Modulator Block Diagram

the required bias voltage. An optical network analyzer (ONA_1) is connected to the optical input and output ports in order to extract the frequency response of the device.

The ONA performs a frequency sweep over the optical frequency range of interest and extracts the following quantities:

- **S-parameters:** Complex scattering parameters, particularly S_{21}, characterising the device transmission response.
- **Resonance characteristics:** Resonance frequencies and corresponding transmission minima.
- **Free spectral range (FSR):** Frequency spacing between adjacent resonances.
- **Extinction ratio:** Ratio of the maximum to minimum transmission.
- **Quality factor:** Ratio of the resonance frequency to its linewidth, enabling determination of the optical 3-dB bandwidth.

3.7.3 Time-Domain Analysis

The time-domain analysis setup is shown in Figure 3.9. This configuration is used to evaluate the transient behavior of the MRM.

Optical Transmitter: A continuous-wave laser (`CWL_1`) provides the optical carrier at the input port.

Optical Receiver: The optical output is monitored by an optical oscilloscope (`OOSC_1`) prior to detection. The receiver chain consists of an attenuator (`ATT_1`), a photodetector (`PIN_1`), and

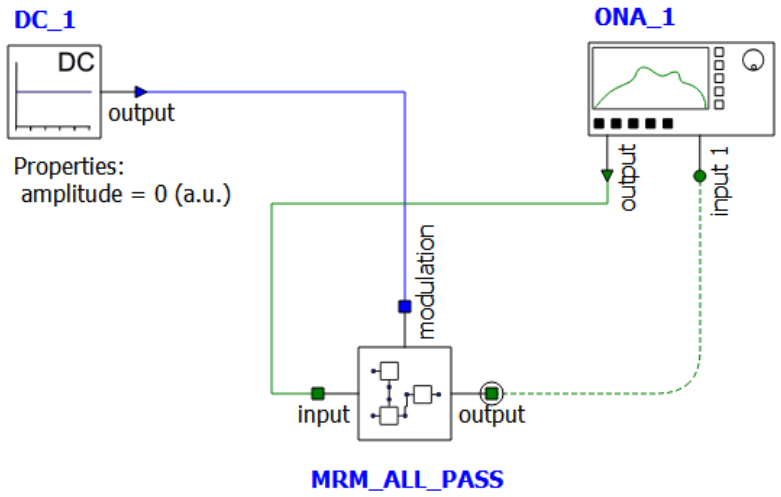


Figure 3.8: Microring modulator frequency domain analysis setup, with DC Source and Optical Network Analyzer (ONA)

a low-pass filter (`LPF`). The resulting electrical output is then connected to both an oscilloscope (`OSC_2`) and an eye-diagram monitor (`EYE_1`) for temporal performance evaluation.

Electrical Drive: This chain consists of a pseudo-random binary sequence (`PRBS`) generator that feeds a modulation pulse amplitude mapper (`MAP`), which generates a PAM4 waveform that is applied to the modulation port. An oscilloscope monitor is connected at the modulation output to observe the applied signal.

Since the optical modulator block `OM` inside the microring compound element is ideal and not bandwidth limited, the only bandwidth-limiting element in this setup is provided is the `MAP_1` driver, as a normalized rise time parameter.

$$\frac{t_\mathrm{r}}{t_s}$$

where t_r is the rise time and t_s the symbol time obtained from the bitrate f_s of the simulation.

$$t_s = \frac{1}{f_s}$$

In physical systems thee 10–90% rise time is approximately related to the 3-dB bandwidth by

$$f_{3\mathrm{dB}} \approx \frac{0.35}{t_\mathrm{r}} \tag{3.4}$$

so a good approximation for the percentual rise time parameter utilized in the design is

$$\frac{t_\mathrm{r}}{t_s} \approx 0.35 \cdot \frac{f_s}{f_{3\mathrm{dB}}} \tag{3.5}$$

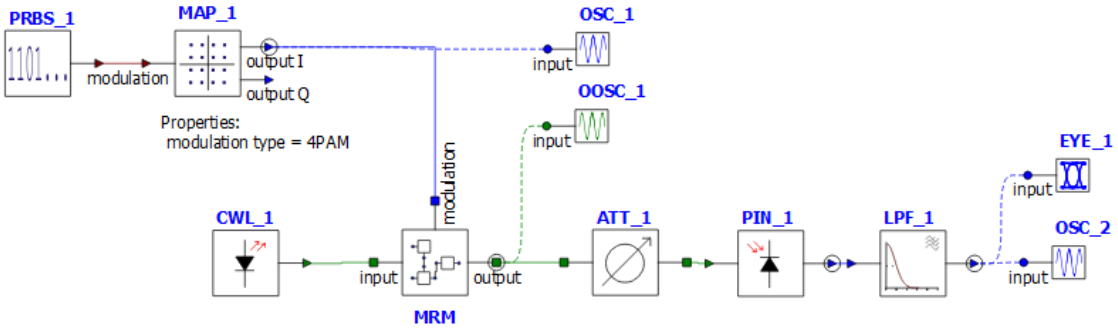


Figure 3.9: Microring modulator time domain analysis setup, with PAM driver, transmitter and receiver chains

3.8 Summary

This chapter presented the multi-physics simulation methodology developed for the microring modulator design and analysis. The workflow developed integrates the electrical, optical, and circuit-level simulations through a hierarchical approach, combining CHARGE, MODE, FDTD, and INTERCONNECT simulations to capture the device characteristics.

A Python automation layer was developed to provide a unified framework for the generation of parameterised devices, running simulations, and managing the simulation data through an SQLite database.

The extracted waveguide modal properties, coupler characteristics, and voltage induce modulation properties form the basis of the circuit-level microring modulator model. The assembled INTERCONNECT model allows the evaluation of both static optical properties and dynamic PAM4 transmission performance.

The methodology established in this chapter therefore provides the foundation for the subsequent design optimisation and performance analysis of the microring modulator.

Chapter 4

Device Design and Target Specifications

4.1 Introduction and Design Objectives

This chapter describes the design process adopted for the microring modulator. Using the theoretical framework introduced in Chapter 2, the objective is to identify a device geometry that satisfies the bandwidth and extinction ratio requirements while minimizing optical loss, footprint, and power consumption.

Design Objectives: The microring modulator design must satisfy several competing requirements:

- Resonant operation at a specified design wavelength λ_0 within the C-band (e.g., 1550 nm)
- High optical bandwidth BW [GHz]
- High extinction ratio ER [dB]
- Low insertion loss IL [dB]
- Reduced power consumption E_{bit} [pJ/bit]

The design variables considered in this work are represented in the microring dataclass (Fig. 3.2), which contains the p–n junction with its own efficiency requirements:

- Resonance wavelength shift as a function of voltage $\Delta\lambda(V)$ [pm]
- High effective index modulation efficiency $\frac{dn_{\text{eff}}}{dV}$ [V^{-1}] , or equivalently a small voltage length product $V_\pi \cdot L$ [$\text{V} \cdot \text{cm}$].
- Sufficient junction 3-db electrical bandwidth f_{τ_j} [GHz]

4.2 Fabrication Constraints and Candidate Waveguide Geometries

The microring modulator is implemented on a standard 220-nm SOI platform. In a foundry environment, the rib waveguide cross-section is typically fixed and cannot be freely optimized, as the etch depth, slab thickness, and rib width are tightly constrained by process design rules and yield considerations.

In this work, we adopt a generic rib waveguide geometry used in silicon photonic PDKs, following the generic process parameters reported in [1, Ch. 10] and shown in Tab. 4.1

Parameter	Target value
Silicon thickness	220 nm
Silicon etch	130 nm
Doping (N)	5×10^{17} cm^{-3}
Doping (P)	7×10^{17} cm^{-3}
Doping (N++)	5×10^{20} cm^{-3}
Doping (P++)	1.9×10^{20} cm^{-3}

Table 4.1: Generic silicon photonic PDK fabrication process parameters used as reference for the PN-junction design, adapted from [1, Ch. 10].

The slab and core thickness follow directly from the silicon thickness and etch values in Tab. 4.1. The core width is chosen to tune the optical loss and optical confinement as described in Sec. 2.2.1, the loss is too high for a core width of 0.45 µm, so the width of 0.5 µm is utilized, as illustrated in Fig. 4.1

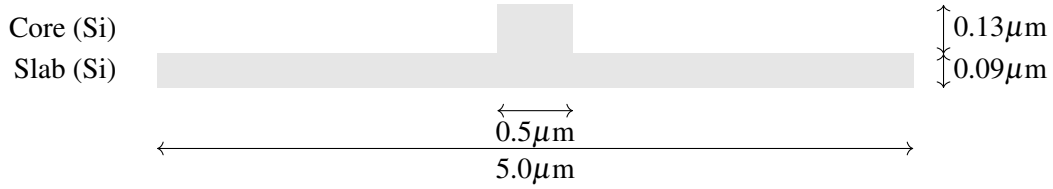


Figure 4.1: Rib waveguide cross-section

4.2.1 Analytical Design Criteria

4.2.1.1 Active modulation region

Ideally, the PN junction would extend over the entire ring circumference in order to maximize the interaction length and therefore the modulation efficiency. However, the coupling region between the microring and bus waveguide imposes a geometrical constraint as seen in Fig. 4.2.

- C_A: radial distance from the center of the microring to the center line of the bus-waveguide core.

$$C_A = R + w_{\text{wg}} + g \tag{4.1}$$

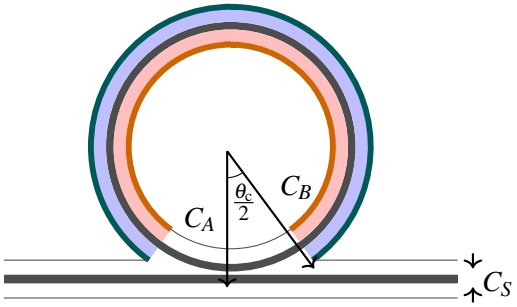


Figure 4.2: Geometrical definition of the clearance angle θ_c in the microring modulator.

- C_B: radial distance from the center of the microring to the outer boundary of the ring slab region.

$$C_B = R + \frac{w_{\text{slab}}}{2} \tag{4.2}$$

- C_S: required passive clearance distance between active region and bus-waveguide core.
- θ_c: clearance angle defining the angular portion of the ring that remains inactive around the bus-waveguide coupling region.

$$\theta_c = 2\cos^{-1}\left(\frac{C_A - C_S}{C_B}\right) \tag{4.3}$$

The active modulation fraction χ — percentage of the ring circumference that can be modulated —is then computed from the clearance angle with the Eq. 4.4.

$$\chi = 1 - \frac{\theta_c}{2\pi} = 1 - \frac{1}{\pi}\cos^{-1}\left(\frac{C_A - C_S}{C_B}\right), \qquad \chi \in [0,1] \tag{4.4}$$

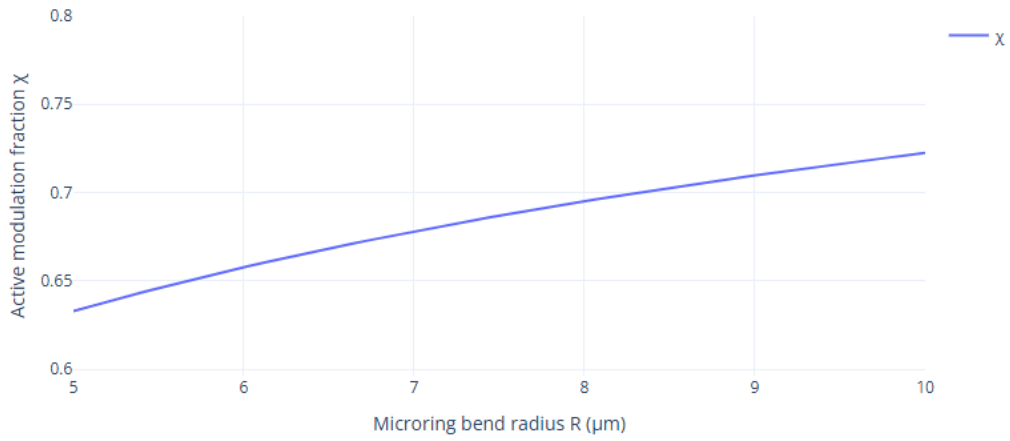


Figure 4.3: Active modulation fraction χ of an all-pass microring modulator as a function of microring bend radius R with $w_{\text{wg}} = 0.5\,\mu\text{m}$, $w_{\text{slab}} = 5.0\,\mu\text{m}$, $g = 0.4\,\mu\text{m}$ and $C_s = 2.5\,\mu\text{m}$.

The active fraction decreases for smaller radii due to the increased angular portion required for clearance between the microring junction and the bus waveguide coupling region as seen in Figure 4.3.

The resonance condition depends on the optical phase accumulated over one round-trip of the microring. Since the optical mode propagates through both active and passive sections, the effective index of the complete device is given by the length-weighted average effective index

$$\bar{n}_{\text{eff}} = \chi\, n_{\text{eff,active}} + (1-\chi)\, n_{\text{eff,passive}} \tag{4.5}$$

where $n_{\text{eff,active}}$ and $n_{\text{eff,passive}}$ denote the complex effective indices of the active and passive waveguide cross-sections, respectively.

The voltage-induced perturbation follows the same averaging principle,

$$\Delta\bar{n}_{\text{eff}} = \chi\, \Delta n_{\text{eff,active}} + (1-\chi)\, \Delta n_{\text{eff,passive}}$$

Since the passive clearance region is not modulated, $\Delta n_{\text{eff,passive}} = 0$

$$\Delta\bar{n}_{\text{eff}} = \chi\, \Delta n_{\text{eff,active}} \tag{4.6}$$

Parameters depending on the effective index n_{eff} and its voltage-induced perturbation Δn_{eff} slightly change due to the active fraction and must be accounted for in device design. Examples include the resonance wavelength (2.45), the achievable resonance shift (2.73), and the intrinsic quality factor (2.44).

4.2.2 Resonance-shift and insertion-loss criterion

By selecting a 3-dB threshold as the maximum acceptable insertion-loss, the design objectives set for the p–n junction in Sec. 4.1 can be directly related to the quality factor Q through Eq. (2.53), since a resonance shift which is equal to the linewidth $\Delta\lambda_{\text{res}} = \Delta\lambda_{\text{FWHM}}$ produces the 3-dB insertion-loss.

Substituting the linewidth in Eq. (2.53) with $\Delta\lambda(V)$ and a target resonance wavelength $\lambda_0 = 1550\,\text{nm}$ yields

$$Q_{\text{IL}=3dB}(V) = \frac{1550\,\text{nm}}{\Delta\lambda(V)} \tag{4.7}$$

Or equivalently in terms of the frequency linewidth

$$\Delta f_{\text{FWHM}}(V) = \frac{f_0}{Q} = \frac{c}{\lambda_0^2}\Delta\lambda(V), \qquad \frac{c}{\lambda_0^2} \approx 0.125\,\text{GHz/pm} \tag{4.8}$$

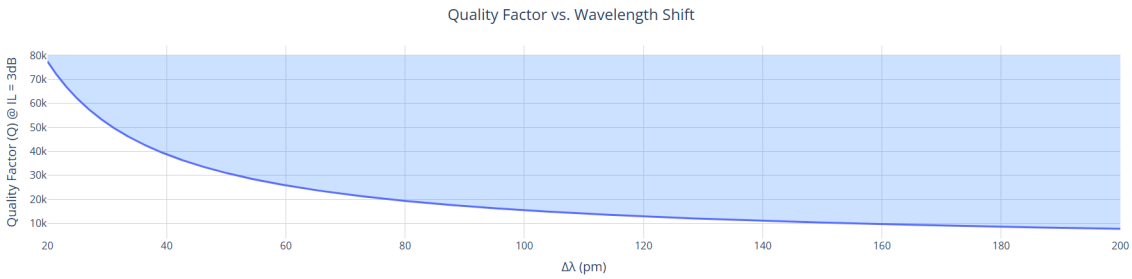


Figure 4.4: 3-dB insertion loss quality factor as a function of achievable resonance shift $\Delta\lambda_{\text{res}}$. The blue region represents Q values that lower the IL below the 3-dB value.

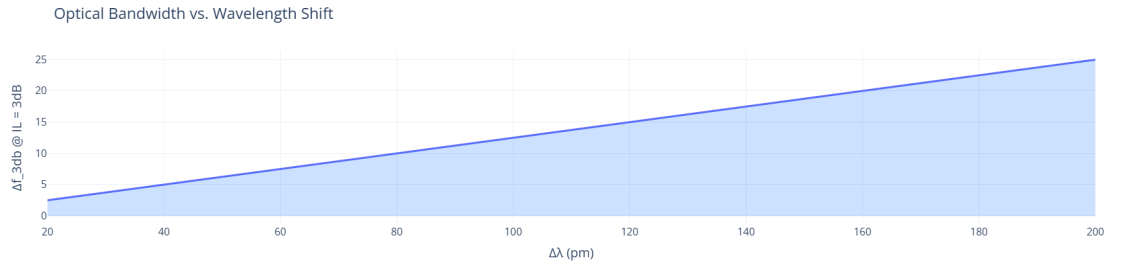


Figure 4.5: 3-dB insertion loss frequency linewidth as a function of achievable resonance shift $\Delta\lambda_{\text{res}}$. The blue region represents Δf_{FWHM} values that lower the IL below the 3-dB value.

Figures 4.4 and 4.5 illustrate the relationship between the resonance wavelength shift induced by the phase modulator, the quality factor, and the corresponding optical frequency linewidth. In both figures the blue curve represents the 3-dB insertion-loss boundary. The blue region represents values of Q or Δf_{FWHM} with lower insertion loss for the same value of $\Delta\lambda_{\mathrm{res}}$ at the detriment of higher Q and narrower resonance. This shows that a larger voltage induced resonance wavelength shift $\Delta\lambda(V)$ enables a larger optical bandwidth for a given insertion-loss requirement.

At a center wavelength of $\lambda_0 = 1550$nm, Fig. 4.5 confirms that the optical bandwidth increases at a rate of 0.125 GHz/pm.

4.2.3 Doping Profile and Junction Geometry

The overlap between the mode profile, illustrated in Fig. 2.2, and the p–n junction formed between the n and p doped regions directly affects the effective index modulation as seen in Eq. 2.15.

In the literature, many junction designs have been explored [19]. Among these, two common designs are the vertical depletion region [1], illustrated in Fig. 4.6, and a L-shaped depletion region [4, Ch. 6.2], illustrated in Fig. 4.7.

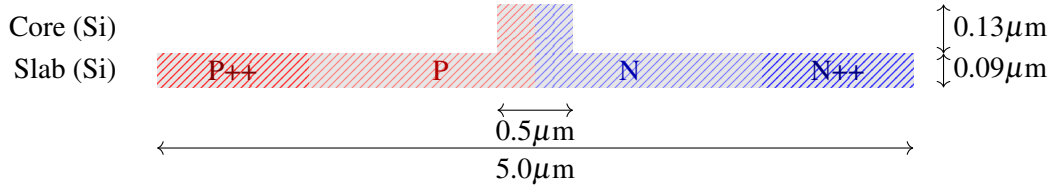


Figure 4.6: PN junction abrupt vertical junction cross-section

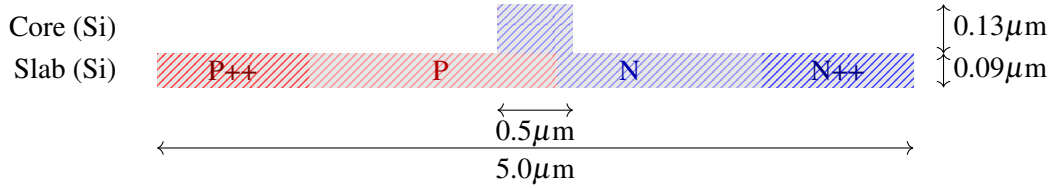


Figure 4.7: PN junction L-shaped junction cross-section

The doping strategy used to realize these profiles is illustrated in Figs. 4.8 and 4.9. The vertical junction has p and n ion implants with the same range while to achieve a L-shaped junction a shallow implant, with less range, is required [19].

The ligth and heavy doping concentrations shown in Table 4.1 are utilized for the ion-implantation and diffusion doping respectively.

The doping parameters utilized to generate the discussed junction types are summarized in Table 4.2 which uses as reference the coordinate axis and origin illustrated in Fig. 4.10.

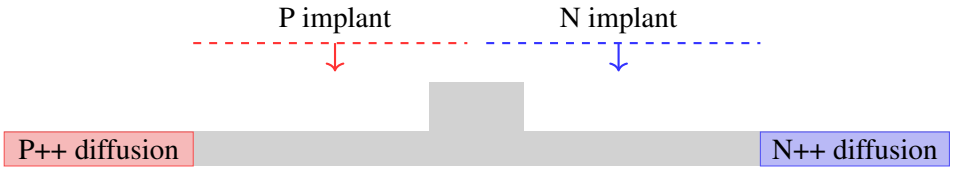


Figure 4.8: Implant Doping for abrupt vertical junction

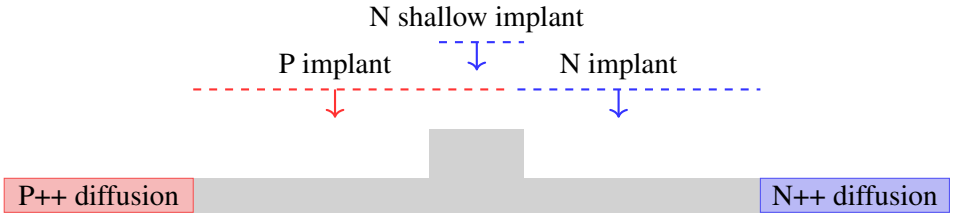


Figure 4.9: Implant Doping for L-shaped junction

Junction	**Region**	**Type**	**Concentration** (cm^{-3})	**Lateral extent** (µm)	**Depth / Vertical extent** (µm)
Vertical	N++ well	n	5×10^{20}	$x = [-2.75, -1.0]$	$y = [-1.0, 0]$
	P++ well	p	1.9×10^{20}	$x = [1.0, 2.75]$	$y = [-1.0, 0]$
	N implant	n	5×10^{17}	$x = [-1.0, 0]$	$d = 0.15$
	P implant	p	7×10^{17}	$x = [0, 1.0]$	$d = 0.15$
L-shaped	N++ well	n	5×10^{20}	$x = [-2.75, -1.0]$	$y = [-1.0, 0]$
	P++ well	p	1.9×10^{20}	$x = [1.0, 2.75]$	$y = [-1.0, 0]$
	N implant	n	5×10^{17}	$x = [-1.0, -0.25]$	$d = 0.15$
	P implant	p	7×10^{17}	$x = [-0.25, 1.0]$	$d = 0.15$
	Shallow N	n	7×10^{17}	$x = [-0.25, 0.25]$	$d = 0.05$

Table 4.2: Summary of the doping profiles used for the investigated PN junctions. The abrupt junctions (500 nm and 450 nm core widths) share the same doping configuration. Diffusion regions are defined by their lateral (x) and vertical (y) extents, while implanted regions are characterised by their lateral extent and implantation depth (d).

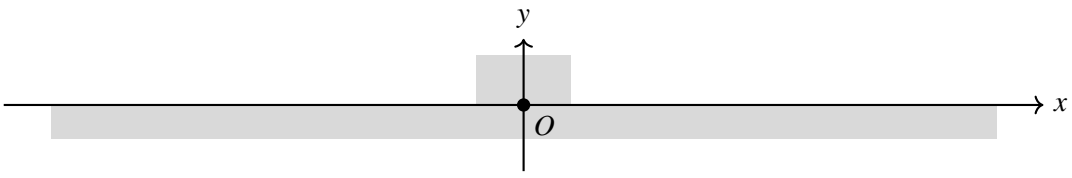


Figure 4.10: Cross-sectional schematic of the rib waveguide geometry with the coordinate origin located at the center of the core–slab interface.

4.3 Ring Radius selection procedure

The intrinsic quality factor is determined by Eqs. (2.44) and (2.37), being directly dependent on the loss α or equivalently the imaginary part of the effective index $\Im\{n_{\text{eff}}\}$ both computed in the MODE simulations.

A smaller ring radius or core width increases loss and therefore decreases the quality factor, whilst a larger radius or core width decreases loss and increases the quality factor. The MODE simulations therefore need to be realized near radius and core width values that satisfy a design target for the intrinsic quality factor Q_i.

Radius design for resonance: The radius cannot be selected solely from the intrinsic quality factor, since the ring geometry must also have a resonance at the design wavelength $\lambda_0 = 1550\,\text{nm}$ in accordance with the resonance condition (2.45).

The effective index obtained from the MODE simulations can be described as a function $n_{\text{eff}}(R,\lambda)$ obtained from the interpolation of the data for the effective index results. Both the active and passive sections must be considered in accordance with Eq. (4.5) yielding the interpolation function $\bar{n}_{\text{eff}}(R,\lambda)$ for $\chi = 0.65$.

The resonant radii were found by numerically solving $F_m(R) = 0$ (root-finding) where F_m is derived from (2.45).

$$F_m(R) = \frac{2\pi R \bar{n}_{\text{eff}}(R,\lambda_0)}{\lambda_0} - m \tag{4.9}$$

This process provides a list of radii with resonance at $\lambda_0 = 1550\,\text{nm}$ from which we can extract the interpolated intrinsic quality factor

4.4 Coupling-gap selection procedure

The coupling region geometry, ring radius and bus gap illustrated in Fig. 3.5, determines the strength of the interaction between the bus waveguide and the resonator. The FDTD simulation in Sec. 3.6 extracts the power coupling coefficient (3.3) which is related to the coupling quality factor Q_c by Eq. (2.44). This can be rewritten as

$$|t| = \exp(-\frac{\pi L_{\text{rt}} n_g}{\lambda Q_c}) \tag{4.10}$$

or equivalently in terms of the measured power coupling κ^2 in the simulation

$$\kappa^2 = 1 - t^2 = 1 - \exp(-\frac{2\pi L_{\text{rt}} n_g}{\lambda Q_c}) \tag{4.11}$$

this relationship is illustrated in Fig. 4.11.

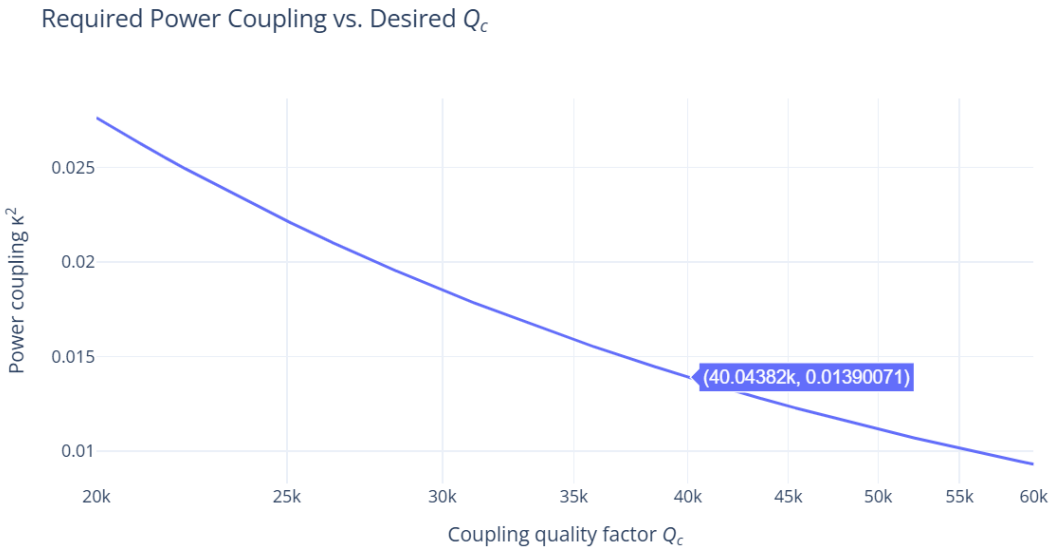


Figure 4.11: Coupling quality factor Q_c as a function of the power coupling coefficient κ^2.

To achieve a design target coupling quality factor Q_c given a chosen radius, the FDTD simulation sweeps across different gap values to find a power coupling coefficient κ^2 that satisfies the desired Q_c.

$$Q_c = \frac{2\pi L_{\mathrm{rt}} n_g}{\lambda \ln\left(\dfrac{1}{1-\kappa^2}\right)} \tag{4.12}$$

4.5 Summary

This chapter established the microring modulator design parameters through a sequence of targeted parameters sweeps. A core width of 500 nm and ring radius of $R = 5.65\,\mu\mathrm{m}$ were selected to satisfy the intrinsic quality factor target of $Q_i = 40\,000$ while simultaneously fulfilling the resonance condition at the design wavelength $\lambda_0 = 1550\,\mathrm{nm}$ (Sec. 4.3). Using this radius, a coupler gap of 0.328 µm was subsequently chosen to achieve the target coupling quality factor $Q_c = 40\,000$ (Sec. 4.4).

Together with the p–n junction geometry described, these choices fully specify the loaded quality factor $Q = 20000$, equivalently the frequency linewidth, that provides a balance between extinction ratio, insertion loss and bandwidth.

These parameters are utilized to generate the artifacts required by the circuit-level simulation in Lumerical INTERCONNECT (Fig. 3.1).

Chapter 5

Simulation Results and Device Optimisation

5.1 PN Junction and Waveguide Simulation Results

The PN junction simulations were performed for three different PN junction configurations: a conventional 500 nm-wide PN junction, a 450 nm-wide PN junction, and an L-shaped 500 nm-wide PN junction shown in the design section.

The database coverage for each PN junction simulation is summarised in Listings 5.1–5.3.

Listing 5.1: Simulation database summary for the 500 nm PN junction.

```
PN Junction: pn_junction_500nm
ID: 1
============================================================
Frequency Sweep
------------------------------------------------------------
  Radii:       11
  Frequencies: 15
  Radius range: 5.000e-06 -> 6.000e-06 m
  Frequency range: 1.922e+14 -> 1.947e+14 Hz
  Active:      [False, True]
Voltage Sweep
------------------------------------------------------------
  Radii:       11
  Voltages:    11
  Radius range: 5.000e-06 -> 6.000e-06 m
  Voltage range: -10.00 -> 0.00 V
AC Characterisation
------------------------------------------------------------
  Voltages:    21
  Frequencies: 41
  Voltage range: -10.00 -> 0.00 V
```

```
  Frequency range: 1.000e+03 -> 1.000e+11 Hz
FDTD Coupling
------------------------------------------------------------
  Radii:       5
  Gaps:        15
  Frequencies: 20
  Radius range: 5.000e-06 -> 6.000e-06 m
  Gap range:    3.500e-07 -> 5.500e-07 m
  Frequency range: 1.874e+14 -> 1.999e+14 Hz
============================================================
```

Listing 5.2: Simulation database summary for the 450 nm PN junction.

```
PN Junction: pn_junction_450nm
ID: 2
============================================================
Frequency Sweep
------------------------------------------------------------
  Radii:       11
  Frequencies: 15
  Radius range: 5.000e-06 -> 6.000e-06 m
  Frequency range: 1.922e+14 -> 1.947e+14 Hz
  Active:      [False, True]
Voltage Sweep
------------------------------------------------------------
  Radii:       11
  Voltages:    11
  Radius range: 5.000e-06 -> 6.000e-06 m
  Voltage range: -10.00 -> 0.00 V
AC Characterisation
------------------------------------------------------------
  Voltages:    21
  Frequencies: 41
  Voltage range: -10.00 -> 0.00 V
  Frequency range: 1.000e+03 -> 1.000e+11 Hz
============================================================
```

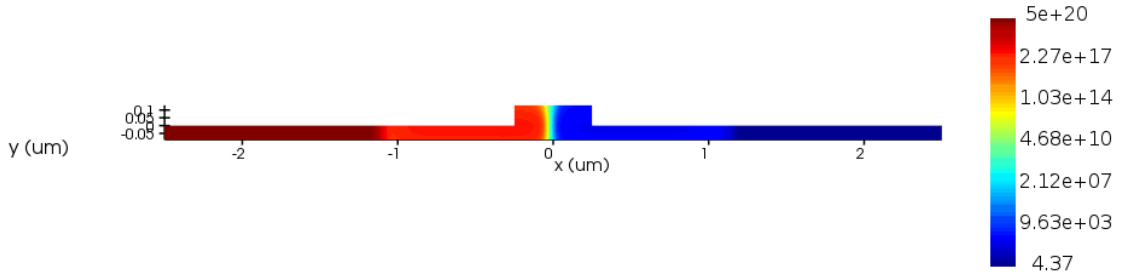
Listing 5.3: Simulation database summary for the L-shaped 500 nm PN junction.

```
PN Junction: pn_junction_lshaped_500nm
ID: 3
============================================================
Frequency Sweep
------------------------------------------------------------
  Radii:       11
  Frequencies: 15
```

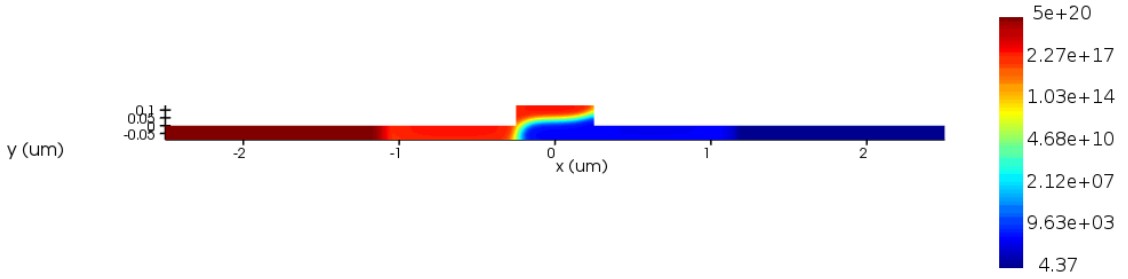
```
  Radius range: 5.000e-06 -> 6.000e-06 m
  Frequency range: 1.922e+14 -> 1.947e+14 Hz
  Active:      [False, True]
Voltage Sweep
------------------------------------------------------------
  Radii:       11
  Voltages:    11
  Radius range: 5.000e-06 -> 6.000e-06 m
  Voltage range: -10.00 -> 0.00 V
AC Characterisation
------------------------------------------------------------
  Voltages:    21
  Frequencies: 41
  Voltage range: -10.00 -> 0.00 V
  Frequency range: 1.000e+03 -> 1.000e+11 Hz
============================================================
```

5.1.1 Junction shape

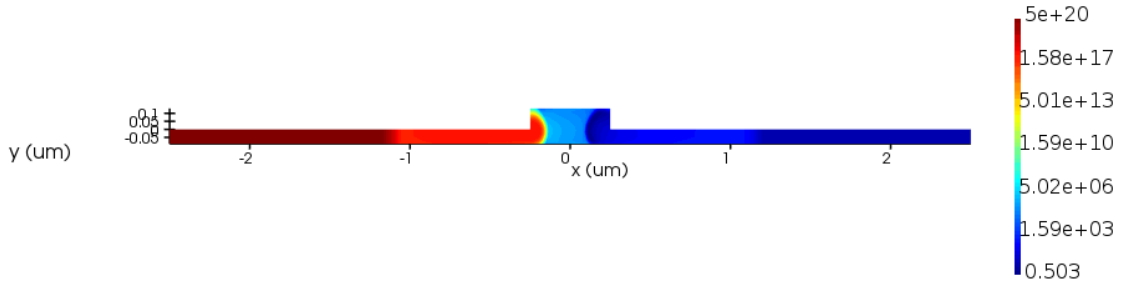
The shape of the junctions designed in Sec. 4.2.3 is illustrated in Fig. 5.1 through the carrier spatial profile. Note the expansion of the depletion width when a reverse bias is applied, in accordance with Sec. 2.3.



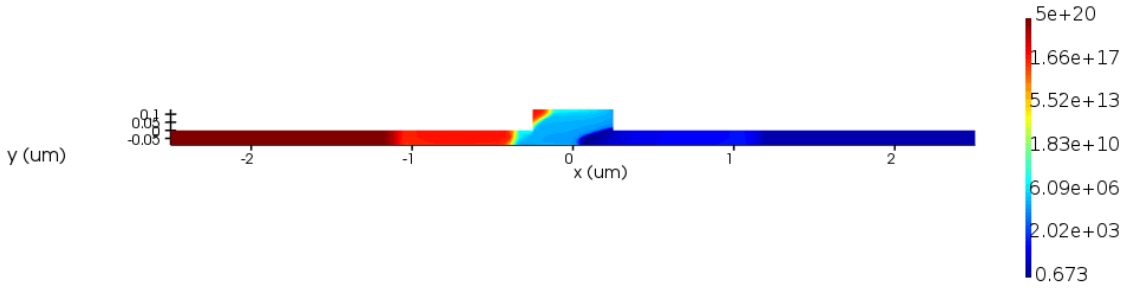
(a) Vertical, 500 nm, 0 V



(b) L-shaped, 500 nm, 0 V



(c) Vertical, 500 nm, 10 V



(d) L-shaped, 500 nm, 10 V

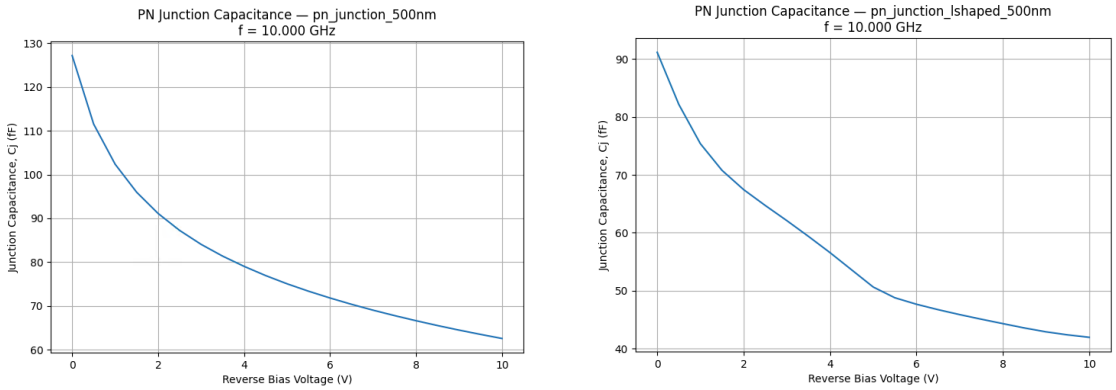
Figure 5.1: Electron carrier density distribution across p–n junction cross-sections at (top row) 0 V and (bottom row) 10 V reverse bias. Vertical junction with core width 500 nm compared against L-shaped geometry at 500 nm core width. The colorbar indicates electron carrier concentration (cm^{-3}).

5.1.2 Junction Characteristics

The electrical characteristics of the vertical and L-shaped PN junctions, with core width 500 nm, are compared in this section.

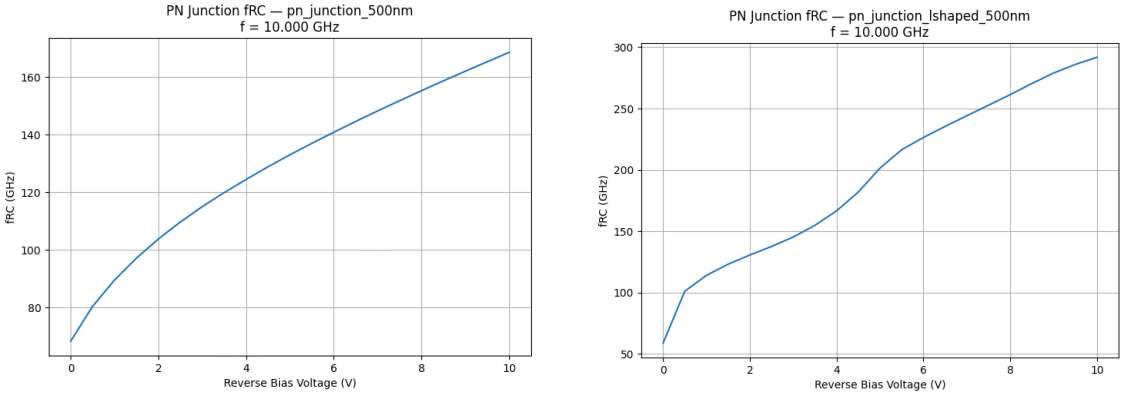
The junction capacitance and the electrical cutoff frequency are shown in Figs. 5.2 and 5.3 respectively. These results characterise the electrical response and bandwidth of the two junction geometries.

The electrical bandwidth f_{τ_j} for the vertical junction is similar to the analytical derivation done by [1], while the bandwidth for the L-shaped junction does not follow a smooth curve. Since the electrical bandwidth is much greater than the optical bandwidth its effect on the modulation will be small, as seen in Eq. (2.71).



(a) Vertical 500 nm (b) L-shaped 500 nm

Figure 5.2: Junction capacitance as a function of reverse-bias voltage for the conventional and L-shaped 500 nm PN junctions. Obtained from a small-signal AC simulation at f = 10 GHz.

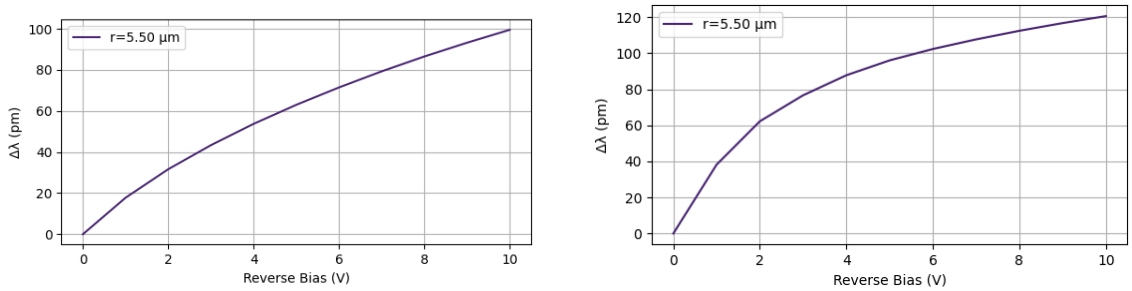


(a) Vertical 500 nm (b) L-shaped 500 nm

Figure 5.3: Electrical cutoff frequency as a function of reverse-bias voltage for the conventional and L-shaped 500 nm PN junctions. Obtained from a small-signal AC simulation at f = 10 GHz.

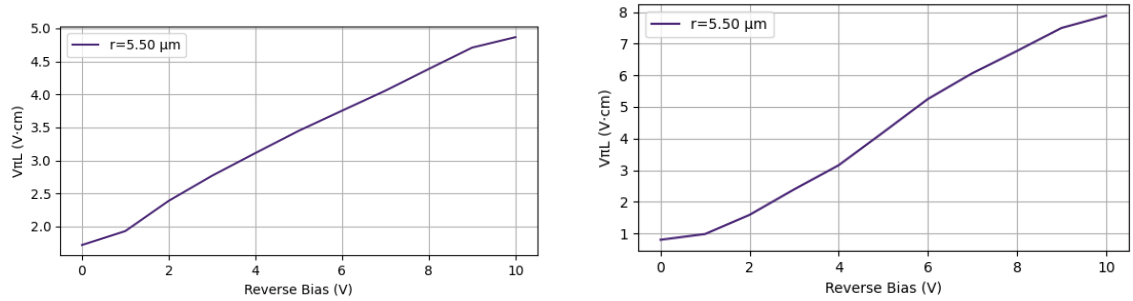
The modulation efficiency of the PN junctions is characterised by the voltage-length product shown in Fig. 5.5 and the resonance wavelength shift shown in Fig. 5.4. In the design chapter (4)

the wavelength shift $\Delta\lambda_{res}$ was utilized to determine other parameters like the target quality factor Q.



(a) Vertical 500 nm (b) L-shaped 500 nm

Figure 5.4: Resonance wavelength shift as a function of reverse-bias voltage for the conventional and L-shaped 500 nm PN junctions.



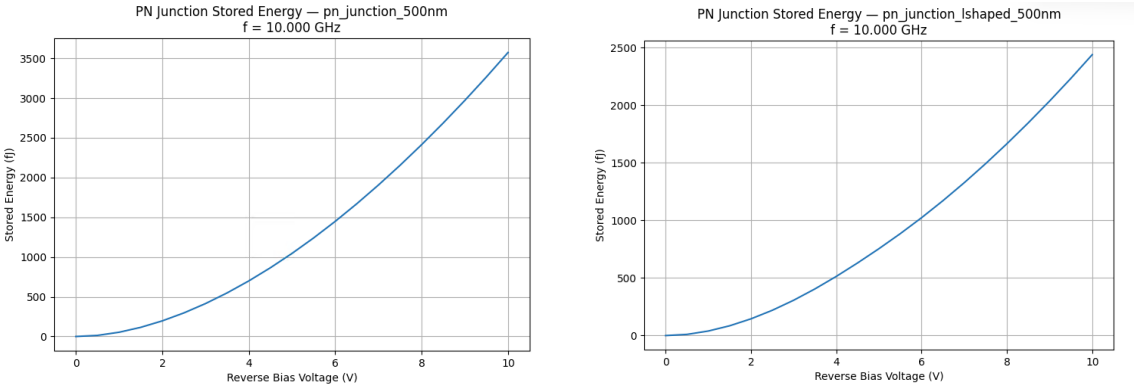
(a) Vertical 500 nm (b) L-shaped 500 nm

Figure 5.5: Local voltage-length product as a function of wavelength for multiple bend radii for the conventional and L-shaped 500 nm PN junctions.

Integrating the junction capacitance (Fig. 5.2) with the applied reverse bias voltage yields the energy stored in the PN junction lumped capacitor model and this energy is presented in Fig. 5.6. The vertical PN junction stores 3500 fJ while the L-shaped junction stores 2500 fJ at 10 V reverse bias, accounting for the fact that the L-shaped junction can have a significant resonance shift with only 4 V reverse bias the energy stored can be as low as 500 fJ. Note that the worst case dynamic consumption (NRZ) is half of capacitor stored energy since a sequence of 1's and 0's has a rising edge only every two bits.

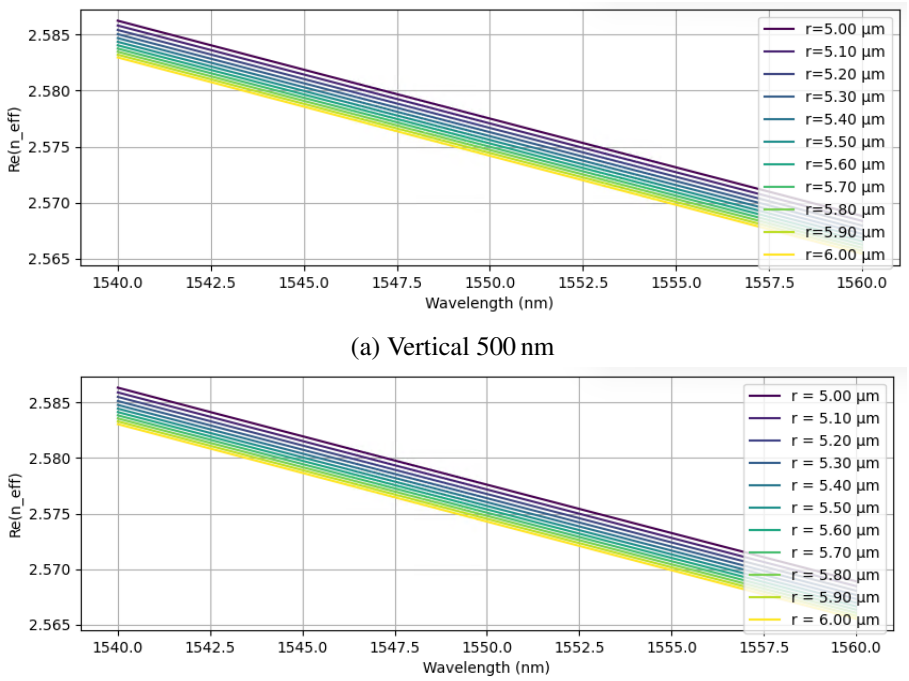
The optical and modal properties of the two 500 nm junction geometries are shown in Figs. 5.7, 5.8 and 5.9. The real and imaginary components of the effective index and the group index are evaluated at zero bias. These quantities characterise the phase response, modal loss, and wavelength-dependent dispersion of the junction waveguides [1].

Finally, the intrinsic quality factor is used to compare all three PN junction configurations, as shown in Fig. 5.10. In contrast to the other characteristics, the comparison with the 450 nm junction is included here to assess the effect of the reduced waveguide width on the intrinsic optical loss. The L-shaped 500 nm junction is compared with the conventional 500 nm geometry



(a) Vertical 500 nm (b) L-shaped 500 nm

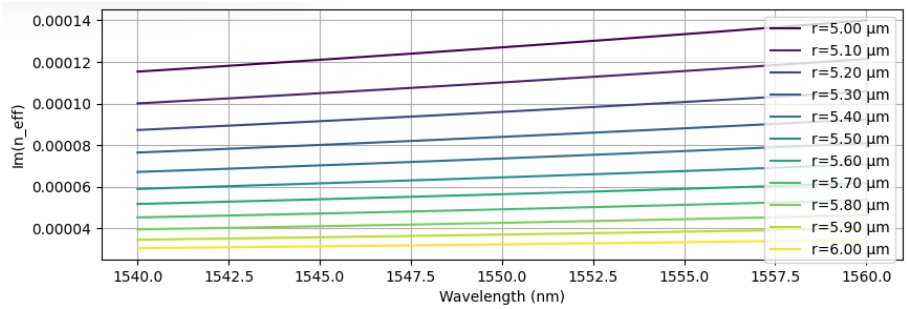
Figure 5.6: Stored electrical energy as a function of reverse-bias voltage for the conventional and L-shaped 500 nm PN junctions.



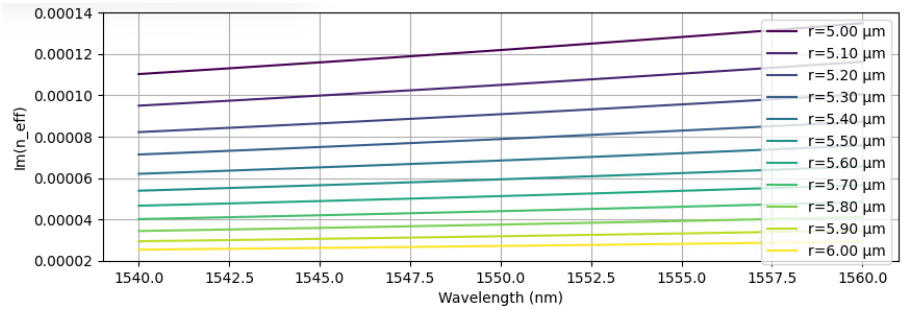
(a) Vertical 500 nm

(b) L-shaped 500 nm

Figure 5.7: Real component of the effective index as a function of wavelength for the conventional and L-shaped 500 nm PN junctions.

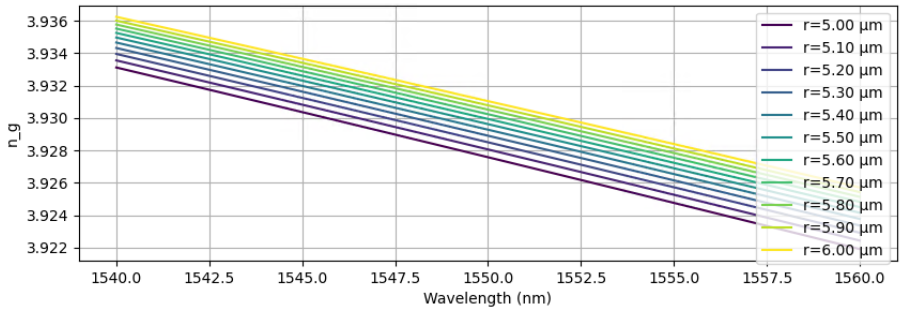


(a) Vertical 500 nm

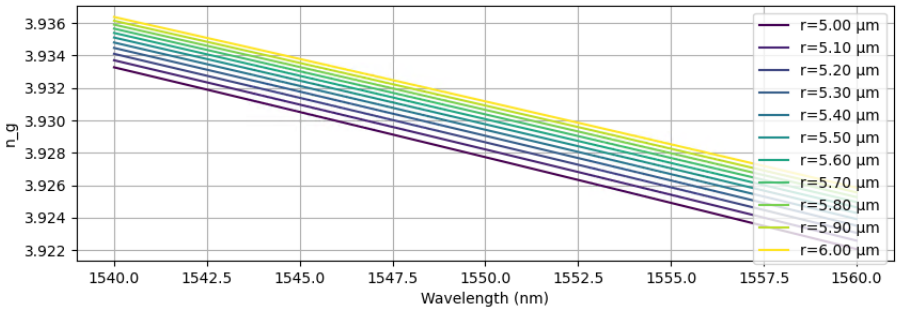


(b) L-shaped 500 nm

Figure 5.8: Imaginary component of the effective index as a function of wavelength for the conventional and L-shaped 500 nm PN junctions.



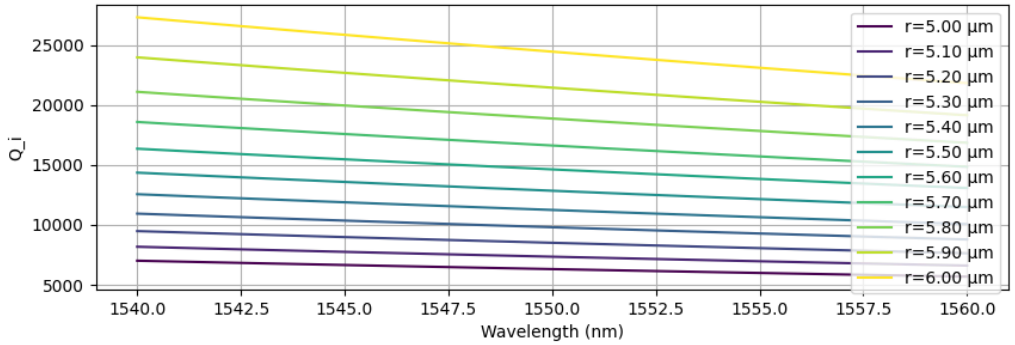
(a) Vertical 500 nm



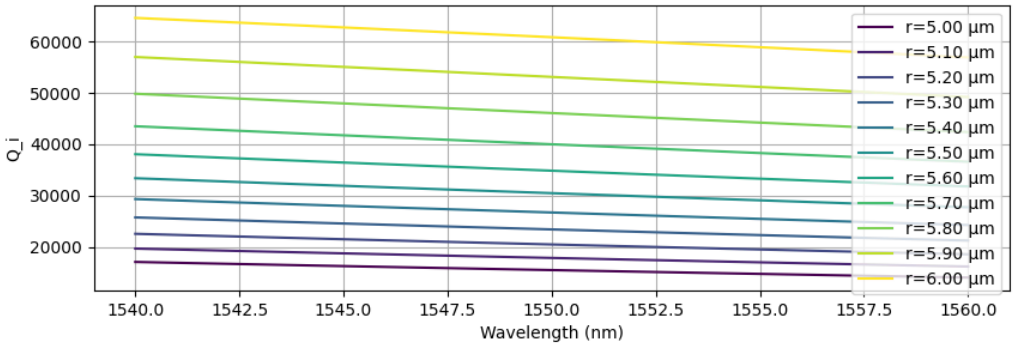
(b) L-shaped 500 nm

Figure 5.9: Group index as a function of wavelength for the conventional and L-shaped 500 nm PN junctions.

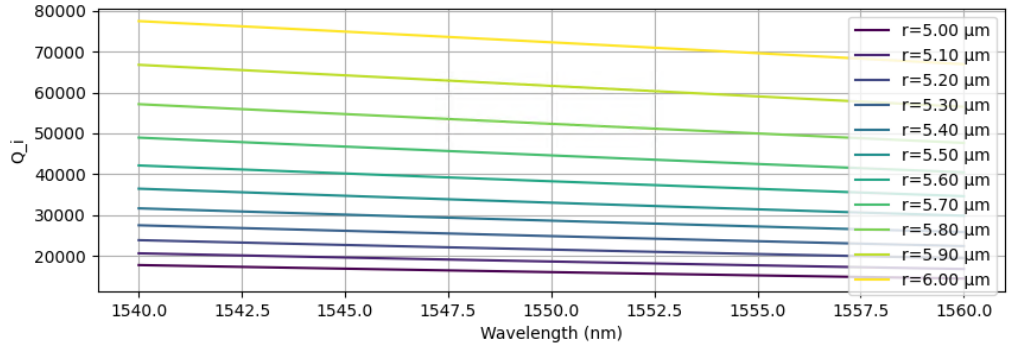
to determine the impact of the modified junction shape on the resonator quality factor in the design chapter 4.



(a) Vertical 450 nm



(b) Vertical 500 nm



(c) L-shaped 500 nm

Figure 5.10: Intrinsic quality factor Q_i as a function of wavelength for the 450 nm vertical, 500 nm vertical, and L-shaped 500 nm PN junction configurations.

5.1.3 Loaded Quality Factor and Optical Bandwidth Optimisation Targets

The resonance wavelength shift $\Delta\lambda_{res}$ obtained from the MODE simulations, for the two junction configurations described in Sec. 4.2.3, is illustrated in Figs. 5.4. The vertical and L-shaped junctions achieve 100 pm and 120 pm respectively at 10 V, the L-shaped junction, however, has a steeper initial slope reaching 100 pm at 5 V and 60 pm at 2 V, which implies a smaller dynamic energy consumption per bit if modulated at those voltages.

Designing for a resonance shift $\Delta\lambda_{\text{res}} = 80\,\text{pm}$, which both junctions can achieve, the required loaded quality factor for a 3-dB insertion loss is approximately $Q = 20000$ with frequency linewidth around 10 GHz, obtained from Eqs. (4.7) and (4.8).

To achieve a coupling ratio of 1 the intrinsic and coupling quality factors must therefore each be approximately 40000 to achieve the design loaded quality factor (2.44).

So the target design values for the different quality factors are

$$Q = 20000, \qquad Q_i = Q_c = 40000$$

As seen in Fig. 5.10, around this radius range (5 µm–6 µm) Q_i is around half its target value for a core width of 450 nm, so a 500 nm width was selected.

$$w_{\text{width}} = 500\text{nm}$$

For a radius around 5 µm–6 µm the active modulation fraction for a clearance of 2.5 µm (half the slab width) is around $\chi = 0.65$ as seen in Fig. 4.3.

$$\chi = 0.65$$

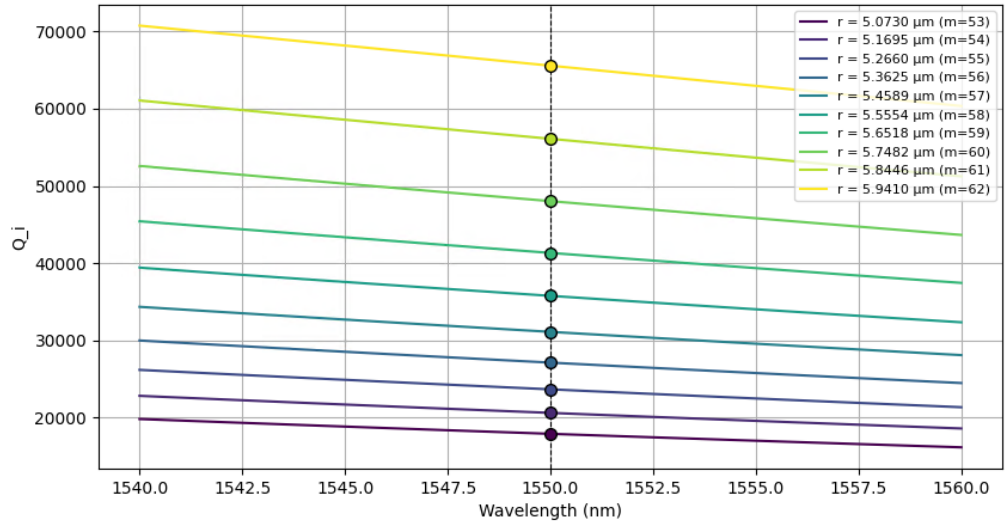
Following the radius selection and design for resonance procedure in Sec. 4.3, the interpolation results of the intrinsic quality factor are shown in Fig. 5.11.

The resonant radius closest to the design target $Q_i = 40000$ are 5.6520 µm and 5.6518 µm for the L-shaped and the vertical junction respectively, the selected radius is therefore

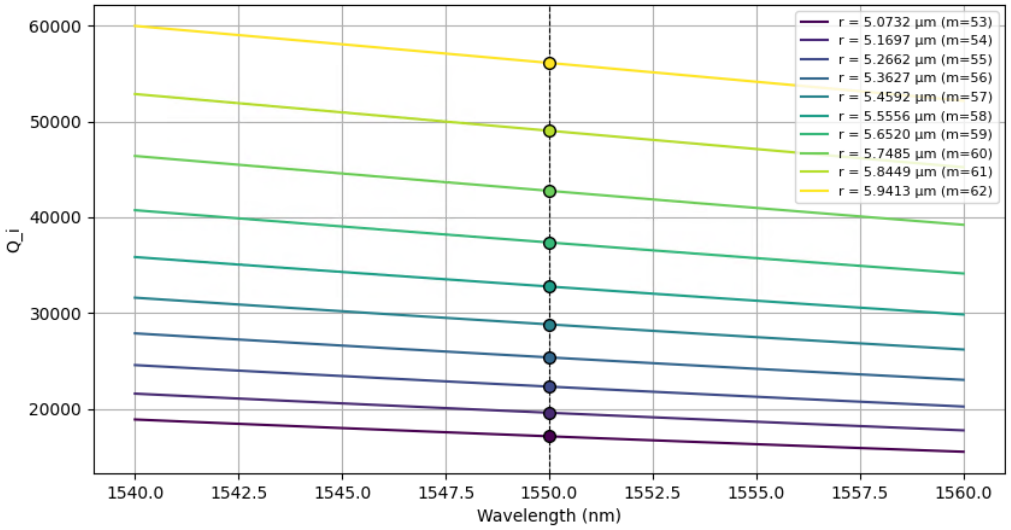
$$R = 5.65\,\mu\text{m}$$

Which yields a resonance slightly blue-shifted (smaller wavelength) from the target resonance value $\lambda_0 = 1550\text{nm}$. This shift however can be corrected later through static compensation.

Inserting these values in the MODE simulations yields the lumerical data files and n_{eff} modulation file, artifacts necessary for the circuit-level simulation as described in the methodology chapter 3.



(a) L-shaped junction



(b) Vertical junction

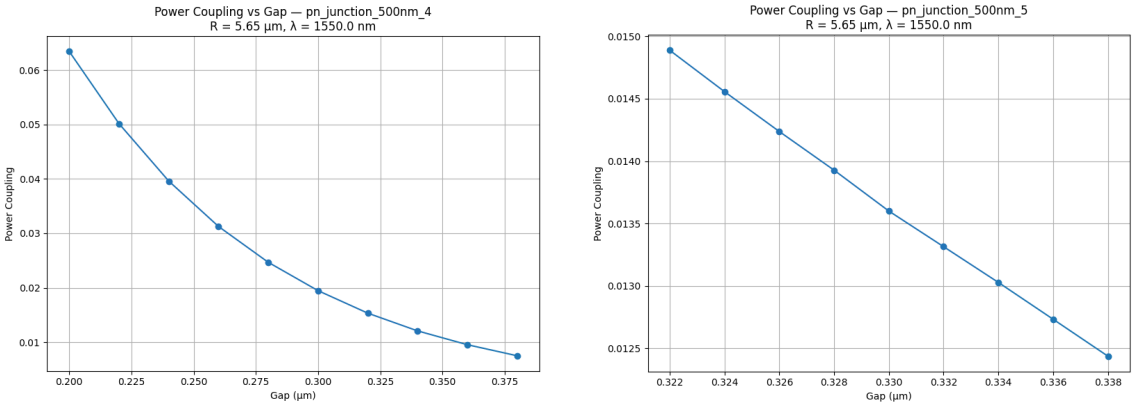
Figure 5.11: Interpolation of the intrinsic quality factor Q_i as a function of ring radius for the L-shaped and vertical PN junction designs.

5.2 Coupling-Gap optimisation

The FDTD simulation results for the coupling region are presented in Fig. 5.12. The power coupling coefficient κ^2 decreases with increasing coupling gap, as expected from the reduced modal overlap between the bus waveguide and the microring.

To achieve the target coupling quality factor of $Q_c = 40000$ the required power coupling coefficient is around $\kappa^2 = 0.0139$, in accordance with Eq. (4.12).

Based on the results of the coarser sweep in Fig. 5.12, a coupler gap of 0.328 µm was selected. From this gap and the corresponding simulation data stored in the database, the coupling coefficient file is generated following the workflow described in the component diagram (Fig. 3.1).



(a) Coupling gap sweep (0.2–0.38 µm).

(b) Coarser coupling gap sweep (0.32–0.34 µm).

Figure 5.12: Power coupling κ^2 as a function of coupling gap at the design wavelength $\lambda_0 = 1550$ nm.

The target coupling quality factor defined in Sec. 4.4 corresponds to a power coupling coefficient of approximately $\kappa^2 = 0.0139$. The gap is a fabrication sensitive parameter since small variations will change κ^2 and consequently coupling quality factor Q_c obtained, which can lead to deviations of the target design.

5.3 Microring Modulator Optimised Device and Generated Layout

Based on the design parameters established in the previous chapter, a complete physical layout of the microring modulator was generated with the Python Automation tool The resulting GDS layout is presented in Fig. 5.13

The results in this section were obtained by inputting the same design parameters in the INTERCONNECT simulation, presented in Sec. 3.7.

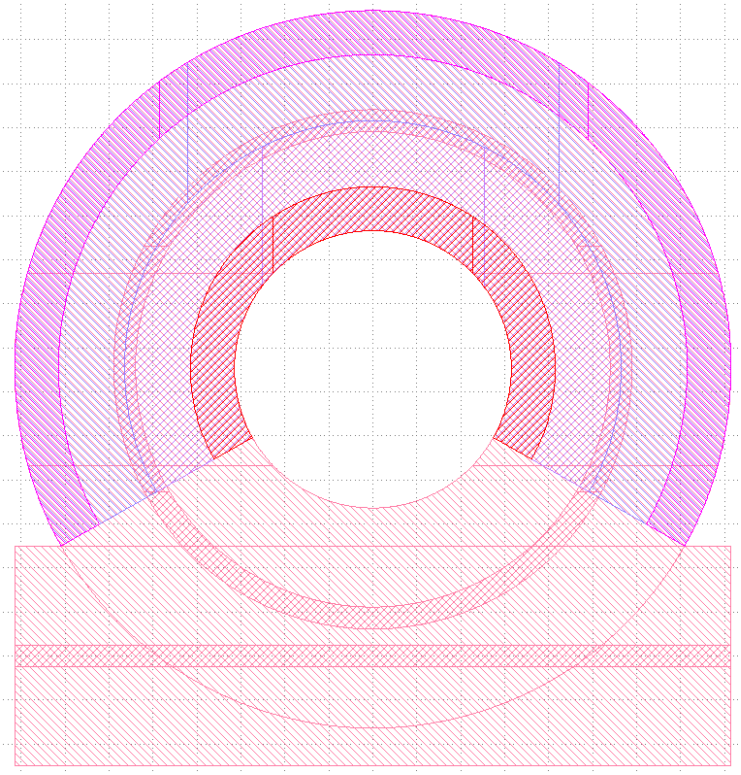


Figure 5.13: Generated GDS layout

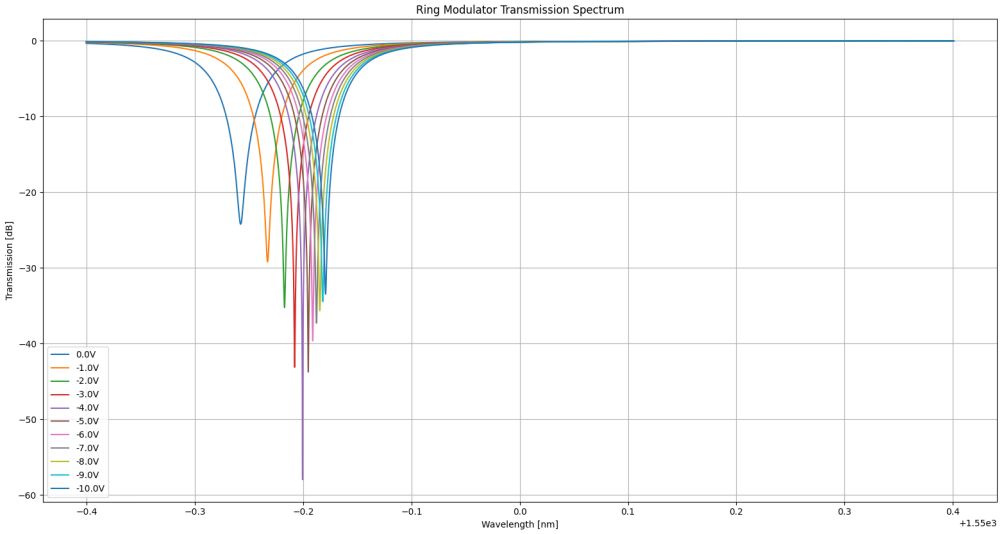
5.3.1 Transmission Spectrum Results

The transmission spectra for the microring designed with the vertical and L-shaped junctions is presented in Figs. 5.14 and 5.15 respectively. Both devices exhibit resonant wavelengths slightly shorter than the design target of 1550 nm, to align the modulator's resonance a static effective index shift is applied, which is usually done through a thermo-optical shift, as detailed in Sec. 2.1.

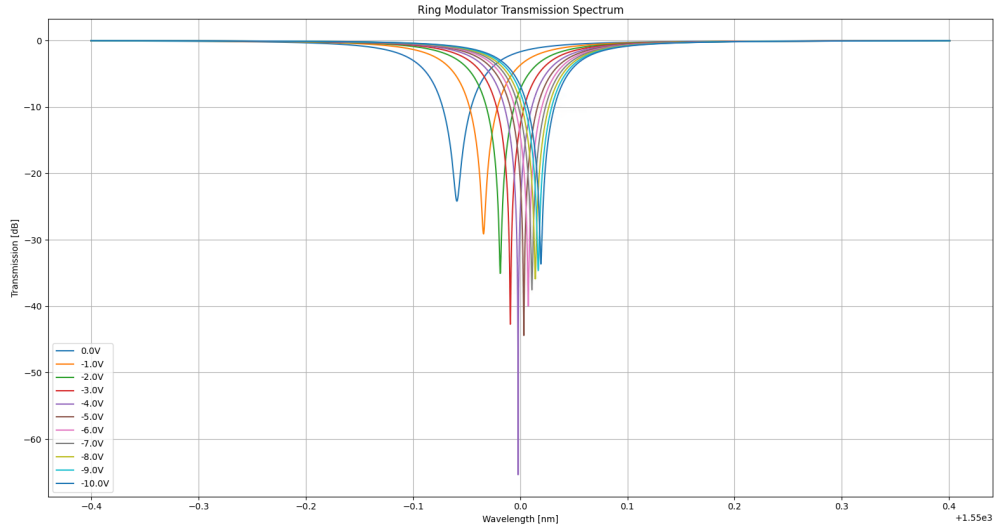
The static effective index shift required was around $5.5 \cdot 10^{-4}$, considering the thermo-optic coefficient of silicon $\frac{dn}{dT} = 1.87 \cdot 10^{-4}\,\mathrm{K}^{-1}$ this corresponds to a 3 K heating above the baseline 300 K.

Spectral Performance Metrics Results: Table 5.1 summarizes the key performance characteristics extracted from both junction configurations. The microring modulator with a L-shaped PN junction demonstrates superior wavelength tunability, achieving a 62.5 pm resonance shift and -60 dB resonance depth at a reverse bias voltage of 4 V. Substituting it by the vertical junction yields a 64.7 pm shift and -30 dB resonance extinction depth at 10 V reverse bias. Both designs have quality factors around 19000 corresponding to a frequency linewidth of around 10.18 GHz.

Voltage-Dependent Wavelength Tuning Results: The resonance wavelength shift as a function of reverse bias voltage is depicted in Fig. 5.16. Both exhibit a progressive decrease in sensitivity



(a) Transmission spectrum.

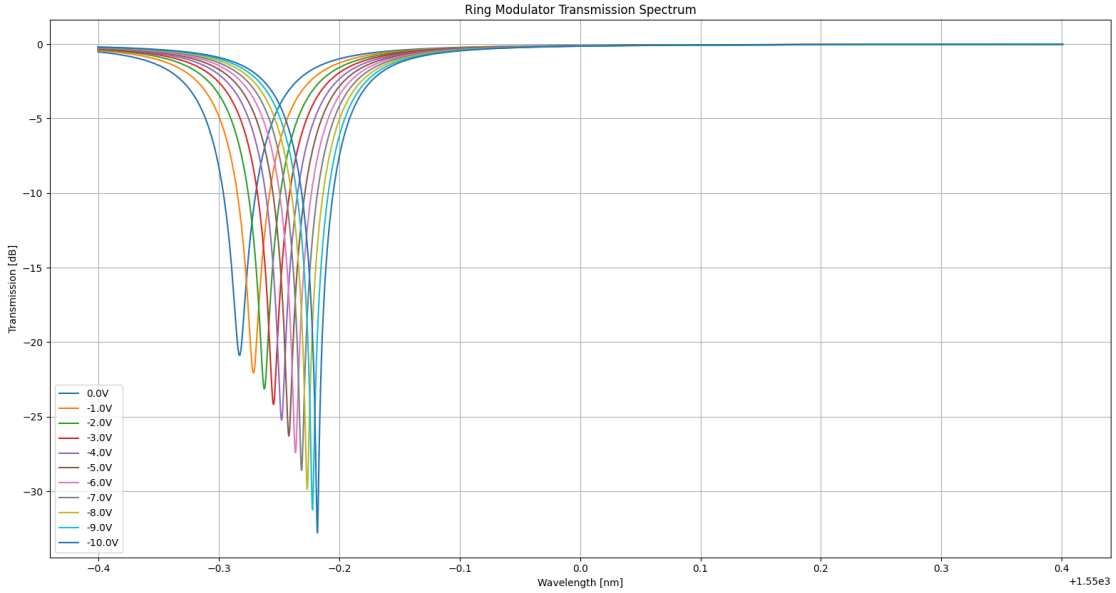


(b) Shifted transmission spectrum.

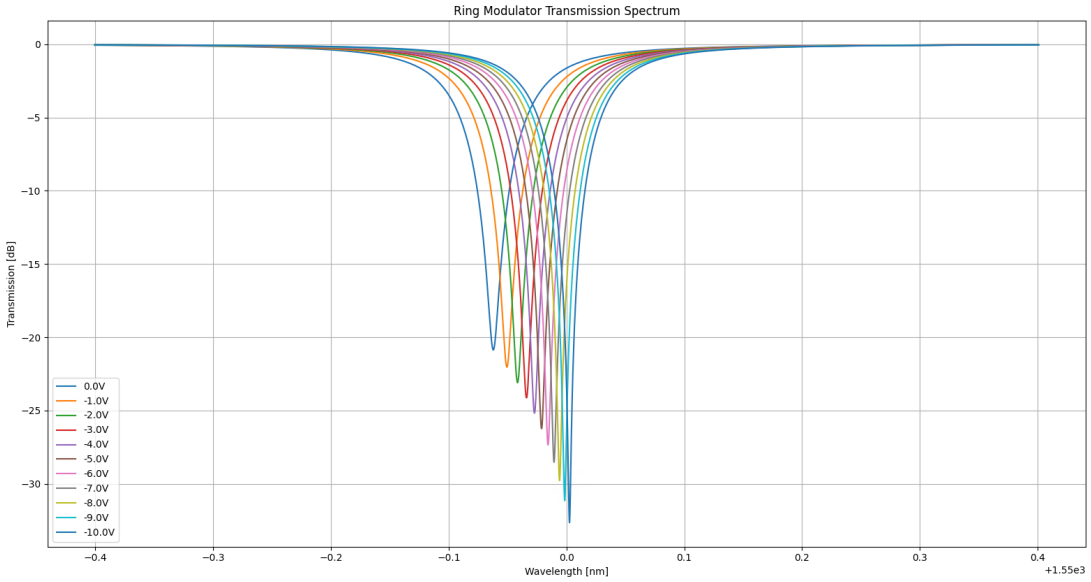
Figure 5.14: Transmission spectrum of microring modulator with L-shaped PN junction.

Parameter	**L-shaped junction**	**Vertical junction**
Quality Factor (Q)	19100	18600
Total Wavelength Shift	62.5 pm @ -4 V	64.7 pm @ -10 V
Insertion Loss	$\approx$ 1.5dB	$\approx$ 1.5dB
Max. Extinction Depth	-60 dB @ -4 V	-30 dB @ -10 V

Table 5.1: Summary of microring modulator performance metrics for L-shaped and vertical PN junctions.



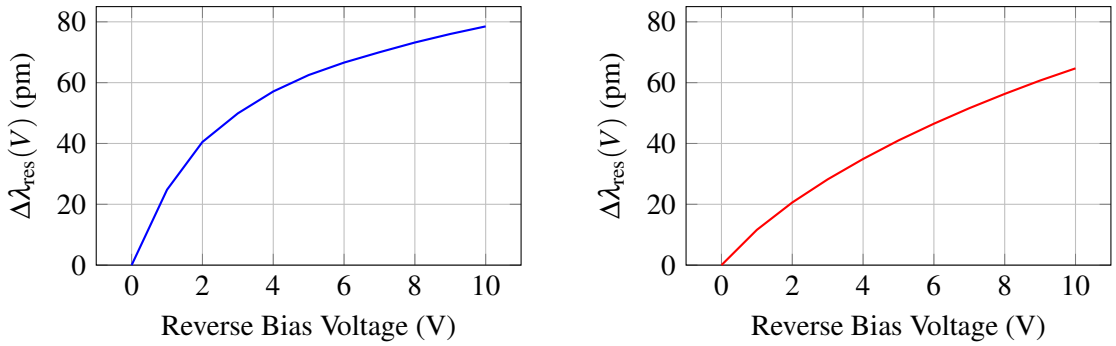
(a) Transmission spectrum.



(b) Shifted transmission spectrum.

Figure 5.15: Transmission spectrum of microring modulator with vertical PN junction.

at higher bias voltages, with the L-shaped junction having a more pronounced nonlinearity with stronger diminishing returns.



(a) L-shaped junction.

(b) Vertical junction.

Figure 5.16: Accumulated wavelength shift as a function of reverse bias voltage for the two PN junction configurations.

5.3.2 Eye Diagrams

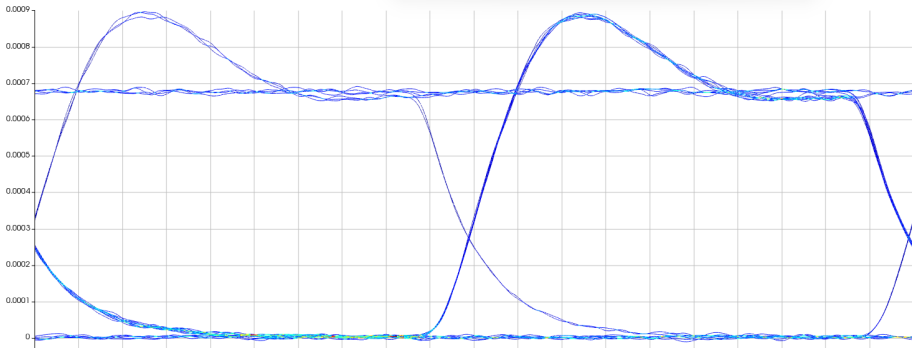
The selected reverse bias voltage levels, summarized in Table 5.2, for OOK and PAM4 schemes were determined to maximize the total extinction ratio whilst having similar and adequate spacing between the PAM4 levels.

PN Junction	Modulation Scheme	Voltage Levels (V)			
L-shaped	OOK	0	4		
L-shaped	PAM4	0	0.95	1.85	4
Vertical	OOK	0	10		
Vertical	PAM4	0	2.5	5	10

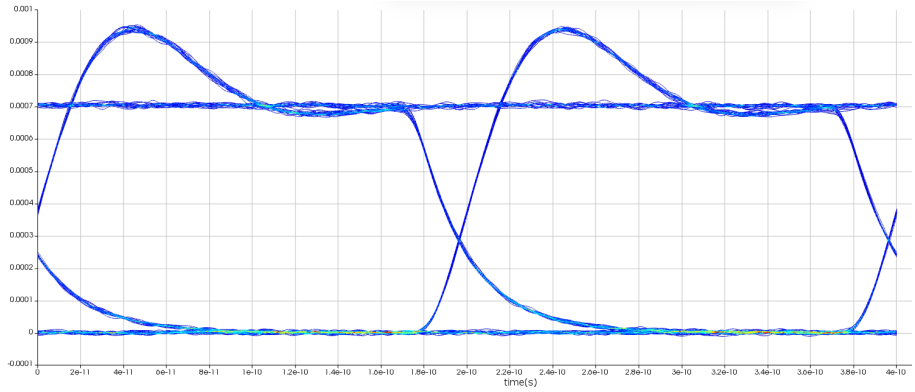
Table 5.2: Modulation voltage levels for OOK and PAM4 schemes across PN junction configurations.

Note that to achieve a linear spacing between the PAM4 levels, the voltage levels chosen ended up having a non-linear spacing, due to the non-linear nature of the transmission curve, requiring an electrical driver that could support this voltage spacing.

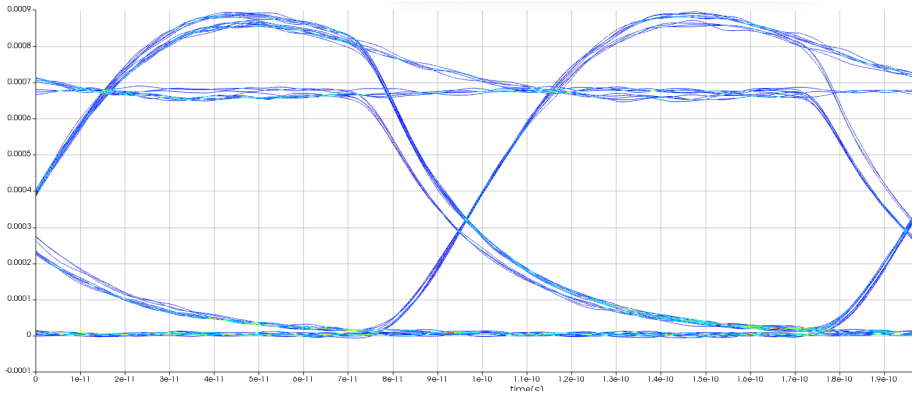
The input power in the microring modulator was set as $P_{\text{in}} = 1\,\text{mW}$ decreasing to around $P_1 = 0.7\,\text{mW}$ due to the insertion loss.



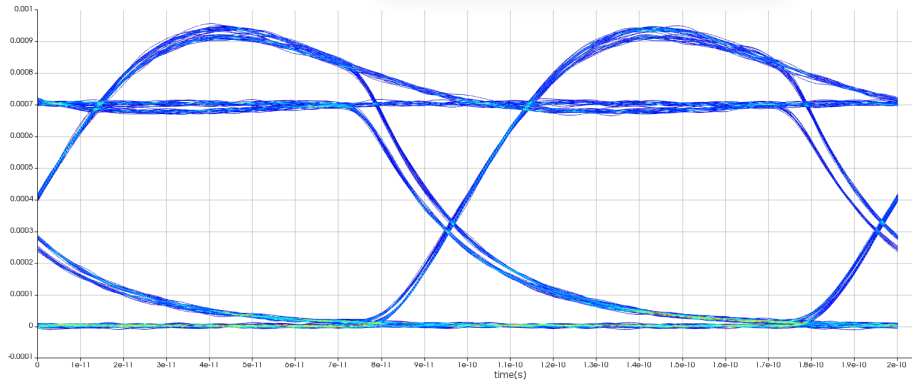
(a) Microring with L-shaped junction, 5 Gbaud



(b) Microring with vertical junction, 5 Gbaud

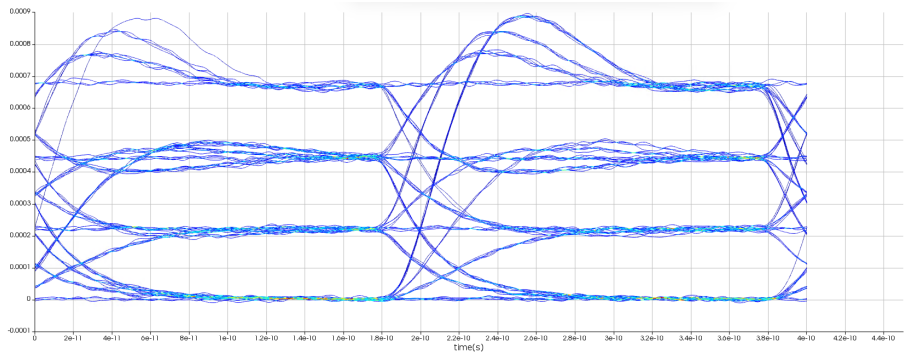


(c) Microring with L-shaped junction, 10 Gbaud

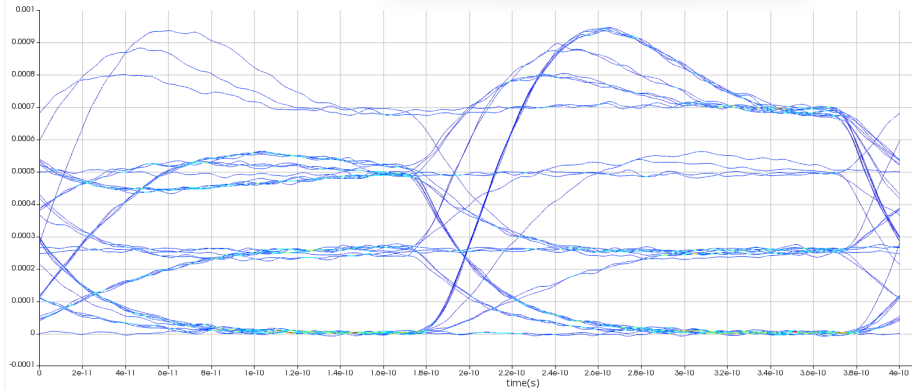


(d) Microring with vertical junction, 10 Gbaud

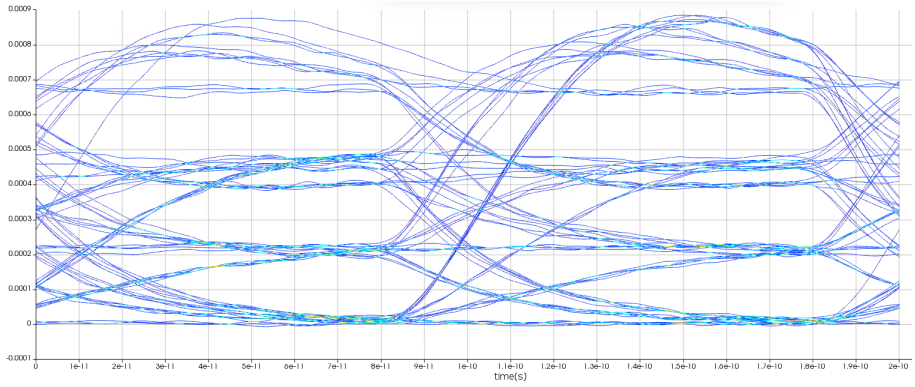
Figure 5.17: OOK eye diagrams comparing L-shaped and vertical PN junction microring modulators at 5 and 10 Gbaud.



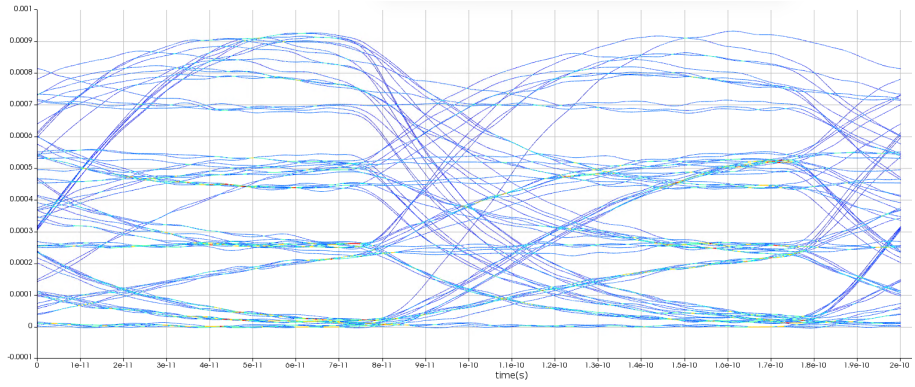
(a) Microring with L-shaped junction, 5 Gbaud (10 Gb/s)



(b) Microring with vertical junction, 5 Gbaud (10 Gb/s)



(c) Microring with L-shaped junction, 10 Gbaud (20 Gb/s)



(d) Microring with vertical junction, 10 Gbaud (20 Gb/s)

Figure 5.18: PAM4 eye diagrams comparing L-shaped and vertical PN junction microring modulators at 5 and 10 Gbaud.

OOK Modulation Comparison The OOK eye diagrams in Fig. 5.17 demonstrate the impact of the PN junction configuration and modulation speed on the transient performance of the microring modulator. At 5 Gb/s, both junction designs achieve clear eye openings, indicating that the optical bandwidth of the resonator is sufficient for this modulation rate. However, the L-shaped junction achieves a comparable modulation depth with a significantly lower driving voltage of 4 V compared with the 10 V required by the vertical junction.

Increasing the symbol rate to 10 Gb/s results in reduced eye openings for both configurations due to the increased influence of the finite optical bandwidth, but still maintaining distinguishable optical levels, with an optical modulation amplitude of around OMA ≈ 0.7 mW.

PAM4 Modulation Comparison For both junction configurations, the voltage levels were selected to provide approximately uniform optical spacing between the four PAM4 levels such that the eye diagrams in Fig. 5.18 exhibit an optical modulation amplitude between levels of around OMA ≈ 0.22 mW, although with reduced eye opening.

At 5 Gb/s, both devices exhibit distinguishable PAM4 levels. At 10 Gb/s, however, the eye openings decrease as a result of bandwidth limitations, which is more apparent for the vertical junction. Nevertheless, the four optical levels remain distinguishable, demonstrating the capability of the designed microring modulator to support PAM4 modulation at this operating rate, with the L-shaped junction providing the best modulation efficiency per driving voltage.

5.4 Summary

This chapter presented the simulation results of the designed silicon photonic microring modulator. The influence of PN junction geometry, coupling conditions, and bias voltage on the optical and electrical performance was evaluated through frequency-domain and time-domain simulations.

The FDTD coupling optimisation enabled the selection of a coupling gap that achieves the desired coupling quality factor, while the INTERCONNECT analysis demonstrated the impact of the PN junction design on the final modulator performance. The L-shaped junction achieved a higher wavelength tuning efficiency and lower operating voltage compared with the conventional vertical junction, resulting in improved modulation efficiency.

Both OOK and PAM4 simulations show that the microring modulators designed can operate at symbol rates of 5 Gb/s and 10 Gb/s which in PAM4 are equivalent to 10 Gbit/s to 20 Gbit/s.

The results demonstrate the feasibility of the proposed design for compact silicon photonic PAM4 transmitters.

Chapter 6

Conclusion and Future Work

6.1 Overview

This dissertation addressed the design, simulation and layout-generation workflow, as well as circuit-level assessment of a silicon photonic microring modulator intended for multilevel pulse-amplitude modulation. This work pursued this objective through a multiphysics hierarchical workflow, connecting the electrical behaviour of carrier-depletion ON junctions to waveguide propagation, directional coupler design, resonator design and then system-level transmission.

Within the scope of numerical simulations, the main objective was achieved: a complete microring modulator was parameterised, its physical layout generated, and its static and dynamic performance assessed for OOK and PAM4 operation.

6.2 Main Findings

The design procedure converged on a 500 nm waveguide core, a ring radius of 5.65μm, and a coupling gap of 0.328μm. The intrinsic and coupling quality factors were each targeted at approximately 40000, corresponding to a loaded quality factor close to 20000. The circuit simulations produced loaded quality factors of approximately 19100 for the L-shaped junction design and 18600 for the conventional vertical junction design. These values correspond to an optical FWHM linewidth of ≈ 10.18GHz around 1550nm.

The comparison between junction geometries shows that the L-shaped PN junction provides the most favourable modulation-efficiency trade-off among the configurations studied. According to the spectral metrics summarised in Table 5.1, the L-shaped and vertical junction devices achieve total resonance shifts of 78.5pm and 64.7pm, respectively, at a reverse-bias voltage of 10V. Both devices exhibit an insertion loss of approximately 1.5dB, the L-shaped design also reaches a substantially deeper simulated resonance at a lower reverse-bias voltage, -60dB at -4V, compared with approximately -30dB at -10V for the vertical design. This behaviour results from the resonator design, with the L-shaped junction design achieving critical coupling with a smaller voltage.

The lower driving voltage requirements are also reflected in the stored electrical energy in the lumped capacitor model of the PN junction. The simulated curves indicate approximately 0.5pJ stored in the L-shaped junction at a reverse-bias voltage of 4V, whereas the vertical junction stores approximately 3.5pJ at 10V. These values should not be interpreted as the complete transmitter energy per bit, which also depends on the driver, the transition statistics and static energy consumption, usually from thermal-control overhead.

The time-domain simulations show that both junction configurations produce clearly separated OOK and PAM4 levels at 5GBd and 10GBd, although the increase in the modulation rate and number of levels reduces the eye opening. The best compromise between drive voltage and bandwidth is provided by the L-shaped junction microring modulator at 10GBd PAM4, corresponding to a bit rate of 20Gbit/s.

Overall, the results demonstrate, at the simulation level, that the design methodology can generate a compact resonant modulator capable of OOK and PAM4 operation, although no evidence of error-free operation is provided. The microring geometry cannot be optimized from a single metric: modulation efficiency, capacitance, optical loss, resonator quality factor, drive voltage and bandwidth must be considered together.

6.3 Limitations

The conclusions of this work are based exclusively on numerical models that use as reference default material parameters and doping concentrations. Although a GDS layout was generated, the device was not fabricated or experimentally characterised.

The design also remains sensitive to fabrication variations. In particular, the coupling gap directly determines the coupling quality factor, while deviations in waveguide width, etch depth, doping, and ring radius can change the resonance wavelength and intrinsic quality factor. Resonance alignment was represented by a static effective-index correction usually done through a thermo-optic control; however the heater and the associated control loop were not modelled.

The system-level assessment is limited to simulated eye diagrams at 5 and 10GBd. No OOK or PAM4 figures of merit were calculated and no noise sources were included. Moreover, the non-uniform voltage levels selected require a suitable electrical driver that wasn't modelled.

Finally, the energy values reported in the results represent energy stored in the junction capacitance rather than a complete energy per bit. A full comparison should include driver losses and thermal tuning losses.

6.4 Future Work

Future work should focus on:

- **Experimental validation:** Fabricate and characterise the proposed devices, and compare measurements with CHARGE, MODE, FDTD, and INTERCONNECT simulations to validate and refine the models.

- **Fabrication robustness:** Assess process variations through Monte Carlo simulations to evaluate the device parameter sensitivity to fabrication deviations and then optimise design parameters to account for these deviations.
- **PN junction optimisation:** Further refine the L-shaped junction to reduce drive voltage and capacitance while increasing the achievable resonance shift.
- **System-level analysis:** Evaluate performance with realistic transmitter and receiver models over a wider range of symbol rates, including the effects of parasitics, noise, equalisation, and predistortion.
- **Workflow automation:** Extend the design framework with closed-loop optimisation, where an algorithm modifies the design and reruns the simulations, minimizing the simulation steps that need to be done manually.

6.5 Final Remarks

This dissertation establishes a coherent path from PN junction design to resonator design and finally the simulation and performance assessment of a complete silicon microring modulator. The main value of the work is the workflow, from the simulation methodology to the design choices, used to design and assess the preliminary PAM4 operation at 10GBd of the investigated ring resonators.

References

[1] Lukas Chrostowski and Michael E. Hochberg. *Silicon photonics design*. en. Cambridge: Cambridge university press, 2015. ISBN: 978-1-107-08545-9.

[2] Sudip Shekhar et al. "Roadmapping the next generation of silicon photonics". en. In: *Nature Communications* 15.1 (Jan. 2024), p. 751. ISSN: 2041-1723. DOI: 10.1038/s41467-024-44750-0. URL: https://www.nature.com/articles/s41467-024-44750-0 (visited on 10/27/2025).

[3] B E Little et al. "Microring Resonator Channel Dropping Filters". en. In: ().

[4] Jie Sun et al. "A 128 Gb/s PAM4 Silicon Microring Modulator With Integrated Thermo-Optic Resonance Tuning". en. In: *Journal of Lightwave Technology* 37.1 (Jan. 2019), pp. 110–115. ISSN: 0733-8724, 1558-2213. URL: https://ieeexplore.ieee.org/document/8510799/ (visited on 12/31/2025).

[5] Govind P. Agrawal. *Fiber-optic communication systems*. en. Fifth edition. Hoboken, NJ: Wiley, 2021. ISBN: 978-1-119-73737-7 978-1-119-73738-4 978-1-119-73739-1.

[6] Robert W. Boyd. *Nonlinear Optics*. en. 4th ed. San Diego: Elsevier Science & Technology, 2020. ISBN: 978-0-12-811002-7 978-0-12-811003-4.

[7] R. Soref and B. Bennett. "Electrooptical effects in silicon". en. In: *IEEE Journal of Quantum Electronics* 23.1 (Jan. 1987), pp. 123–129. ISSN: 0018-9197. DOI: 10.1109/JQE.1987.1073206. URL: http://ieeexplore.ieee.org/document/1073206/ (visited on 01/02/2026).

[8] Guoliang Li et al. "Ring Resonator Modulators in Silicon for Interchip Photonic Links". In: *IEEE Journal of Selected Topics in Quantum Electronics* 19.6 (Nov. 2013), p. 3401819. DOI: 10.1109/JSTQE.2013.2278885.

[9] Richard M. Osgood Jr. and Xiuling Meng. *Principles of Photonic Integrated Circuits: Materials, Device Physics, Guided Wave Design*. Graduate Texts in Physics. Cham: Springer International Publishing, 2021. DOI: 10.1007/978-3-030-65193-0.

[10] A. Yariv and P. Yeh. *Photonics: Optical Electronics in Modern Communications*. Oxford series in electrical and computer engineering. Oxford University Press, 2007. ISBN: 978-0-19-517946-0. URL: https://books.google.de/books?id=B2xwQgAACAAJ.

[11] Brian Pile and Geoff Taylor. "Small-signal analysis of microring resonator modulators". en. In: *Optics Express* 22.12 (June 2014), p. 14913. ISSN: 1094-4087. DOI: 10.1364/OE.22.014913. URL: https://opg.optica.org/oe/abstract.cfm?uri=oe-22-12-14913 (visited on 01/04/2026).

[12] Ansys. *Ring Modulator*. https://optics.ansys.com/hc/en-us/articles/360042322794-Ring-Modulator. Accessed 20 Jul. 2026.

[13] Ansys. *Optical PAM4 transceiver*. https://optics.ansys.com/hc/en-us/articles/360042322694-Optical-PAM4-transceiver. Accessed 20 Jul. 2026.

[14] Ansys. *PN-depletion phase shifter*. https://optics.ansys.com/hc/en-us/articles/360042328674-PN-depletion-phase-shifter. Accessed 20 Jul. 2026.

[15] Ansys. *Ansys Lumerical CHARGE*. Software. Version 2022 R2.1.

[16] Ansys. *Ansys Lumerical MODE*. Software. Version 2022 R2.1.

[17] Ansys. *Ansys Lumerical FDTD*. Software. Version 2022 R2.1.

[18] Ansys. *Ansys Lumerical INTERCONNECT*. Software. Version 2022 R2.1.

[19] M. Hamouda et al. "PN Junction Optimization for High-Speed Silicon Photonic Modulators". In: *Photonics* 12.11 (Oct. 2025), p. 1079. DOI: 10.3390/photonics12111079.